1-1-2012

Probing DNA-Induced Colloidal Interactions and Dynamics with Scanning-Line Optical Tweezers

William Benjamin Rogers
University of Pennsylvania, wrogers@seas.harvard.edu

Recommended Citation

Rogers, William Benjamin, "Probing DNA-Induced Colloidal Interactions and Dynamics with Scanning-Line Optical Tweezers" (2012). *Publicly Accessible Penn Dissertations*. 568.
http://repository.upenn.edu/edissertations/568

Probing DNA-Induced Colloidal Interactions and Dynamics with Scanning-Line Optical Tweezers

Abstract

A promising route to forming novel nanoparticle-based materials is directed self-assembly, where the interactions among multiple species of suspended particles are intentionally designed to favor the self-assembly of a specific cluster arrangement or nanostructure. DNA provides a natural tool for directed particle assembly because DNA double helix formation is chemically specific — particles with short single-stranded DNA grafted on their surfaces will be bridged together only if those strands have complementary base sequences. Moreover, the temperature-dependent stability of such DNA bridges allows the resulting attraction to be modulated from negligibly weak to effectively irreversible over a convenient range of temperatures. Surprisingly, existing models for DNA-induced particle interactions are typically in error by more than an order of magnitude, which has hindered efforts to design complex temperature, sequence and time-dependent interactions needed for the most interesting applications. Here we report the first spatially resolved measurements of DNA-induced interactions between pairs of polystyrene microspheres at binding strengths comparable to those used in self-assembly experiments. The pair-interaction energies measured with our optical tweezers instrument can be modeled quantitatively with a conceptually straightforward and numerically tractable model, boding well for their application to direct self-assembly.

In addition to understanding the equilibrium interactions between DNA-labeled particles, it is also important to consider the dynamics with which they bind to and unbind from one another. Here we demonstrate for the first time that carefully designed systems of DNA-functionalized particles exhibit effectively diffusion-limited binding, suggesting that these interactions are suitable to direct efficient self-assembly. We systematically explore the transition from diffusion-limited to reaction-limited binding by decreasing the DNA labeling density, and develop a simple dynamic model that is able to reproduce some of the anomalous kinetics observed in multivalent binding processes. Specifically, we find that when compounded, static disorder in the melting rate of single DNA duplexes gives rise to highly non-exponential lifetime distributions in multivalent binding. Together, our findings motivate a nanomaterial design approach where novel functional structures can be found computationally and then reliably realized in experiment.

Degree Type

Dissertation

Degree Name

Doctor of Philosophy (PhD)

Graduate Group

Chemical and Biomolecular Engineering

First Advisor

John C. Crocker

Keywords
colloidal interactions, functional particles, multivalent binding, nucleic acids, optical tweezers, self-assembly

Subject Categories
Biophysics | Chemical Engineering | Physics

PROBING DNA-INDUCED COLLOIDAL INTERACTIONS AND DYNAMICS WITH SCANNING-LINE OPTICAL TWEEZERS

William Benjamin Rogers

A DISSERTATION

in

Chemical and Biomolecular Engineering

Presented to the Faculties of the University of Pennsylvania in Partial Fulfillment of the
Requirements for the Degree of Doctor of Philosophy

2012

Supervisor of Dissertation

____
John C. Crocker
Associate Professor, Chemical and Biomolecular Engineering

Graduate Group Chairperson

____
Raymond J. Gorte
Russel Pearce and Elizabeth Crimian Heuer Professor, Chemical and Biomolecular Engineering

Dissertation Committee

Ravi Radhakrishnan, Associate Professor, Bioengineering
Talid R. Sinno, Associate Professor, Chemical and Biomolecular Engineering
Kathleen J. Stebe, Richer and Elizabeth Goodwin Professor, Chemical and Biomolecular Engineering

PROBING DNA-INDUCED COLLOIDAL INTERACTIONS AND DYNAMICS WITH SCANNING-LINE OPTICAL TWEEZERS

ACKNOWLEDGEMENT

This work would not have been possible without the help of the following individuals: my advisor, John Crocker, for his guidance and unparalleled intuition; my colleagues, Bob Meyer, Valeria Garbin, and Marie Ung, for their camaraderie; my former classmates, Will Tisdale, Alison Tisdale, and Nabil Laachi, for their inspiration and friendship; my friend, Lindsey Martin, and family, Laura Rogers, Chris Rogers, David Rogers, and Elizabeth English, for their unending support; and my companion, Kassie Richardson, for her patience and encouragement.

ABSTRACT

PROBING DNA-INDUCED COLLOIDAL INTERACTIONS AND DYNAMICS WITH SCANNING-LINE OPTICAL TWEEZERS

William Benjamin Rogers

Supervisor: John C. Crocker

A promising route to forming novel nanoparticle-based materials is directed self-assembly, where the interactions among multiple species of suspended particles are intentionally designed to favor the self-assembly of a specific cluster arrangement or nanostructure. DNA provides a natural tool for directed particle assembly because DNA double helix formation is chemically specific—particles with short single-stranded DNA grafted on their surfaces will be bridged together only if those strands have complementary base sequences. Moreover, the temperature-dependent stability of such DNA bridges allows the resulting attraction to be modulated from negligibly weak to effectively irreversible over a convenient range of temperatures. Surprisingly, existing models for DNA-induced particle interactions are typically in error by more than an order of magnitude, which has hindered efforts to design complex temperature, sequence and time-dependent interactions needed for the most interesting applications. Here we report the first spatially resolved measurements of DNA-induced interactions between pairs of polystyrene microspheres at binding strengths comparable to those used in self-assembly experiments. The pair-interaction energies measured with our optical tweezers instrument can be modeled quantitatively with a conceptually straightforward and numerically tractable model, boding well for their application to direct self-assembly.

In addition to understanding the equilibrium interactions between DNA-labeled particles, it is also important to consider the dynamics with which they bind to and unbind from one another. Here we demonstrate for the first time that carefully designed systems of DNA-functionalized particles exhibit effectively diffusion-limited binding, suggesting that these interactions are suitable to direct efficient self-assembly. We systematically explore the transition from diffusion-limited to reaction-limited binding by decreasing the DNA labeling density, and develop a simple dynamic model that is able to reproduce some of the anomalous kinetics observed in multivalent binding processes. Specifically, we find that when compounded, static disorder in the melting rate of single DNA duplexes gives rise to highly non-exponential lifetime distributions in multivalent binding. Together, our findings motivate a nanomaterial design approach where novel functional structures can be found computationally and then reliably realized in experiment.

Contents

List of Tables

List of Figures

Chapter 1

Introduction

1.1 Directed Self-Assembly

Self-assembly refers to the process by which discrete building blocks spontaneously organize into ordered structures, and is the predominant scheme that nature uses to build sophisticated architectures. In an attempt to emulate and extend the effortless manner in which nature generates complexity and function, researchers are trying to facilitate this process by carefully selecting and designing the building blocks to guide the assembly of novel ordered structures, a process called directed self-assembly. Unlike the conventional 'top-down' approach to materials synthesis, which uses traditional workshop or microfabrication methods to cut, pattern and shape materials, the 'bottom-up' approach of directed self-assembly has the potential to produce complex assemblies in a massively parallel, cheap and scalable way. Currently, our ability to precisely position components on the nanometer/micrometer scale the way nature does in a parallel manner is somewhat limited, but groups are beginning to make great progress in designing functional building blocks through chemical (1), spatial (2) and morphological modification (3, 4). Unfortunately, this classical chemical toolbox (e.g. electrostatic and entropic interactions), primarily developed in the context of colloidal stabilization, often lacks the high degree of chemical specificity required for the most complex applications, for example, directing the assembly of the next generation microprocessor. Nucleic acids can help overcome this problem though, as the exquisite specificity of Watson-Crick base pairing allows for the construction of combinatorial libraries of tunable, reversible and addressable interactions. This promise was first realized in the early 1980s for the assembly of structural motifs made entirely of DNA (5), and later extended to the directed-assembly of inorganic particle-based systems (6, 7).

1.2 DNA-Directed Assembly

Deoxyribonucleic acid (DNA), the genetic blueprint for life, is one of the most remarkable self-assembling molecules. Following precise Watson-Crick base pairing rules, two complementary DNA sequences assemble into a double helix (or duplex) through a cooperative interplay of hydrogen bonding, π-stacking, electrostatic and hydrophobic interactions (8). Because of the near-infinite number of combinations and permutations of this simple code, DNA is emerging as an ideal material that is capable of, in principle, directing the assembly of materials into any designed structure of arbitrary complexity. Moreover, because DNA structure and stability play such a crucial role in the development and function of nearly all known living organisms, it has been carefully characterized from nearly every perspective (e.g. structurally, thermodynamically, kinetically, etc.).

While the molecular level structural detail is essential for the assembly of materials made entirely of DNA, it is the thermodynamic stability of hybridized duplexes that is most important from the perspective of using DNA as reversible, molecular bridges between particle-based assemblies. Fortunately, there are extensive databases of the thermodynamic parameters for many of the most common motifs (e.g. Watson-Crick base pairs, internal mismatches, dangling ends, loops, bulges, hairpins, etc.) that can be used to predict the stability of DNA secondary structure (9-11). In the most complicated systems, dynamic programming algorithms are available and many of these routines have been packaged into user-friendly web-based services that are freely available (12, 13). In other simpler systems (e.g. hybridization between a few well-designed, orthogonal sequences), hybridization between DNA complements is accurately modeled as a simple two-state process, and a nearest-neighbor model is sufficient to predict the hybridization free energy and associated duplex stability as a function of concentration, temperature and ionic strength, for example. This ability, then, to make *a priori* predictions of duplex stability, coupled with rapid advances in DNA synthesis, purification and amplification, make DNA an ideal material for directed materials synthesis.

Interestingly, unlike the significant progress in 'DNA nanotechnology,' where DNA has been used to build molecular machines (14), assembly lines (15), and macroscopic, crystalline scaffolds that could precisely position arrays of proteins for genomics and proteomics (16), only a handful of particle-based assemblies have been formed, despite the fact that a number of interesting structures have been predicted theoretically (17). Still, over the past fifteen years or so, several groups have used such interactions to drive the assembly of three-dimensional, crystalline structures from both nanoscopic (18-22) and microscopic (23, 24) particles. Moreover, two recent studies, one that used real-space electron microscopy to characterize and quantify a full zoo of ordered nanoparticle metamaterials (25), and another that used carefully modulated DNA-induced interactions to drive a martensitic-like structural transformation of polymer microspheres (26), demonstrate that we are just scratching the surface of this technology. Ultimately, we envision a highly versatile design protocol in which a user-designed matrix of specific interactions among multiple particle species leads to sequential or even hierarchical assembly of complex particle structures, controlled by a user-designed thermal program.

1.3 Measuring DNA-Induced Interactions: Line Optical Tweezers

Unlike this vision of designable, sequential and hierarchical assembly among a significant number of different components, current experiments typically employ only one or two particle species, and only one or two pairs of interacting DNA strands, a likely consequence of the lack of a reliable, quantitative interaction model to guide experiments and enable computational studies. Several groups have reported interaction models (17, 23, 27-30) that qualitatively describe the existing interaction measurements based on mapping the temperature-dependent aggregation-disaggregation transition of DNA-labeled nanoparticles (31), microparticles (27, 29, 32-34) and polymers (35), but the interpretation of these types of experiments is necessarily model-dependent. A more direct approach uses optical tweezers to measure the full spatial and temperature dependence of these short-range pair-interactions with exquisite force and spatial resolution (23, 36).

As first demonstrated in 1986, laser light that is focused to a diffraction-limited 'point' can act as a handle to manipulate dielectric particles (37). In a conventional point trap, the force exerted on the trapped object is proportional to the gradient of the intensity. As a result, a trap formed from a beam with a Gaussian intensity profile (TEM00) has a near-harmonic potential at the trap center. Because of their exquisite force and spatial resolution, optical tweezers have revolutionized the study of many fundamental biological processes, including molecular motor translocation (38) and nucleic acid unfolding (39, 40). Most of these point trap approaches, however, require the application of large tensions (> 10 pN) and are ill suited for the study of equilibrium processes at small forces. Line optical tweezers, on the other hand, extend and soften the trapping potential, allowing colloidal particles to diffuse and interact in the absence of applied forces. As a result, they are often used to study weak, thermally accessible colloidal interactions (23, 41, 42). Unfortunately, unlike point traps that routinely achieve sub-nanometer spatial precision, many line optical tweezers instruments have severely degraded spatial resolution (43, 44), limiting their ability to constrain short-range interactions (e.g. DNA-induced pair potentials).

1.4 Dynamics of DNA-Induced Binding and Hybridization Kinetics

In addition to being able to predict the equilibrium phases that result from hybridization of colloidal particles (17), understanding the kinetics of association and growth is equally important for ultimately realizing high-quality, DNA-directed assemblies (24, 45, 46). Specifically, recent theoretical (47, 48) and experimental (24, 26) studies have demonstrated that the ability of individual, interacting particles to readily equilibrate with the surface of a growing crystal, is critically important in determining both the quality and structure of the final ordered assembly. Unfortunately, many experiments looking at DNA-induced binding report slow and anomalous dynamics (23, 49, 50), despite the fact that single molecule measurements of the kinetics of DNA hybridization (51) suggest that DNA-induced, diffusion-limited binding should be readily achievable. These concerns are highlighted by the fact that the nucleation and growth of DNA-directed colloidal crystals takes several days, roughly one hundred times slower than for depletion crystallization (49), and that the kinetics are dependent on the grafted DNA density, suggesting that particle-particle binding is reaction-, rather than diffusion-limited. These slow binding dynamics likely account for many early failures to produce crystalline assemblies, and improving them should help accelerate progress in the field.

1.5 Organization

In Chapter 2, we describe the details and operating principles of a scanning-line optical tweezers instrument that can be used to measure short-range, thermally accessible colloidal interactions with nanometer spatial precision. In Chapter 3, we describe the design, functionalization and characterization of DNA-labeled microparticles. Specifically, we motivate a sequence design protocol for generating short, complementary strands of DNA that obey simple two-state hybridization and melting. We also describe a DNA-functionalization scheme that produces highly stable, homogeneously labeled particles that can be bridged together by Watson-Crick base pairing. In Chapter 4, we report direct measurements of the pair-interaction free energy between colloidal particles bearing one or two complementary sequences of DNA. We also develop a mean-field model that quantitatively captures the full spatial and temperature dependence of these interactions up to binding energies that are relevant for self-assembly (up to 6 k_BT). In Chapter 5, we measure and discuss DNA-mediated binding dynamics between a pair of colloidal particles as a function of their labeling density. We show that densely functionalized particles exhibit diffusion-limited binding and discuss the implications in the context of self-assembly. We also demonstrate that sparsely labeled particles display highly non-exponential binding kinetics and relate this to static heterogeneity in the rupture of individual DNA duplexes. Finally, we use this large data set to test our mean-field model from Chapter 4 and develop a simple extension using binomial statistics. In Chapter 6, we measure DNA-induced colloidal interactions that are mediated by a soluble linker strand. We show that if poorly designed, linker-mediated binding is slow, but can be sped up dramatically by designing slightly thermodynamically asymmetric linkers. In Chapter 7, we extend our discussion from Chapters 5 and 6 and discuss their implications in the context of previously designed 'single-molecule' experiments of DNA hybridization and melting. We also present a generic model that generates highly non-exponential lifetime distributions though a slowly varying, random force and discuss the limits of its appropriateness. Finally, in Chapter 8, we end this thesis with closing remarks about the future of this work.

1.6 References

1. Leunissen ME*, et al.* (2005) Ionic colloidal crystals of oppositely charged particles. *Nature* 437:235-240.
2. Chen Q, Bae SC, Granick S (2011) Directed self-assembly of a colloidal kagome lattice. *Nature* 469:381-384.
3. Glotzer SC, Solomon MJ (2007) Anisotropy of building blocks and their assembly into complex structures. *Nature Materials* 6:557-562.
4. Sacanna S, Irvine WTM, Chaikin PM, Pine DJ (2010) Lock and key colloids. *Nature* 464:575-578.
5. Seeman NC (1982) Nucleic-Acid Junctions and Lattices. *Journal of Theoretical Biology* 99:237-247.
6. Mirkin CA, Letsinger RL, Mucic RC, Storhoff JJ (1996) A DNA-based method for rationally assembling nanoparticles into macroscopic materials. *Nature* 382:607-609.
7. Alivisatos AP*, et al.* (1996) Organization of 'nanocrystal molecules' using DNA. *Nature* 382:609-611.
8. Watson JD, Crick FHC (1953) Molecular Structure of Nucleic Acids - a Structure for Deoxyribose Nucleic Acid. *Nature* 171:737-738.
9. Owczarzy R*, et al.* (1997) Predicting sequence-dependent melting stability of short duplex DNA oligomers. *Biopolymers* 44:217-239.
10. SantaLucia J, Turner DH (1997) Measuring the thermodynamics of RNA secondary structure formation. *Biopolymers* 44:309-319.
11. SantaLucia J, Hicks D (2004) The thermodynamics of DNA structural motifs. *Annual Review of Biophysics and Biomolecular Structure* 33:415-440.
12. Zuker M (2003) Mfold web server for nucleic acid folding and hybridization prediction. *Nucleic Acids Research* 31:3406-3415.
13. Zadeh JN*, et al.* (2011) NUPACK: Analysis and Design of Nucleic Acid Systems. *Journal of Computational Chemistry* 32:170-173.
14. Yurke B, Turberfield AJ, Mills AP, Simmel FC, Neumann JL (2000) A DNA-fuelled molecular machine made of DNA. *Nature* 406:605-608.
15. Gu HZ, Chao J, Xiao SJ, Seeman NC (2010) A proximity-based programmable DNA nanoscale assembly line. *Nature* 465:202-U286.
16. Zheng JP*, et al.* (2009) From molecular to macroscopic via the rational design of a self-assembled 3D DNA crystal. *Nature* 461:74-77.
17. Tkachenko AV (2002) Morphological diversity of DNA-colloidal self-assembly. *Physical Review Letters* 89:148303.
18. Nykypanchuk D, Maye MM, van der Lelie D, Gang O (2008) DNA-guided crystallization of colloidal nanoparticles. *Nature* 451:549-552.
19. Park SY*, et al.* (2008) DNA-programmable nanoparticle crystallization. *Nature* 451:553-556.

20. Maye MM, Kumara MT, Nykypanchuk D, Sherman WB, Gang O (2010) Switching binary states of nanoparticle superlattices and dimer clusters by DNA strands. *Nature Nanotechnology* 5:116-120.
21. Jones MR*, et al.* (2010) DNA-nanoparticle superlattices formed from anisotropic building blocks. *Nature Materials* 9:913-917.
22. Cigler P, Lytton-Jean AKR, Anderson DG, Finn MG, Park SY (2010) DNA-controlled assembly of a NaTl lattice structure from gold nanoparticles and protein nanoparticles. *Nature Materials* 9:918-922.
23. Biancaniello PL, Kim AJ, Crocker JC (2005) Colloidal interactions and self-assembly using DNA hybridization. *Physical Review Letters* 94:058302.
24. Kim AJ, Scarlett R, Biancaniello PL, Sinno T, Crocker JC (2009) Probing interfacial equilibration in microsphere crystals formed by DNA-directed assembly. *Nature Materials* 8:52-55.
25. Macfarlane RJ*, et al.* (2011) Nanoparticle Superlattice Engineering with DNA. *Science* 334:204-208.
26. Ung MT, Scarlett R, Rogers WB, Sinno T, Crocker JC (2011) Diffusionless transformations and real-space crystallography of DNA-directed colloidal crystals. *Submitted*.
27. Valignat MP, Theodoly O, Crocker JC, Russel WB, Chaikin PM (2005) Reversible self-assembly and directed assembly of DNA-linked micrometer-sized colloids. *Proceedings of the National Academy of Sciences of the United States of America* 102:4225-4229.
28. Licata NA, Tkachenko AV (2006) Statistical mechanics of DNA-mediated colloidal aggregation. *Physical Review E* 74:041408.
29. Dreyfus R*, et al.* (2010) Aggregation-disaggregation transition of DNA-coated colloids: Experiments and theory. *Physical Review E* 81:041404.
30. Leunissen ME, Frenkel D (2011) Numerical study of DNA-functionalized microparticles and nanoparticles: Explicit pair potentials and their implications for phase behavior. *Journal of Chemical Physics* 134:084702.
31. Jin RC, Wu GS, Li Z, Mirkin CA, Schatz GC (2003) What controls the melting properties of DNA-linked gold nanoparticle assemblies? *Journal of the American Chemical Society* 125:1643-1654.
32. Dreyfus R*, et al.* (2009) Simple Quantitative Model for the Reversible Association of DNA Coated Colloids. *Physical Review Letters* 102:048301.
33. Leunissen ME*, et al.* (2009) Switchable self-protected attractions in DNA-functionalized colloids. *Nature Materials* 8:590-595.
34. Leunissen ME, Dreyfus R, Sha R, Seeman NC, Chaikin PM (2010) Quantitative Study of the Association Thermodynamics and Kinetics of DNA-Coated Particles for Different Functionalization Schemes. *Journal of the American Chemical Society* 132:1903-1913.
35. Park SY, Gibbs-Davis JM, Nguyen SBT, Schatz GC (2007) Sharp melting in DNA-linked nanostructure systems: Thermodynamic models of DNA-linked polymers. *Journal of Physical Chemistry B* 111:8785-8791.

36. Rogers WB, Crocker JC (2011) Direct measurements of DNA-mediated colloidal interactions and their quantitative modeling. *Proceedings of the National Academy of Sciences of the United States of America* 108:15687-15692.
37. Ashkin A, Dziedzic JM, Bjorkholm JE, Chu S (1986) Observation of a Single-Beam Gradient Force Optical Trap for Dielectric Particles. *Optics Letters* 11:288-290.
38. Svoboda K, Block SM (1994) Biological Applications of Optical Forces. *Annual Review of Biophysics and Biomolecular Structure* 23:247-285.
39. Liphardt J, Onoa B, Smith SB, Tinoco I, Bustamante C (2001) Reversible unfolding of single RNA molecules by mechanical force. *Science* 292:733-737.
40. Liphardt J, Dumont S, Smith SB, Tinoco I, Bustamante C (2002) Equilibrium information from nonequilibrium measurements in an experimental test of Jarzynski's equality. *Science* 296:1832-1835.
41. Verma R, Crocker JC, Lubensky TC, Yodh AG (1998) Entropic colloidal interactions in concentrated DNA solutions. *Physical Review Letters* 81:4004-4007.
42. Crocker JC, Matteo JA, Dinsmore AD, Yodh AG (1999) Entropic attraction and repulsion in binary colloids probed with a line optical tweezer. *Physical Review Letters* 82:4352-4355.
43. Roichman Y, Grier DG (2006) Projecting extended optical traps with shape-phase holography. *Optics Letters* 31:1675-1677.
44. Tietjen GT, Kong YP, Parthasarathy R (2008) An efficient method for the creation of tunable optical line traps via control of gradient and scattering forces. *Optics Express* 16:10341-10348.
45. Licata NA, Tkachenko AV (2006) Errorproof programmable self-assembly of DNA-nanoparticle clusters. *Physical Review E* 74:041406.
46. Lukatsky DB, Mulder BM, Frenkel D (2006) Designing ordered DNA-linked nanoparticle assemblies. *Journal of Physics-Condensed Matter* 18:S567-S580.
47. Scarlett RT, Crocker JC, Sinno T (2010) Computational analysis of binary segregation during colloidal crystallization with DNA-mediated interactions. *Journal of Chemical Physics* 132.
48. Scarlett RT, Ung MT, Crocker JC, Sinno T (2011) A mechanistic view of binary colloidal superlattice formation using DNA-directed interactions. *Soft Matter* 7:1912-1925.
49. Kim AJ, Biancaniello PL, Crocker JC (2006) Engineering DNA-mediated colloidal crystallization. *Langmuir* 22:1991-2001.
50. Xu Q, Feng L, Sha R, Seeman NC, Chaikin PM (2011) Subdiffusion of a Sticky Particle on a Surface. *Physical Review Letters* 106.
51. Bonnet G, Krichevsky O, Libchaber A (1998) Kinetics of conformational fluctuations in DNA hairpin-loops. *Proceedings of the National Academy of Sciences of the United States of America* 95:8602-8606.

Chapter 2

Measuring Colloidal Interaction with Scanning-Line Optical Tweezers

2.1 Introduction

Optical trapping techniques present a noninvasive way to manipulate microscopic objects using a tightly focused laser beam (1). Because of their exquisite force and spatial resolution, optical tweezers have revolutionized biophysics, allowing precise and direct measurement of many biological processes, including enzyme translocation (2) and single-molecule unfolding (3, 4). Optical tweezers have also become an important tool for research in soft condensed matter physics (5) and are often used in the study of colloidal and surface forces. An interesting class of optical tweezers called line optical tweezers (LOT) or line traps, where the optical trap is elongated in one-dimension, has been used to measure weak, thermally accessible inter-particle pair-interaction potentials (6-8). Previously, these line tweezers have been formed by rapidly scanning a point-like optical trap with rotating mirrors (9, 10), galvanometer-driven mirrors (8, 11), or acousto-optical deflectors (12), or by introducing an anamorphic trap magnification through beam shaping (13) or holography (14, 15). Unfortunately, many of these approaches result in instruments that are difficult to operate and align, or suffer from poor spatial resolution (roughly 10-20 nm) that results from slow scan speeds, unaccounted for optical aberrations or inefficient use of available laser power. With those concerns in mind, we designed a time-shared line optical tweezers instrument that is cheap to build, easy to operate, and has superior spatial and temporal resolution.

This chapter discusses a specific implementation of a time-shared line optical trap that combines a resonant scanning mirror (RSM) and an acousto-optic modulator (AOM). The RSM is used to generate a time-averaged elongated trapping potential by rapidly scanning a point optical trap back and forth. The AOM is used to modulate the instantaneous brightness of the trapping laser synchronously with the scan to control the trapping potential in the scan direction. This instrument is ultimately capable of accurately and reliably measuring short-range, thermally accessible colloidal interactions with nanometer spatial precision.

2.2 Line Optical Tweezers

A schematic representation of the full setup is shown in Figure 2.1. A 671 nm wavelength, linearly polarized, diode-pumped solid-state (DPSS) laser (300 mW, SDL-671-300T, Shanghai Dream Lasers) forms an optical trap in the focal plane of an inverted light microscope (DM IRM, Leica Microsystems), where particles can be trapped by gradient forces. We create an extended optical potential by rapidly scanning the trap back and forth with a 16-kHz resonant scanning mirror (SC-30, Electro-Optical Products Corporation) that is imaged onto the back aperture of a microscope objective (Plan-Apo, 100x, numerical aperture, NA = 1.4, Leica Microsystems) by a 10x magnification Keplarian telescope (f_1 = 50 mm, f_2 = 500 mm, spherical, plano-convex lenses, ThorLabs). While scanning, we modulate the trap intensity synchronously with a LabVIEW controlled acousto-optic modulator (MT-110-VIS, Electro-Optical Products Corporation) to tailor the time-averaged intensity profile along the line. A half-wave plate upstream from the AOM can rotate the trapping laser's polarization to optimize the coupling to and efficiency of the AOM. The zeroth-order beam exiting the AOM ultimately forms the optical trap; the higher-order beams are sent to a beam block. A microscope slide just after the AOM reflects a small portion of the trapping light onto a high-speed photodetector (DET36A, ThorLabs) to monitor the instantaneous brightness. Another half-wave plate, positioned downstream from the RSM, can rotate the laser's polarization again to control any polarization-sensitive optical forces acting on the trapped particles. The trapping beam is ultimately coupled to the optical path of the inverted light microscope by a dichroic mirror (Z670BCM, Chroma Technology Corp.) that is mounted onto the fluorescence module carousel. Finally, trapped particles are imaged by a high-speed digital camera (Phantom 4, Visual Research) under high-brightness Kohler laser illumination. Details of the digital camera, relay optics and laser illuminator are published elsewhere (13).

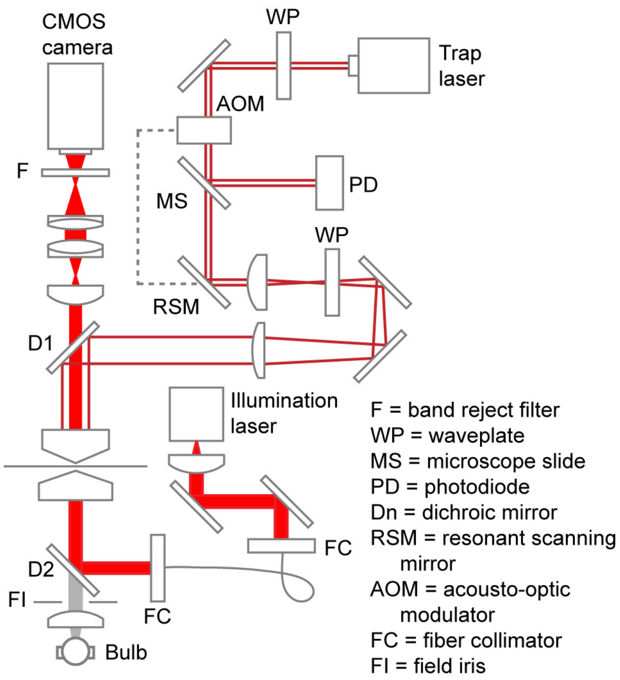

Figure 2.1. Schematic diagram of the scanning-line optical tweezers setup combining an RSM and an AOM.

2.3 Trap Elongation, Intensity Modulation and Waveform Generation

2.3.1 Resonant Scanning Mirror

The RSM is used to steer the trapping beam into the 10x magnification Keplarian telescope as shown in Figure 2.2. The telescope images the mirror surface onto the back aperture of the microscope objective so that a rotation of the mirror through an angle θ_{RSM} corresponds to a rotation of the beam at the aperture of θ_{OBJ} and an in-plane translation of the optical trap. The RSM has a maximum deflection angle of $\theta_{RSM}^{\max} = 2.5°$ (5° peak-to-peak) that corresponds to a maximum rotation of $\theta_{OBJ}^{\max} = (f_1 / f_2)\theta_{RSM}^{\max} = 0.25°$ at the back aperture and an in-plane displacement of approximately ±6 µm.

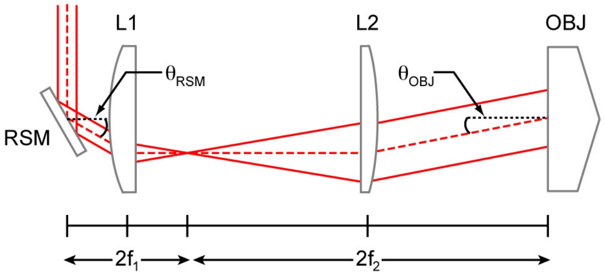

Figure 2.2. The rotation angle θ_{RSM} of the resonant scanning mirror RSM results in a tilt θ_{OBJ} at the back aperture of the microscope objective OBJ.

2.3.2 Acousto-Optic Modulator Characterization

The AOM is phase-locked to the RSM and is used to control the intensity of the trapping laser synchronously as it is scanned back and forth in the focal plane. The maximum modulation frequency is limited by the time required for the acoustic wave to travel through the beam (~1 mm diameter) and is ~1 megahertz in this setup. A Bragg configuration of the AOM crystal and input laser gives a single first-order output beam and a colinear zeroth-order beam, whose intensity I is directly related to the power of the radiofrequency (RF) control signal (ultimately controlled by an external voltage signal V ranging between 0-5 V). Figure 2.3 shows a calibration of I/I_0 as a function of V/V_{max}, where I_0 is the output intensity in the absence of any modulation and $V_{\max} = 5\text{V}$. The calibration curve is fitted-well by $I(V)/I_0 = 1 - A\sin^2(BV/V_{\max})$.

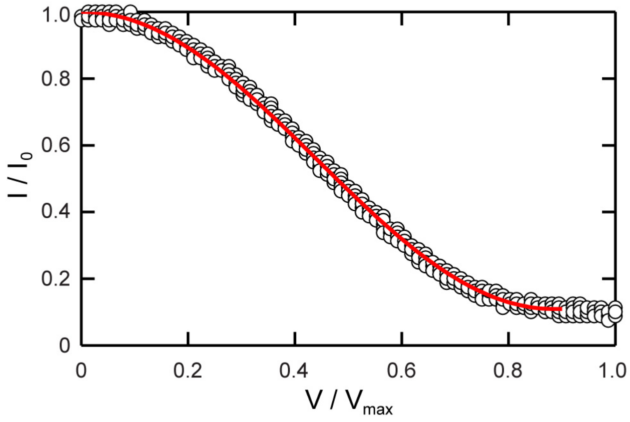

Figure 2.3. A calibration curve of the AOM response to an input voltage. The relative intensity I/I_0 can be modulated from 1-0.1 by changing the input voltage from 0-V_{max} (V_{max} = 5V). The AOM response is fitted-well by $I(V)/I_0 = 1 - A\sin^2(BV/V_{\max})$ and this calibration is used to generate all subsequent waveforms.

2.3.3 Waveform Design and Use

The relative in-plane displacement $x/x_{\max}$ of the optical trap is given by $x(t)/x_{\max} = \sin 2\pi\omega t$, where ω is the resonant frequency of the RSM and $x_{\max}$ is the maximum trap displacement ($x_{\max}$ can be adjusted between 0-6 μm). As a result, in the absence of any modulation of the trapping laser, the time-averaged relative intensity along the scan direction follows $I(x)/I_0 = 1/\sqrt{1-(x/x_{\max})^2}$. That is, the time-averaged intensity is brightest at the 'ends' because the RSM naturally slows as it approaches $\theta_{RSM}^{\max}$ before turning back. To compensate and generate a line trap with a uniform time-averaged intensity, for example, the trapping laser must be modulated in phase with the RSM according to $I(t)/I_0 = \left|\cos 2\pi\omega t\right|$.

To demonstrate the utility of our scanning-line optical tweezers instrument, we generate a family of modulation waveforms (Figure 2.4) that produce parabolic time-averaged intensity profiles of the form $I(x)/I_0 = 1 - 1/2k_{trap}(x/x_{trap})^2$ and associated harmonic trapping potentials $U(x) \propto -I(x)$, where k_{trap} is a user-specified spring constant that can vary between 0-2. The line length is held constant at ~5 μm. To characterize the optical trapping potentials experienced by colloidal particles, we passively observe and track (16) the Brownian motion of single trapped one-micron diameter polystyrene microspheres in 1x TE buffer (10 mM Tris/ 1 mM EDTA/pH = 8.0). The potential along the scan direction $U(x)$ is extracted (up to an additive offset) from a histogram of the x-position of the particle's centroid $P(x)$ by inverting the Boltzmann relation $P(x) \propto \exp[-U(x)/k_B T]$. Figure 2.4b shows three representative parabolic trapping potentials for k_{trap} = [0.2, 0.4, 1.6]. For a parabolic trapping potential $U(x)$, the x positions explored by a diffusing particle are normally distributed with a standard deviation σ_x that is related to the trap's spring constant by $\sigma_x \propto k_{trap}^{-1/2}$, as demonstrated in Figure 2.4c. In this way, we are able to tune the stiffness of the extended harmonic potential by simply changing the user-specified spring constant of the modulation waveform. As demonstrated later, this provides a convenient way of tuning the optical forces between a pair of interacting particles. Lastly, the time-averaged intensity profile $I(x)$ need not be parabolic and can be defined arbitrarily by the user, if so desired.

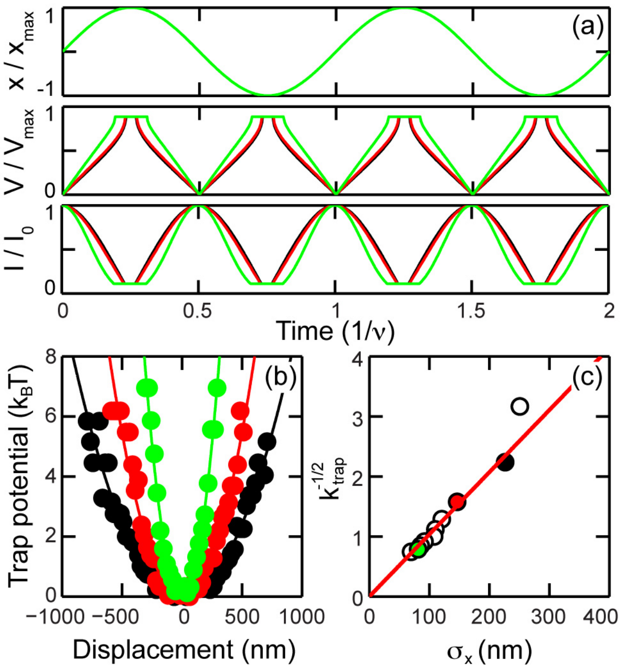

Figure 2.4. Demonstration of a tunable harmonic line trap. (a) The relative scan position x/x_{max}, modulation voltage V/V_{max}, and trap intensity I/I_0 as a function of time for three different spring constants: $k_{trap} = 0.2$ (black), $k_{trap} = 0.4$ (red) and $k_{trap} = 1.6$ (green). The trap potentials extracted from videos of diffusing colloidal particles are indeed harmonic (b) and the spring constant scales as $\sigma_x \propto k_{trap}^{-1/2}$, where σ_x is the standard deviation of the particle's centroid position along the scan direction.

2.4 Practical Operation: Warm-up and Alignment

2.4.1 Getting Started

To begin, turn on the driver of the trapping laser (DPSSL Driver, Shanghai Dream Lasers) and its bench-top temperature controller (CSC32, Omega Engineering, Inc.). Set the controller setpoint somewhere between 25-30 °C to minimize mode hopping in the laser cavity. Continue to try different temperatures in this range until mode hopping is reduced to an acceptable level. After about 10 minutes, turn on the AOM driver in continuous-wave (CW) mode with the amplitude adjustment (AM) set to the maximum RF power (P_{max}). It is important that the amplitude be set to P_{max}, as the AOM calibration (Figure 2.3) changes with the RF power amplitude setting. Once the laser comes up to temperature (~20 min), select a modulation waveform and set the scan frequency in LabVIEW. This frequency is ultimately used to drive the RSM, so it must be close to 16 kHz. Next, execute the LabVIEW routine to load the waveform into an arbitrary function generator (33120A, Hewlett Packard) and switch the AOM driver to external modulation (EXT). After another 20 minutes, turn on the RSM driver (PLD-1S, Electro-Optical Products Corportation) with the amplitude turned down to roughly half the maximum deflection angle. Let the mirror oscillate for a few minutes and then try turning up the scan amplitude. If the RSM becomes unstable, turn it off, switch the AOM back to CW, increase the modulation frequency by a few Hz, and repeat until a stable driving frequency is identified. Finally, turn on the high-speed photodetector (PD) and view the PD and RSM deflection (monitor) signals on an oscilloscope (72-6800, Tenma®). Setup the oscilloscope to trigger on the deflection signal and adjust the phase on the RSM driver until the RSM and AOM are synchronized.

2.4.2 Aligning and Focusing the Optical Trap

While warming up the trapping laser, set the microscope objective and condenser heaters' setpoints (Bioptechs) to the desired experimental temperature. Because line optical tweezers are very sensitive to longitudinal spherical aberration (LSA), we use an immersion-oil with an index of refraction n_D = 1.530 at 25°C (Series A, Cargille Labs) to compensate for LSA introduced by our optical train or the microscope objective. While this specific oil nulls LSA at ~25°C, its index of refraction is temperature-dependent (n_D temperature coefficient = -0.000409/ +°C), causing the trap efficiency and focal plane to vary with temperature. As a result, we must compensate for any additional LSA induced when changing the temperature in an experiment. Because changing the oil is somewhat impractical, as it requires that we clean the objective and make a new chamber for each temperature, we adjust the trap focus by translating the final lens *L2* along the optical axis. Specifically, we trap a pair of particles and then slide the lens toward or away from the focal plane until the particles return to focus. In practice, a translation of a few centimeters is sufficient to compensate for a ~10°C temperature change.

Finally, we must correct for any 'tilt' of the trapping laser with respect to optical axis of the microscope objective. To do so, we trap a single particle in an extended harmonic potential and monitor its centroid as it diffuses in the trap. If there is any tilt of the incident trapping light with respect to the objective, the particle will be biased toward one end of the trap or the other. If this is the case, we adjust the angle of incidence by rotating our final mirror, which is positioned on a gimbal mount to provide a pure rotation of the beam, until the particle is centered in the trap. If necessary, the beam can then be recentered in the two lenses, but this alignment is not always necessary.

2.5 Instrument Demonstration and Validation

2.5.1 Pair-Interaction Potential Measurement

To extract pair-interaction potentials from videos of two interacting colloids, we use particle-tracking routines (13, 16) that correct for diffraction blurred overlap to follow the relative separation *h* between two trapped microspheres as they undergo Brownian diffusion. We calculate the equilibrium pair free energy *F*(*h*) between the particles from the probability distribution of their relative separation *P*(*h*) by inverting the Boltzmann relation $P(h) \propto \exp[-F(h)/k_BT]$. The resulting *F*(*h*) contains both the particle-particle pair-interaction potential as well as contributions from the optical trap itself. To prevent the optical contributions from obscuring the short-range physical pair potential of interest, we tune the line-length and/or harmonic spring constant to null the optical forces acting between the particles near contact, and then fit and subtract a smooth function to *F*(*h*) for *h* > 100 nm, according to published methods (13). For the purposes of extracting short-range interactions that have a full interaction range of < 50 nm (e.g. DNA- or depletion-induced attractions), a simple linear fit is sufficient. Each pair-interaction potential that follows is calculated from a *P*(*h*) compiled from 16,288 uncorrelated measurements of the relative separation *h* between the particles.

2.5.2 Spatial Resolution

The ultimate spatial resolution of this particle tracking based system depends on the signal-to-noise ratio of the camera and the in-plane confinement of the trapped particles. In order to measure the full spatial resolution of our instrument, we tracked the separation between the centroids of an irreversibly bound pair or doublet of one-micron diameter polystyrene sulfate microspheres (Figure 2.5a) (17). In the limit of infinite spatial resolution and perfect confinement to the elongated axis, the probability distribution $P(\Delta x)$ should be a delta function centered at the particle's diameter $P(\Delta x) = \delta(\Delta x - 2a)$, where a is the particle radius. Instead, we measure a slightly asymmetric, Gaussian-like distribution with a standard deviation $\sigma_{\Delta x} \approx 2$ nm (Figure 2.5d), a measure of the minimum spatial resolution of our instrument.

To further improve our spatial resolution, we take advantage of the microsphere brightness and geometry of the doublet to estimate the out-of-plane motion of the particles. Because the two lobes of the doublet are irreversibly bound together, the full, three-dimensional separation between their centers Δr must satisfy $\Delta x^2+\Delta y^2+\Delta z^2 = \Delta r^2$, where y and z are the two other orthogonal Cartesian axes that are in and out of the focal plane, respectively. Assuming that the relative integrated intensity between the particles Δm is proportional to their out-of-plane separation Δz, we can relate Δz to Δm by $\Delta z = k(\Delta m-\Delta m_{off})$, where k is a proportionality constant and Δm_{off} is an offset that accounts for slight polydispersity in the particle size or shading of the illumination. For two particles of identical size in a uniform field of illumination, $\Delta m_{off} = 0$.

As shown in Figure 2.5b, we can extract k, Δm_{off} and a by fitting $\sqrt{\Delta x^2 + \Delta y^2} \approx 2a - k^2(\Delta m - \Delta m_{off})^2 / 4a$ to our in-plane doublet data: Δx, Δy and Δm. As expected, we find that the in-plane confinement $\sigma_{\Delta y} \approx 18$ nm is better than the out-of-plane confinement $\sigma_{\Delta z} \approx 40$ nm by roughly a factor of two (Figure 2.5c). We also find that the probability distribution $P(\Delta r)$ is highly Gaussian with a standard deviation of only $\sigma_{\Delta r} \approx 1$ nm, a measure of our maximum spatial resolution (Figure 2.5d). This spatial resolution is more than an order of magnitude better than other line traps formed by holography or beam scanning (8, 14, 15), and ultimately allows us to constrain the separation dependence of our pair-interaction models with great certainty.

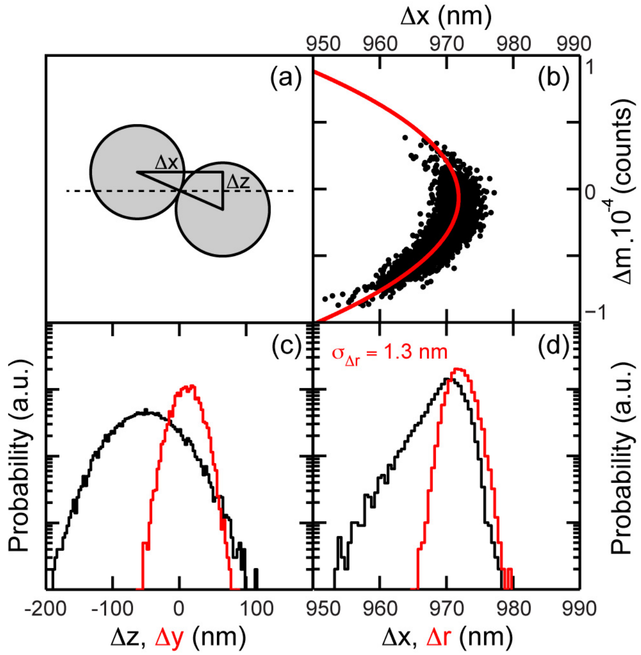

Figure 2.5. Measuring spatial resolution and approximating out-of-plane motion. (a) We trap an irreversible bound doublet particle in an extended optical potential. The *xy* plane is coincident with the microscope focal plane. The *z*-axis is normal to the focal plane. (b) We can extract the out-of-plane motion by fitting (red curve) the relative brightness Δm as a function of in-plane separation Δx. (c) The doublet is highly confined in the *y* direction (red) ($\sigma_{\Delta y} \approx 18$ nm) and slightly less confined in the out-of-plane direction *z* (black) ($\sigma_{\Delta z} \approx 40$ nm). (d) We can achieve a maximum spatial resolution of ~1.3 nm (red) by accounting for out-of-plane motion.

2.5.3 Pair Potential Fitting

To account for and simulate the finite spatial resolution of our optical tweezers instrument, we fit our measured pair-interaction potentials to numerically blurred models of $\Delta F(h)$. First, we convert the model solution of $\Delta F(h)$ into a probability distribution $P(h)$ using the Boltzmann relation $P(h) \propto \exp[-\Delta F(h)/k_B T]$. Next, we numerically convolve $P(h)$ with a Gaussian kernel $G(h)$ (with a standard deviation σ equal to our spatial resolution) to obtain $P_{blur}(h) = P(h) * G(h)$, and then convert $P_{blur}(h)$ back to $\Delta F_{blur}(h)$, again using the Boltzmann relation. Figure 2.6 shows the effects of instrumental blurring on a model $\Delta F(h)$ with well depths or binding energies of 3 $k_B T$ and 6 $k_B T$. In addition to 'softening' the repulsive interaction, blurring also causes a systematic reduction in the observed binding energy: ~10% for σ of 3 nm and ~25% for σ of 5 nm. To verify our spatial resolution and functionality of our instrument, we measure a well-characterized colloidal interaction known as the depletion attraction.

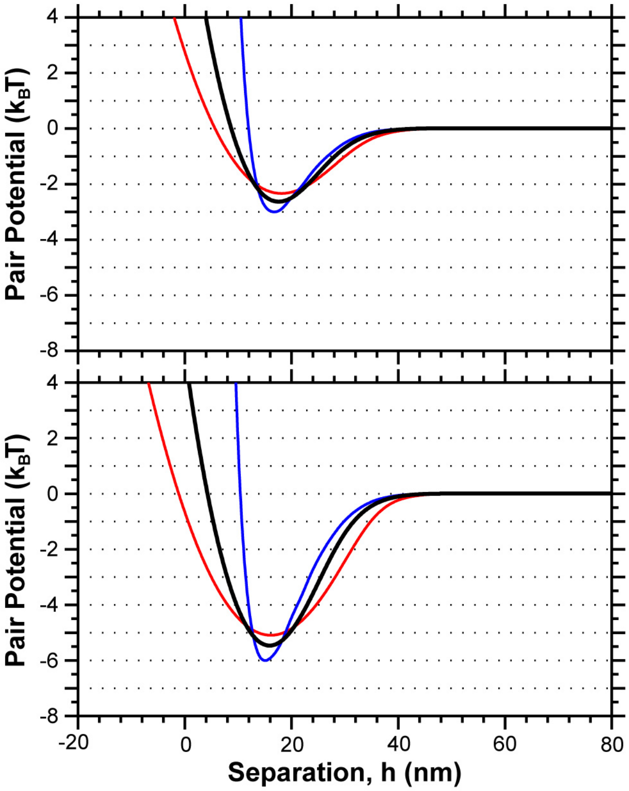

Figure 2.6. Comparison between blurred and unblurred pair-interaction potentials. Computed DNA-mediated pair-interaction potentials for binding energies of 3 k_BT (top) and 6 k_BT (bottom): unblurred (blue), blurred with σ of 3 nm (black), and blurred with σ of 5 nm (red). See Chapter 4 for details on computing DNA-mediated interactions.

2.5.4 The Depletion Interaction: A Case Study

When small, non-adsorbing particles are added to a stable colloidal suspension, the larger colloids experience an induced attraction, due to the unbalanced osmotic pressure arising from exclusion of the smaller particles in regions between colloids (Figure 2.7). This phenomenon is referred to as the depletion attraction and was first introduced theoretically by Asakura and Oosawa in 1954 (18). Since that time, a great deal of work has been done to better understand the specific depletion attraction that results from the presence of micellar or macromolecular depletants (19). In 2000, Piech and Walz (20) showed that for the special case of spherical or spheroidal, charged depletants, the full depletion attraction could be mapped onto the simple hard-sphere potential by substituting an effective size for the hard-core size of the depletant. A similar expression was also introduced by Crocker et al in 1999 (8). This effective size represents the hard-core depletant radius a plus a contribution from the charged double layer d and ranges between 4-5 $\kappa\delta$, where κ^{-1} is the screening length. The original Asakura and Oosawa expression for the depletion interaction energy between to two spheres is given by

$$\frac{F_{AO}(r)}{k_B T} = -\frac{\phi_s}{8a^3}\left[2R+2a-r\right]^2\left(2R+2a+r/2\right); \quad r<2R+2a, \tag{2.1}$$

where r is the distance between the particle centers, ϕ_s is the depletant volume fraction, R is the particle radius and a is the depletant radius. To account for the effective size of the double layer, a is replaced with $a + \delta$ and the volume fraction is adjusted accordingly.

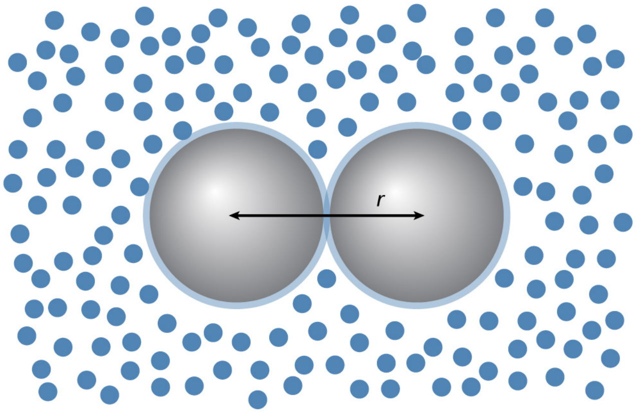

Figure 2.7. An illustration of the depletion interaction. Large particles in a sea of small particles feel an entropic attraction proportional to the overlap of their excluded volumes.

To demonstrate the functionality of our scanning-line optical tweezers instrument, we measured the pair-interaction potentials between a pair of 1.01 micrometer diameter polystyrene sulfate particles in the presence of a background of charged sodium dodecyl sulfate (SDS) micelles. To tune the attractive strength, we varied both the surfactant and salt (NaCl) concentrations in an aqueous buffer of 1x TE. When the concentration of SDS is below the critical micelle concentration (CMC), the pair-interaction should be purely repulsive and described by the Derjaguin-Landau-Verwey-Overbeek (DLVO) theory (21)

$$\frac{F_{DLVO}(r)}{k_B T} = Z^{*2} \lambda_B \left[\frac{e^{2\kappa R}}{(1+\kappa R)^2} \right] \frac{e^{-\kappa r}}{r}, \tag{2.2}$$

where Z^* is the effective surface charge and λ_B is the Bjerrum length (22). For SDS concentrations above the CMC, the depletion attraction should increase linearly with the micelle volume fraction. Moreover, the depth and range of the attraction should also increase as the screening length increases (ionic strength decreases). Figure 2.8 shows measured pair-interaction potentials between PS particles suspended in four different solutions and their corresponding model fits. Each pair potential was fitted to a numerically blurred superposition of Eqs. 2.1 and 2.2, taking δ and the instrument's spatial resolution as free parameters. The fitted $\kappa\delta$ values were 4.1, 4.2 and 4.2 (second from the top, second from the bottom, and bottom, respectively) and are in excellent agreement with the results presented by Piech and Walz, where $\kappa\delta$ ranges between 4-5. Somewhat surprisingly, the spatial resolution needed to fit the four pair potentials accurately (σ_x = 2 nm) is systematically higher than what was measured by tracking the relative separation between a trapped, irreversibly-bound doublet. It is possible that the larger blurring that we observe when measuring real pair-interactions between two distinct particles, rather than the separation between two fused particles, is a result of microsphere roughness or surface charge heterogeneity. In other words, our spatial resolution may no longer be limited by trap efficiency or the signal-to-noise ratio of the camera, and may be, in fact, limited by the effective sphericity of the particles.

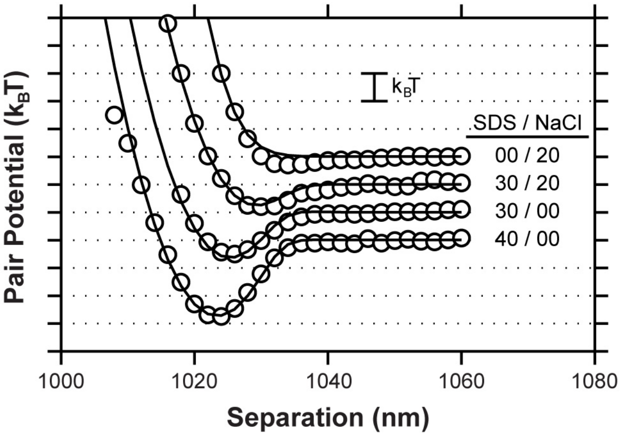

Figure 2.8. Measurements of the micellar depletion interaction. The suspending solutions for each curve, from top to bottom, are: 20 mM NaCl/1xTE, 30 mM SDS/20 mM NaCl/1xTE, 30 mM SDS/1xTE and 40 mM SDS/ 1xTE. The curves have been shifted for clarity. Fits of the data yield $\kappa\delta$ values of 4.1, 4.2, and 4.3 from top to bottom.

2.6 Conclusion

In this chapter, we have developed and demonstrated a versatile scanning-line optical tweezers instrument for measuring the equilibrium interaction potentials between pairs of colloidal microspheres with nanometer resolution. Our instrument is best suited to the study of short-range, weak, thermally accessible interactions due to colloidal forces. We validated our instrument by studying, in the absence of any applied forces, the entropic attraction induced by concentrated solutions of charged micelles. This instrument is equally well suited for studying interactions mediated by adhesion between ensembles of ligand-receptor pairs (e.g. hybridization between surface-grafted complementary ssDNA sequences), and can also be used to study the dynamics of adhesion, either in the context of directed colloidal assembly, or to study hybridization/binding dynamics in the single-molecule limit.

2.7 References

1. Ashkin A, Dziedzic JM, Bjorkholm JE, Chu S (1986) Observation of a Single-Beam Gradient Force Optical Trap for Dielectric Particles. *Optics Letters* 11:288-290.
2. Svoboda K, Block SM (1994) Biological Applications of Optical Forces. *Annual Review of Biophysics and Biomolecular Structure* 23:247-285.
3. Liphardt J, Onoa B, Smith SB, Tinoco I, Bustamante C (2001) Reversible unfolding of single RNA molecules by mechanical force. *Science* 292:733-737.
4. Liphardt J, Dumont S, Smith SB, Tinoco I, Bustamante C (2002) Equilibrium information from nonequilibrium measurements in an experimental test of Jarzynski's equality. *Science* 296:1832-1835.
5. Grier DG (2003) A revolution in optical manipulation. *Nature* 424:810-816.
6. Verma R, Crocker JC, Lubensky TC, Yodh AG (1998) Entropic colloidal interactions in concentrated DNA solutions. *Physical Review Letters* 81:4004-4007.
7. Biancaniello PL, Kim AJ, Crocker JC (2005) Colloidal interactions and self-assembly using DNA hybridization. *Physical Review Letters* 94:058302.
8. Crocker JC, Matteo JA, Dinsmore AD, Yodh AG (1999) Entropic attraction and repulsion in binary colloids probed with a line optical tweezer. *Physical Review Letters* 82:4352-4355.
9. Faucheux LP, Bourdieu LS, Kaplan PD, Libchaber AJ (1995) Optical Thermal Ratchet. *Physical Review Letters* 74:1504-1507.
10. Faucheux LP, Stolovitzky G, Libchaber A (1995) Periodic Forcing of a Brownian Particle. *Physical Review E* 51:5239-5250.
11. Sasaki K, Koshioka M, Misawa H, Kitamura N, Masuhara H (1991) Pattern-Formation and Flow-Control of Fine Particles by Laser-Scanning Micromanipulation. *Optics Letters* 16:1463-1465.
12. Nambiar R, Meiners JC (2002) Fast position measurements with scanning line optical tweezers. *Optics Letters* 27:836-838.
13. Biancaniello PL, Crocker JC (2006) Line optical tweezers instrument for measuring nanoscale interactions and kinetics. *Review of Scientific Instruments* 77:113702.
14. Roichman Y, Grier DG (2006) Projecting extended optical traps with shape-phase holography. *Optics Letters* 31:1675-1677.
15. Tietjen GT, Kong YP, Parthasarathy R (2008) An efficient method for the creation of tunable optical line traps via control of gradient and scattering forces. *Optics Express* 16:10341-10348.
16. Crocker JC, Grier DG (1996) Methods of digital video microscopy for colloidal studies. *Journal of Colloid and Interface Science* 179:298-310.
17. Yake AM, Panella RA, Snyder CE, Velegol D (2006) Fabrication of colloidal doublets by a salting out-quenching-fusing technique. *Langmuir* 22:9135-9141.

18. Asakura S, Oosawa F (1954) On Interaction between 2 Bodies Immersed in a Solution of Macromolecules. *J. Chem. Phys.* 22:1255-1256.
19. Kleshchanok D, Tuinier R, Lang PR (2008) Direct measurements of polymer-induced forces. *Journal of Physics-Condensed Matter* 20.
20. Piech M, Walz JY (2000) Analytical expressions for calculating the depletion interaction produced by charged spheres and spheroids. *Langmuir* 16:7895-7899.
21. Derjaguin B, Landau L (1941) Theory of the stability of strongly charged lyophobic sols and of the adhesion of strongly charged paticles in solution of electrolytes. *Acta Physicochimica URSS* 14:633-662.
22. Crocker JC, Grier DG (1996) When like charges attract: The effects of geometrical confinement on long-range colloidal interactions. *Phys. Rev. Lett.* 77:1897-1900.

Chapter 3

Sample Preparation and Characterization

3.1 Introduction

Since the early 1980s, when automated methods were first developed for synthesizing (1) and amplifying (2) arbitrary DNA sequences, scientists have been repurposing its simple code to generate small libraries of addressable interactions between various nanostructures. Unlike much of the work in 'DNA nanotechology' (3, 4) or 'DNA origami' (5), which aims to make structures built almost exclusively of DNA, assembly of nano- or micron-scale particles by Watson-Crick base-pairing requires the decoration of their surfaces with hundreds or thousands of individual DNA strands (6, 7). While surface functionalizion of gold nanoparticles, a common building block in DNA-directed self-assembly, is relatively straight forward (and mediated by gold-thiol linkages (8)), there are a number of routine methods for grafting polymer microspheres with DNA and other biomolecules.

The two most widespread functionalization schemes use either avidin-biotin ligand-receptor binding (9) or water-soluble carbodiimide chemistry (10). Unfortunately, both of these labeling methods suffer from unsatisfactorily high levels of non-specific binding

(NSB): the first as a result of denatured proteins, and the second as a result of destruction of the carboxylate brush. While many groups choose to ‘patch’ the short-comings of these functionalization schemes, we instead develop a robust physical grafting technique that yields particles that are stable against NSB up to 1 M ionic strength and can be bridged together by DNA hybridization (11). With this approach, we routinely achieve labeling densities of a few thousand DNA molecules per particle, as determined by flow cytometery.

3.2 Materials and Abbreviations

The following section references the materials and abbreviations used throughout the following chapters. Surfactant-free carboxylate-modified latex (CML) particles were obtained from Invitrogen Life Science. Poly(ethylene oxide)-poly(propylene oxide)-poly(ethylene oxide) (PEO-PPO-PEO) triblock copolymer, or Pluronic® F108, was obtained from BASF and used as-is. Short, single-stranded sequences of deoxyribonucleic acid (DNA) were custom synthesized and purified by high-performance liquid chromatography (HPLC) by Integrated DNA Technologies (Coralville, IA). Quantum FITC Low Level flow cytometry standards were obtained from Bangs Laboratories, Inc. (Fishers, IN). Molecular Biology grade 1x TE buffer (10 mM tris-HCl/ 1mM EDTA (ethylenediaminetetraacetic acid)/ pH=8.0) was obtained from Fisher Scientific (Pittsburg, PA). All common reagents and solvents were purchased from either Fisher Scientific or Sigma-Aldrich (St. Louis, MO). HyPure™ Molecular Biology grade water was obtained from Thermo Scientific and used throughout this work.

The following abbreviations are used throughout the text: 4-NPCF (4-nitrophenyl chloroformate), TEA (triethylamine), DCM (dicholormethane), GOPTS (3-glycidyloxypropyl trimethoxysilane), HCl (hydrochloric acid), EtOH (ethanol), ssDNA (single-stranded DNA), dsDNA (double-stranded DNA).

3.3 DNA Sequence Design

Hybridization of appropriately designed, short complementary DNA oligonucleotides can be modeled as a two-state reaction and a nearest-neighbor model (12) is sufficient to predict the stability of the double-stranded (duplex) product formed by Watson-Crick base pairing. All single-stranded DNA sequences used throughout this work were designed to: (i) favor the formation of the ground state duplex upon hybridization with respect to other intermediate duplexes, (ii) minimize secondary structure (e.g. hairpins), and (iii) induce attractive colloidal interactions of order k_BT at 35 °C and 125 mM NaCl. Each surface-bound sequence is composed of a 5'-$(T)_{50}$ spacer followed by a unique 15-base 'handle.' To minimize the formation of undesired intermediate duplexes, the handle sequences were designed so that each three-base motif or codon (e.g. ACC) occurs only once. To avoid self-complementarity, the reverse complement of each codon was not used. Finally, the candidate handle sequences that satisfy (i) and (ii) were screened to find those with the requisite hybridization Gibbs free energy (predicted by the nearest-neighbor model). For example, if the labeling density is 5,000 DNAs per particle, we predict a linker-free binding energy of ~4 k_BT when ΔG_{hyb} is -5 kcal/mol (see Chapters 4 and 5 for details).

In practice, we design our ‘handle’ sequences one nucleotide at a time from the 5’-end to the 3’-end, following a design approach developed by Nadrian Seeman (Figure 3.1). The procedure goes as follows: (i) write down all sixty, three-base motifs (there are only sixty because we exclude the YYY codons, where Y is either A, T, G, or C); (ii) choose one codon at random and eliminate it and its reverse complement from the ensemble (the first chosen codon becomes the first three bases of the sequence); (iii) select another codon at random whose first two nucleotides are the same as the last two nucleotides of the previously selected codon and eliminate it and its reverse complement from the ensemble; (iv) add the last nucleotide of the selected codon to the 3’-end of the growing sequence; and (v) repeat steps iii-iv until you have generated a sequence of the desired length. In practice, it is impossible to generate sequences longer than 32 nucleotides with this strategy.

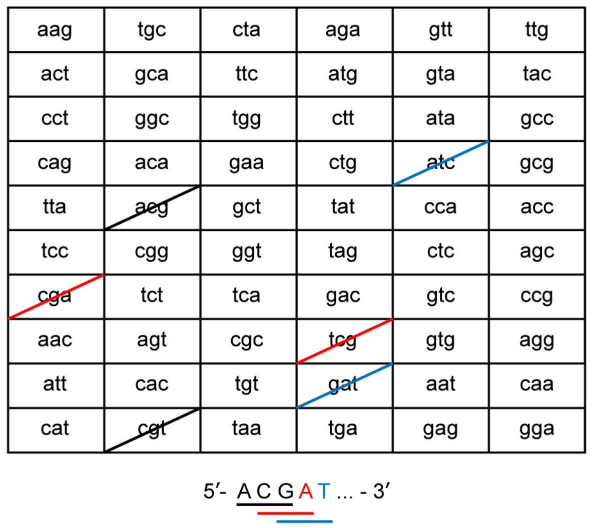

aag	tgc	cta	aga	gtt	ttg
act	gca	ttc	atg	gta	tac
cct	ggc	tgg	ctt	ata	gcc
cag	aca	gaa	ctg	~~atc~~	gcg
tta	~~acg~~	gct	tat	cca	acc
tcc	cgg	ggt	tag	ctc	agc
~~cga~~	tct	tca	gac	gtc	ccg
aac	agt	cgc	~~tcg~~	gtg	agg
att	cac	tgt	~~gat~~	aat	caa
cat	~~cgt~~	taa	tga	gag	gga

Figure 3.1. Sequence design scheme. DNA sequences are designed to favor the formation of the ground state duplex upon hybridization and to minimize secondary structure. The sequences are designed one nucleotide at a time from the ensemble of all possible three base motifs or codons. Each chosen codon and its reverse complement are used only once.

3.4 Particle Functionalization

We synthesize DNA-labeled colloids using a physical grafting technique (11) (Figure 3.2). Briefly, a 5'-amine-modified, 65-oligonucleotide segment of single-stranded DNA is covalently coupled to the terminal ends of an F108 poly(ethylene oxide)-poly(propylene oxide)-poly(ethylene oxide) triblock copolymer. Next, the DNA-labeled copolymer is adsorbed onto the surface of 1.1 micrometer diameter CML colloids and firmly attached by swelling and de-swelling the particles with toluene.

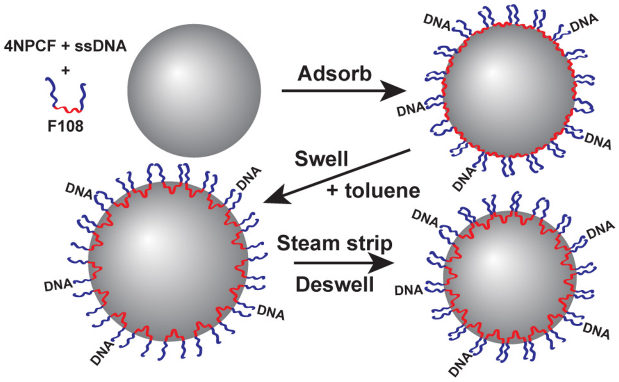

Figure 3.2. Particle functionalization scheme. Short strands of ssDNA are covalently coupled to the terminal ends of a triblock copolymer F108. The DNA-labeled F108 is adsorbed to the surface of polystyrene colloids and firmly attached by swelling and deswelling the particles with toluene. Homogeneity in the labeling density can be increased by lowering the pH of the adsorption buffer below the dissociation constant and isoelectric point of carboxylate and ssDNA, respectively.

Prior to covalent coupling to the 5'-amine-modified ssDNA, the F108 is first activated by reaction with 4-NPCF in ~1% (v/v) TEA/DCM at 0 °C for three hours. The activated-F108 is subsequently precipitated in and washed four times with ~1% (v/v) HCl/EtOH by centrifugation and resuspension at 0 °C. The washed, activated-F108 is then dried in a vacuum desiccator overnight and resuspended at ~1% (w/w) in 10 mM citric acid buffer (pH = 4).

The as-received HPLC purified ssDNA is resuspended in HyPure™ Molecular Biology Grade water to a starting concentration of 1 μM. The 1μM aqueous solution of ssDNA, 1% (w/w) activated-F108 in 10 mM citric acid buffer, and 1 M carbonate buffer (pH = 10) are mixed together in a 15:1:4 volumetric ratio, respectively, and reacted under constant agitation for four hours. After approximately thirty minutes, a yellow color should develop from the production of *p*-nitrophenol, indicating the successful deactivation of activated-F108, either by hydrolysis, or by coupling to ssDNA. The product solution is then added to 1% (v/v) CML colloids in 10 mM citric acid buffer (pH = 4) and the particles are swelled by adding toluene and mixing gently overnight. Finally, the toluene is removed by heating the suspension to ~90 °C for a few minutes, then by washing the particles five times by centrifugation and resuspension in 1x TE buffer. All DNA-labeled particles are stored in aqueous buffer containing 10 mM Tris/1 mM EDTA/pH = 8.0 and are stable at 4 °C for ~1 month.

3.4.1 Buffer Conditions

In the original manuscript detailing the physical grafting technique (11), the 'swelling' step was performed in 1x TE (pH = 8.0) instead of 10 mM citric acid buffer (pH = 4.0). Because the adsorption of DNA-labeled F108 onto the surface of CML microspheres is mediated by hydrophobic-hydrophobic interactions between the PPO center-block and the PS surface, by lowering the pH, we maximize the adhesion 'strength' of adsorbed F108 by uncharging the carboxylate brush (pKa ≈ 5). Moreover, we minimize any electrostatic repulsion between ssDNA and the carboxylate brush by uncharging the ssDNA (pI ≈ 5). Ultimately, changing the 'adsorption buffer' from 1x TE (pH = 8) to 10 mM citric acid buffer (pH = 4) increases the final DNA labeling density in a carboxylate surface density (or 'parking area') dependent way (Figure 3.3), suggesting the existence of an unfavorable carboxylate-ssDNA interaction. In addition to boosting the labeling yield, minimizing the interactions between the DNA-labeled F108 and the carboxylate surface may lead to the production of more uniformly labeled microspheres, as it could erase any memory of already ‘patchy’ carboxylate charges on the particle surface. Interestingly, minimizing electrostatic repulsion between ssDNA and the carboxylate surface by increasing the ionic strength to 100 mM, instead of decreasing the pH, had only a modest effect on the labeling density (increased by ~20%), suggesting that there are more complex interactions at play than just electrostatics.

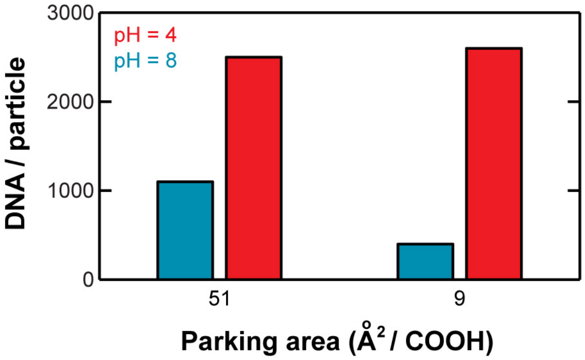

Figure 3.3. Lowering the pH of the ‘swelling buffer’ increases the yield and uniformity of DNA labeling. The carboxylate brush and ssDNA-labeled F108 become uncharged when the solution pH is below their acid dissociation constant (pKa = 5) and isoelectric point (pI = 5), respectively. This maximizes the adhesive ‘strength’ of the adsorbed PPO block and reduces electrostatic repulsion between ssDNA and the carboxylate brush, ultimately boosting the labeling yield by a factor of ~2.5x and ~5x for CML particles with parking areas of 51 Å^2/COOH and 9 Å^2/COOH, respectively.

3.4.2 Stability of the Adsorbed Pluronic Layer

To probe the stability of the adsorbed DNA-pluronic layer, we subjected our DNA-labeled particles to a number of rather strenuous ‘perturbations’ (Figure 3.4). Specifically, we find that the DNA-labeled pluronic, and presumably the neat, adsorbed F108, are unstable at elevated temperature and in the presence of soluble surfactants (including soluble F108). For example, if we heat a 1% (v/v) particle suspension to ~50°C for an hour, we find that the DNA density decreases by ~15%. Moreover, if we heat the sample to ~50°C for an hour and then wash it once by centrifugation and resuspension, the labeling decreases by ~30%, suggesting that desorbed F108 can re-adsorb on experimental timescales. Additionally, if we expose the DNA-functionalized particles to 0.02% (v/v) Tween 20, a common surfactant, we find that roughly 65% of the DNA-labeled F108 molecules are displaced from the particle surface. If we combine the two treatments, we show that we can remove nearly all of the DNA-F108 conjugates, suggesting that the pluronic brush is not physically entangled in the polystyrene matrix, and is loosely complexed to the particle surface. To confirm this hypothesis, we prepared DNA-functionalized particles as described above, but without swelling the particles by addition of toluene. Remarkably, we find that the DNA labeling density is unchanged in the absence of swelling, suggesting that it may be an unnecessary step in the protocol. In either case, to prevent destabilization of the tethered DNA strands, we perform all DNA-assembly experiments and pair-interaction measurements below 40°C and in the absence of any added surfactants.

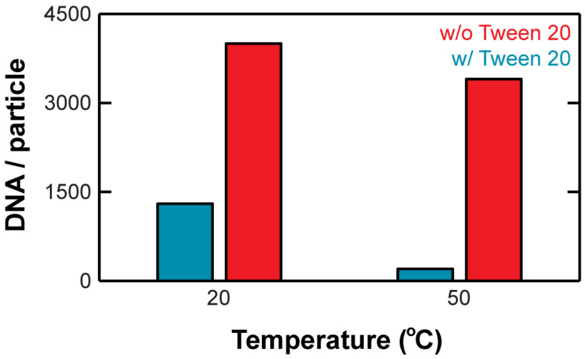

Figure 3.4. Adsorbed DNA-labeled pluronic is unstable at elevated temperatures and in the presence of soluble surfactants. Exposure of DNA-functionalized particles to 0.02% (v/v) Tween 20 (blue) or 1% (w/w) F108 displaces ~65% of the DNA strands at room temperature. At 50°C, nearly all surface-bound ssDNA is washed from the particle surface in the presence of Tween 20. Even in the absence of soluble surfactant (red), heating the particles above 50°C reduces the DNA density by 15-30%. DNA labeling densities were determined by flow cytometry.

We also find that the tethered ssDNA strands (and presumably the F108 brush) are unstable to prolonged exposure to the trapping light. Specifically, we find that the hybridization-induced attraction between a trapped pair of DNA-labeled particles decreases monotonically with time in a trap intensity dependent way. When the DNA-mediated interaction strength is ~3 k_BT, the binding energy decays linearly with a slope of ~0.02 k_BT/min or ~0.01 k_BT/min, when the laser is set to full- or half-power, respectively. The fact that the photodamage is linear in intensity suggests that it is mediated by a single-photon, as opposed to a two-photon, process. Because attempts to slow photodegredation by use of soluble antioxidants were unsuccessful, we limited the trapping time to 5 min for each pair of particles.

3.5 Flow Cytometry

The final DNA labeling densities are quantified using a BD FACScalibur flow cytometer (BD Sciences) and fluorescent calibration standards (Molecular Probes). A calibration curve relating fluorescence intensity to fluorophore number density is first constructed by measuring the fluorescence of three different standards with known fluorophore density (B, 1 and 2) (Figure 3.5a). The cytometer is configured to (i) identify the particle population by adjusting the forward- (FSC) and side-scattering (SSC) detectors' voltage and amplitude gain, and (ii) center the calibration standard's fluorescence signals within the cytometer's dynamic range by adjusting the fluorescein (FL1) detector voltage. To achieve sufficient temporal separation between successive particles as they pass through the detector volume, the calibration standards must be diluted to a volume fraction of ~10^6 particles/ml (<1000 particles/s at the lowest flow rate).

To fluorescently label the DNA-functionalized microspheres, the particles are incubated in a molar excess of short, complementary DNA strands that have been fluorescently modified with 6-FAM phosphoramidite, a common derivative of fluorescein. Again, the now fluorescently-tagged microspheres are diluted to a volume fraction of ~10^6 particles/ml in the same buffer used to dilute the calibration standards, as the fluorescence intensity of fluorescein is highly buffer dependent. Because the scattering intensity of the particles is very sensitive to their size, and the calibration standards are 6 μm in diameter, while our DNA-labeled particles are only 1 μm in diameter, the forward- and side-scattering detectors' voltage and gain must be adjusted to relocate the particle population. The fluorescence detector voltage is left unchanged to preserve the accuracy of the calibration curve.

Table 3.1. Flow cytometer settings. The FSC and SSC voltage and amplitude gain must be adjusted to account for differences in particle size. The FL1 voltage should remain unchanged to preserve the validity of the calibration curve.

	Detector	Voltage	Amp Gain	Mode
6 µm	FSC	E00	7.04	Lin
	SSC	330	1.00	Lin
	FL1	700		Log
1 µm	FSC	E02	7.70	Lin
	SSC	535	1.00	Lin
	FL1	700		Log

Figure 3.5 shows both the calibration curve of fluorophore density versus mean fluorescence intensity, and raw histograms of the fluorescence intensity per particle. The black points and curves correspond to the calibration standards, and the red points and curves correspond to two different samples of DNA-labeled particles. The DNA-density has been modulated between the two samples by diluting the DNA-labeled F108 with pure F108 by a factor of two before adsorption to PS, and subsequent swelling/de-swelling. In this way, we demonstrate that dilution of DNA-labeled F108 with neat F108 is a convenient method to tune the final DNA labeling density.

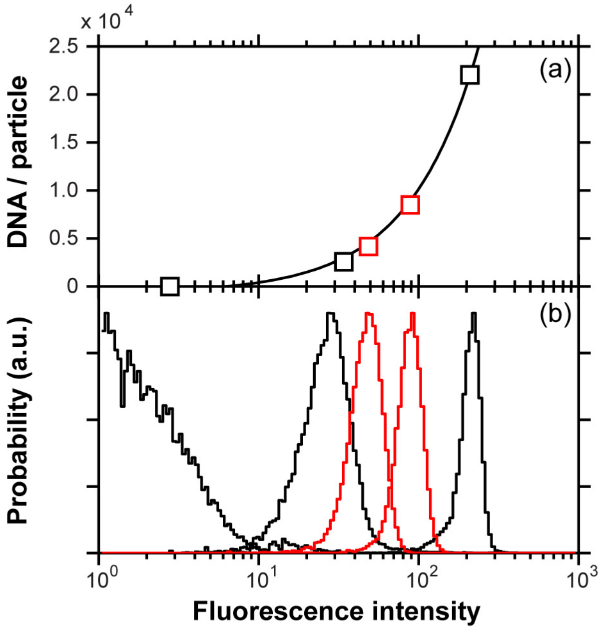

Figure 3.5. Quantification of DNA labeling density with flow cytometry. (a) A calibration curve relating mean fluorescence intensity to fluorophore number density. (b) Histograms of single particle fluorescence for standards B, 1 and 2 (black) and two different samples of DNA-labeled particles (red) that have been tagged with fluorescent, complementary DNA strands. The DNA labeling density can be modulated by dilution of DNA-F108 with neat F108 prior to adsorption and swelling.

3.6 Glass Treatment

To prevent nonspecific binding (NSB) of the DNA-labeled microspheres to the glass coverslip of the microscopy sample chamber, we functionalize the coverslip with a dense poly(ethylene oxide) brush (MW ~8,000 amu). First, the coverslip is dipped into 10% (v/v) GOPTS/xylene and baked in an oven at 100 °C for four hours. Next, the coverslip is washed in acetone, air dried and then baked again at 100 °C for ten minutes. One face of the coverslip is then covered with approximately 200-300 mg of PEG and baked at

100°C overnight. Finally, the PEG melt is washed off with deionized water and the coverslip is stored in a bath of 1% (w/w) PEG in 1x TE buffer.

3.7 Conclusion

In this chapter, we have developed and demonstrated a robust functionalization platform for preparing DNA-labeled polystyrene microspheres that are highly stable against NSB. The dense PEO brush serves two main functions: (i) it provides a strong steric repulsion that stabilizes the particles against aggregation, even at 1 M ionic strength, without the need for 'blockers,' and (ii) it presents the end-grafted ssDNA molecules in a sterically accessible conformation, instead of burying or compressing them near the particle surface. We show that we can tune the DNA labeling density by either changing the starting concentration of DNA prior to reaction, or by diluting the covalently linked DNA-F108 with neat F108 before adsorption and swelling. We also motivate that fact that care must be taken to not destabilize the DNA-labeled pluronic brush. Specifically, assembly experiments should be designed to operate below 40°C and in the absence of any soluble surfactants or other surface-active species. In the future, it may be possible to significantly increase the labeling yield by taking advantage of some common DNA handling protocols used in microbiology (e.g. *in vitro* DNA amplification, ethanol precipitation and purification of DNA-labeled F108 (13), etc.).

3.8 References

1. Caruthers MH (1985) Gene Synthesis Machines - DNA Chemistry and Its Uses. *Science* 230:281-285.
2. Saiki RK*, et al.* (1988) Primer-Directed Enzymatic Amplification of DNA with a Thermostable DNA-Polymerase. *Science* 239:487-491.
3. Seeman NC (2003) DNA in a material world. *Nature* 421:427-431.
4. Shih WM, Quispe JD, Joyce GF (2004) A 1.7-kilobase single-stranded DNA that folds into a nanoscale octahedron. *Nature* 427:618-621.
5. Rothemund PWK (2006) Folding DNA to create nanoscale shapes and patterns. *Nature* 440:297-302.
6. Mirkin CA, Letsinger RL, Mucic RC, Storhoff JJ (1996) A DNA-based method for rationally assembling nanoparticles into macroscopic materials. *Nature* 382:607-609.
7. Alivisatos AP*, et al.* (1996) Organization of 'nanocrystal molecules' using DNA. *Nature* 382:609-611.
8. Gronbeck H, Curioni A, Andreoni W (2000) Thiols and disulfides on the Au(111) surface: The headgroup-gold interaction. *Journal of the American Chemical Society* 122:3839-3842.
9. Green NM (1990) Avidin and Streptavidin. *Methods in Enzymology* 184:51-67.
10. Rogers PH*, et al.* (2005) Selective, controllable, and reversible aggregation of polystyrene latex microspheres via DNA hybridization. *Langmuir* 21:5562-5569.
11. Kim AJ, Manoharan VN, Crocker JC (2005) Swelling-based method for preparing stable, functionalized polymer colloids. *Journal of the American Chemical Society* 127:1592-1593.
12. SantaLucia J, Hicks D (2004) The thermodynamics of DNA structural motifs. *Annual Review of Biophysics and Biomolecular Structure* 33:415-440.
13. Sambrook J, Russell DW (2006) Standard Ethanol Precipitation of DNA in Microcentrifuge Tubes. *Cold Spring Harbor Protocols* 2006:pdb.prot4456.

Chapter 4

DNA-Induced Colloidal Interactions

4.1 Introduction

A promising route to forming novel, nanoparticle-based materials is directed self-assembly, where the interactions among multiple species of suspended particles are intentionally designed to favor the self-assembly of a specific cluster arrangement or nanostructure. DNA provides a natural tool (1-3) for directed particle assembly because DNA double helix formation is chemically specific, i.e. particles with short single-stranded DNA grafted on their surfaces will be bridged together if and only if those strands have complementary base sequences, allowing the two strands to spontaneously hybridize to form double-stranded DNA. Moreover, the temperature-dependent stability of such DNA bridges allows the resulting attraction to be modulated (1, 2) from negligibly weak to effectively irreversible over a convenient range of temperatures. Several groups have recently used such interactions to drive the assembly of three-dimensional, crystalline structures from nanoscopic (4-9) and microscopic (10, 11) particles. Ultimately, we envision a highly versatile nanomaterial design protocol, in which a user-designed matrix of specific interactions among multiple particle species leads to sequential, or even hierarchical, assembly of complex particle structures, controlled by a user-designed thermal program. Unlike this vision of designable, sequential and hierarchical assembly among a significant number of different components, current experiments typically employ only one or two particle species, and only one or two pairs of interacting DNA strands.

We claim that one significant barrier to progress in creating more complex DNA-directed particle assemblies is the lack of a reliable, quantitative interaction model to guide experiments and enable computational studies of structure nucleation, growth or multistep material processing. Several groups have reported interaction models (10, 12-16), all based on capturing the entropic contributions and hybridization thermodynamics of individual grafted DNA molecules. While these models qualitatively describe the existing interaction measurements based on the temperature-dependent aggregation-disaggregation transition of DNA-labeled nanoparticles (17), microparticles (13, 15, 18-20) and polymers (21), or direct measurements with optical tweezers (10), they typically overpredict the interaction strength by roughly two orders of magnitude, corresponding to an unexpectedly large hybridization free energy difference of ~5 k_BT per DNA bridge. Moreover, while the models predict that the interaction strength varies exponentially with temperature, they overestimate the steepness of the temperature dependence by roughly a factor of two. These disappointing findings are all the more surprising, given that DNA is so well understood. The hybridization free energy can typically be estimated *a priori* for any base sequence and its complement to better than 1 k_BT, and the entropic penalties associated with grafting and stretching polymer chains are well-known.

Here we present high precision measurements of the DNA-induced interaction potentials between two microspheres, as a function of particle separation, temperature and DNA composition. Unlike earlier modeling approaches that consider the interacting molecular degrees of freedom explicitly, we employ a mean-field approach based on chemical equilibration between two reactants having static, spatially varying concentration fields, whose form, in turn, is readily computed using a tethered, freely-jointed chain model. Our model quantitatively captures the separation and temperature dependence of the interaction for the first time; it appears that earlier models overpredicted the interactions by not accounting for the spatially varying depletion of unreacted DNA strands in the gap between the particles. A simple generalization of this approach also quantitatively describes the interactions of a more complex but practically important system of spheres functionalized with mixed, interacting DNA strands. The ability to reliably model the interactions between particles with multiple, potentially interacting DNA strands will be key to the development of more complex nanomaterials using DNA-directed assembly.

4.2 Pair Potential Energy Measurements

We synthesize DNA-functionalized colloids using a physical grafting technique described previously (22). Briefly, a 5’-amine-modified, 65-oligonucleotide segment of single-stranded DNA (ssDNA) is covalently coupled to the terminal ends of a poly(ethylene oxide)-poly(propylene oxide)-poly(ethylene oxide) (PEO-PPO-PEO) triblock copolymer. Next, the DNA-labeled copolymer is adsorbed onto the surface of 1.1

micrometer diameter carboxyl-modified polystyrene colloids and firmly attached by swelling and de-swelling the particles with toluene (see Chapter 3). For a typical experiment, we prepare two different populations of DNA-labeled particles, A and B, which are functionalized with complementary sequences of DNA (Figure 4.1a). Each particle is nominally labeled with 5,000 DNA strands and stabilized against nonspecific binding by the dense PEO brush. When two complementary particles come into close contact, $h < 2L$, where h is the relative separation between particles and L is the mean DNA brush thickness, their DNA clouds physically overlap and can hybridize together, inducing a short-range attraction between the spheres (Figure 4.1b). Unlike previous studies that required a soluble linker strand to facilitate hybridization (10), our surface-tethered sequences (Figure 4.1c) are complementary and can hybridize directly, improving the binding kinetics and allowing us to map the spatial dependence of much stronger interactions.

To extract DNA-induced, pair-interaction potentials, we confine two DNA-functionalized particles in an extended optical potential and passively track and histogram their relative separation as they undergo Brownian motion (Figure 4.1d) (see Chapter 2). When the two particles are chemically identical (e.g. A-A or B-B interactions), we observe a diffuse trajectory as the particles bump into one another and explore the underlying optical potential. When the particles are labeled with complementary sequences of DNA (A-B interactions), they follow a different trajectory, transiently binding and unbinding as bridging DNA duplexes form and rupture between the particles. These results highlight the complete chemical specificity of the DNA-induced attraction.

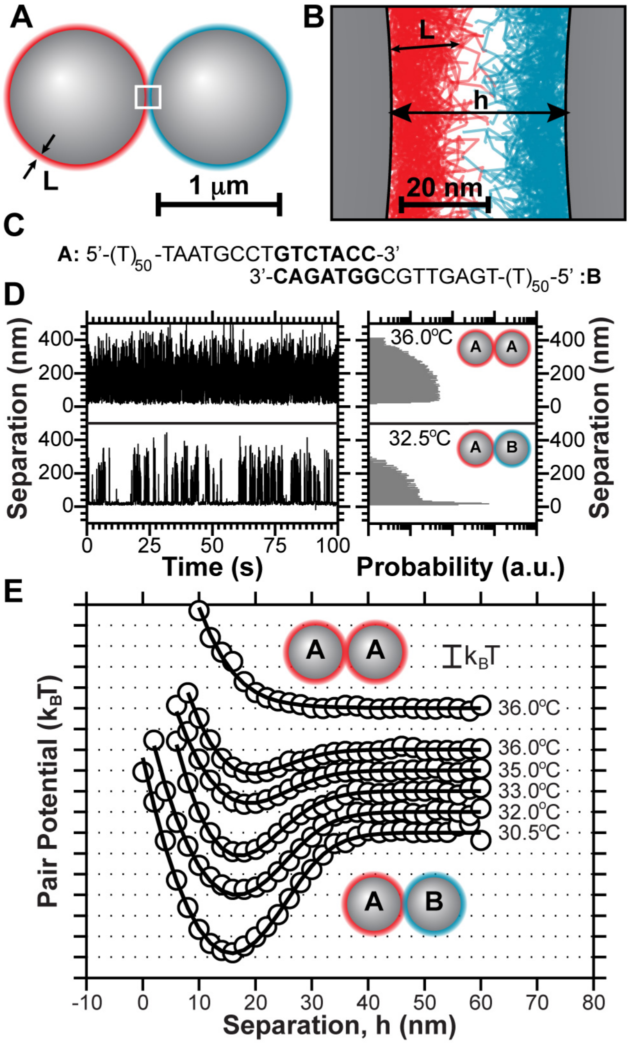

Figure 4.1 Measurement of DNA-mediated colloidal interactions. (A) Grafted ssDNA on two microspheres near contact can hybridize to form bridges (box). (B) Grafted DNA strands form a brush with a mean thickness L ≈ 15 nm. (C) A and B oligonucleotides (red/blue) have a 7-basepair complementary section, 5'-GTCTACC-3'. (D) Experimental separation trajectories and histograms for A-A pairs show no binding, while A-B pairs show intermittent binding. (E) Equilibrium pair-interaction potentials for A-A and A-B interactions as a function of temperature. The circles are experimental data and the solid curves are model fits. A-B pairs show a temperature-dependent attraction and all pairs show a short-range repulsion.

The formation of transient bridges pulls the particles together and leads to the development of a sharp peak in the histogram of relative separation $P(h)$ near $h \approx L$. The equilibrium pair free energy $F(h)$ can be computed from the experimental $P(h)$, up to an additive constant, by inverting the Boltzmann relation $P(h) \propto \exp[-F(h)/k_B T]$, where k_BT is the thermal energy (23). Figure 4.1e shows a representative set of measured pair-interaction potentials. All A-B pair potentials show a temperature-dependent, short-range attraction whose strength decreases monotonically with increasing temperature and a temperature-independent, soft repulsion near contact. The attractive interaction disappears completely at higher temperatures, but under those conditions, it is difficult to discriminate between A-A, A-B and B-B interactions. As a control experiment, we verified that the A-A pair-interaction potential is purely repulsive, confirming the absence of any undesired attractive contributions to the pair potential (e.g. van der Waals, unintended hybridization, or unaccounted for optical forces).

4.3 Thermodynamic Binding Model

Computing the effective pair-interaction of DNA-grafted particles seems daunting at first blush: the confined region between the two microspheres contains scores of interacting random coil macromolecules packed together that undergo complex, reversible, conformational changes during hybridization, and are subjected to time varying forces from two microspheres undergoing coupled rotational and translational diffusion. Upon closer scrutiny, however, several simplifying assumptions break the problem down into conceptually clear and tractable parts. First, bridge formation due to DNA hybridization, while obviously a complex molecular transformation, can be modeled as a "two-state" reaction of the type $A + B \rightleftharpoons AB$, with a sequence-specific free energy change that can be readily computed from the nearest-neighbor (NN) model (24). Second, the forces exerted by the spheres are small enough (< 0.5 pN) to not significantly destabilize double-stranded DNA (25). Third, at typical DNA densities and ionic strengths, chain-chain (excluded volume) interactions are negligible, allowing the configurations of grafted DNA polymers to be easily and reliably modeled as a static ensemble of tethered, freely-jointed chains. Lastly, the DNA density is high enough that each molecule can interact with several others, allowing a mean-field rather than explicitly stochastic description of the bridge formation process.

DNA-induced colloidal interactions arise from two dominant physical effects: (i) transiently forming and breaking DNA bridges act as entropic springs pulling the spheres together and (ii) the compression of unbridged DNA strands when particles come close together acts to push the spheres apart. The first, attractive interaction is the more involved to compute; the second, repulsive interaction can be evaluated from intermediate results derived while computing the first. Ignoring for the moment the effects of DNA brush repulsion and assuming the DNA is in chemical and thermodynamic equilibrium, the free energy change of the combined two-sphere and DNA system satisfies

$$\frac{\Delta F_a(h)}{k_B T} = -\ln\left[P(h)\right] = -\ln\left[1 + \frac{P_{bound}(h)}{P_{free}(h)}\right], \tag{4.1}$$

where $P(h)$ is the probability of finding the spheres separated by a distance h in equilibrium, and $P_{bound}(h)$ and $P_{free}(h)$ describe the separation-dependent probability of there being one or more bridges or no bridges, respectively. This free energy is zero at separations where bridges do not form, by convention. Since $P_{bound} = 1 - P_{free}$, the problem is reduced to computing the probability that no bridges are present (which can be thought of as a time fraction) as a function of separation. If we assume the formation of different bridges is statistically independent and unbounded, the number of bridges k will obey the Poisson distribution

$$P\left(k;\left\langle N_{bridge}\right\rangle\right) = \frac{\left\langle N_{bridge}\right\rangle^{k} e^{-\left\langle N_{bridge}\right\rangle}}{k!}, \tag{4.2}$$

controlled by the h-dependent time-averaged, equilibrium number of bridges $\left\langle N_{bridge}\right\rangle$. The probability that there are no bridges is $P_{free} = P\left(0;\left\langle N_{bridge}\right\rangle\right) = \exp\left(-\left\langle N_{bridge}\right\rangle\right)$ and Eq. 4.1 simplifies to

$$\frac{\Delta F_a}{k_B T} = -\left\langle N_{bridge}\right\rangle. \tag{4.3}$$

Under this approximation, we find that the attractive free energy is simply the time-averaged number of bridges multiplied by the thermal energy, k_BT. Since the $\left\langle N_{bridge}\right\rangle$ that prevails at a given h is the result of a chemical reaction between non-uniformly distributed reactants, this problem consists of two parts: computing the total amount of bridge 'product' in chemical equilibrium and computing the distribution of the DNA 'reactants' themselves.

Since bridge formation is a reversible process, we can compute $\langle N_{bridge} \rangle$ using conventional chemical equilibrium concepts generalized to the case of spatially non-uniform reactants, i.e. by solving the coupled equations

$$\begin{cases} C_{AB}(\vec{r}) = \dfrac{C_A(\vec{r})C_B(\vec{r})}{C_0}\exp\left[-\dfrac{\Delta G_{hyb}}{k_B T}\right] \\ C_A^0(\vec{r}) = C_A(\vec{r}) + C_{AB}(\vec{r}) \\ C_B^0(\vec{r}) = C_B(\vec{r}) + C_{AB}(\vec{r}) \end{cases}, \tag{4.4}$$

where $C_0 = 1M$ is a reference concentration, $C_i(\vec{r})$ is the equilibrium concentration of species i, and ΔG_{hyb} is the hybridization Gibbs free energy for the two-state reaction $A + B \rightleftharpoons AB$. The second two formulae describe mole balances with initial concentrations $C_A^0(\vec{r})$ and $C_B^0(\vec{r})$, which are taken as static, in that they do not vary with the degree of reaction. In essence, we require that chemical equilibrium be satisfied separately at each point $\vec{r}$. The attractive free energy and equilibrium number of bridges between a pair of particles can then be calculated from

$$\frac{\Delta F_a(h)}{k_B T} = -\langle N_{bridge} \rangle = -N_{Av}\int d^3\vec{r}C_{AB}(\vec{r}), \tag{4.5}$$

where N_{Av} is Avogadro's number.

To compute the time-averaged concentration fields of reactants $C_A^0(\vec{r})$ and $C_B^0(\vec{r})$ in the gap between two microspheres, we model the grafted DNA strands as tethered, flexible chains. The DNA strands we use have a contour length (l_c = 40 nm) that is ~8 times the Kuhn length of single-stranded DNA (l_{Kuhn} = 5nm) (26). Specifically, we use Monte Carlo (MC) integration to generate unbiased, 3D random walk configurations consisting of $N = l_c/l_{Kuhn} = 8$ randomly oriented steps. Configurations that intercept either microsphere are rejected as unphysical. The terminal coordinate of the random walk is taken to be the coordinate of the DNA's reactive 'sticky end' (Figure 4.2a). A large ensemble of such random walks (Figure 4.2b) is partitioned to form a discrete approximation to the continuous concentration field $C_i^0(\bar{r})$ (Figure 4.2c). In practice, it is only necessary to generate configurations in the interaction region between the particles (i.e. between two spherical caps), as all other chains on the surface are sterically unavailable for bridge formation.

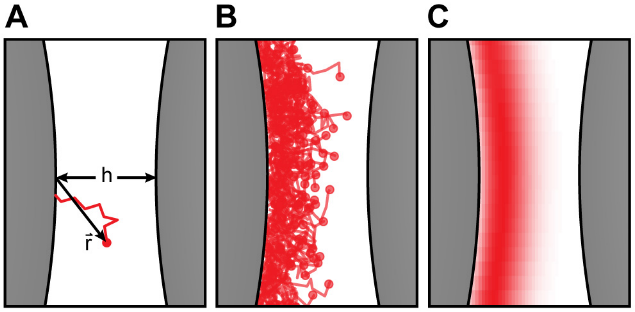

Figure 4.2 Construction of brush polymer ensemble. (*A*) Random walk configuration of a tethered Gaussian coil. The terminal node of the random walk is the coordinate of a point-like DNA sticky end. (*B*) An ensemble of coils, with uniformly distributed anchor points. (*C*) Computed time-averaged concentration field of reactive sticky ends on a discrete grid, 2D slice along centerline.

A subtle but critically important case concerns those polymer configurations that do not intersect the sphere to which they are anchored, but intersect the facing sphere. Since these unphysical configurations must be omitted from the final ensemble, we oversample configurations in the narrow part of the gap, as necessary, until we obtain a uniform areal density of anchor points on the anchoring sphere. This allows us to construct an accurate numerical representation of the local concentration enhancement that occurs when a brush of uniformly distributed grafted strands is compressed. Without resorting to complicated numerical methods, this aspect of the calculation requires generating a new ensemble of brush polymers for each value of the separation h, rather than merely generating one ensemble and translating it as h is varied. Despite this minor complication, generating the necessary ensembles and computing the attractive interaction is readily tractable on a personal computer.

A second important aspect of computing the ensemble of compressed brushes relates to the repulsive part of the DNA-induced interaction. While constructing the ensemble at a given h, we count both the number of tethered coils (that do not intersect the anchor sphere) $\Omega(\infty)$, as well as how many of those coils do not intersect the facing sphere $\Omega(h)$. The entropic repulsion per coil (10) associated with brush compression can then be calculated directly from

$$\frac{\Delta F_r(h)}{k_B T} = -\ln \frac{\Omega(h)}{\Omega(\infty)}. \tag{4.6}$$

The total repulsion between the spheres is then computed by multiplying Eq. 4.6 by the total number of grafted DNA polymers on both particles (to account for compressing two brushes). That is, Eq. 4.6 assumes that the ensemble of coils uniformly covers the entire anchoring sphere. If higher numerical efficiency is desired, a sub-ensemble of chains on a spherical cap can be generated, and both $\Omega(\infty)$ and $\Omega(h)$ can be incremented by the estimated number of coils on the rest of the sphere. Alternatively, approximate forms for the repulsive interaction (10, 27) are available for the case where the particle radius is much larger than the coil. Our formalism presented here, however, is accurate when computing repulsions between nanoscale or non-spherical particles.

The spatially-resolved model predictions of the repulsive and attractive contributions to the DNA-induced pair-interaction potential for the conditions of our experiment are shown in Figure 4.3a. As expected, the attraction becomes significant when the brushes begin to overlap, $h \approx 2L$, and increases monotonically as the particles approach one another. Because we neglect chain-chain interactions, the repulsion has a much shorter range and does not appear until $h < L$. The repulsion is also much larger in magnitude than the attraction for $h < L$, which leads to a peak in $P(h)$ around $h \approx L$, as experimentally observed.

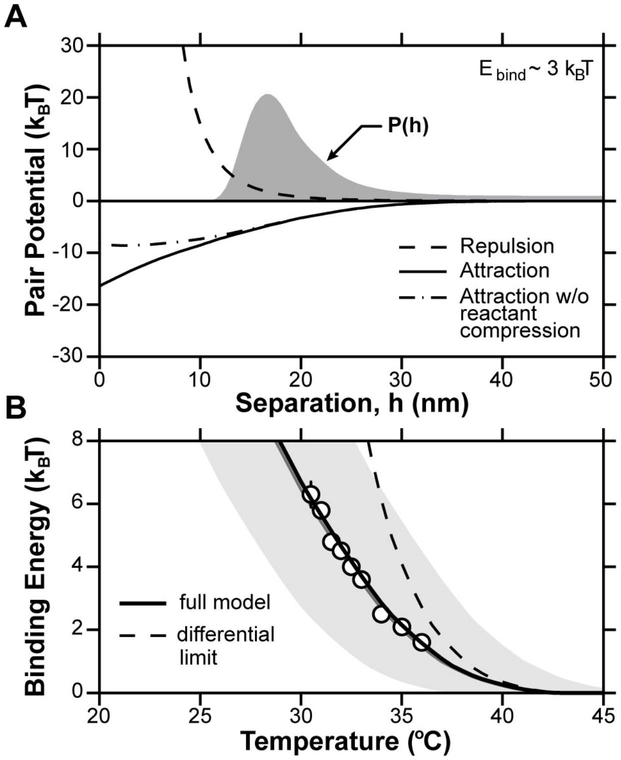

Figure 4.3 Interaction model. (*A*) Computed pair-interaction terms for a binding energy of 3 k_BT: repulsion (dashed curve), full attraction model (solid curve) and approximate attraction neglecting brush compression (dot-dashed curve). P(h) indicates the equilibrium distribution of separations (*B*) Interaction strength or binding energy as a function of temperature. The circles are experimental measurements, each averaged over five pairs. Error bars are determined from the standard error among different pairs. The full interaction model is the solid curve, the dashed curve assumes a differential reaction approximation. The gray band is the full interaction model solution using the nearest-neighbor prediction for ΔG_{hyb}^{NN} (gray curve) delimited by ΔG_{hyb}^{NN} ± 1 k_BT.

Solving Eqs. 4.4-4.6, blurred by our instrumental spatial resolution of ~3 nm (see Chapter 2), we compute and fit the experimentally measured pair-interaction potentials in Figure 4.1e, taking ΔG_{hyb} as a fitting parameter, while allowing particle diameter to fluctuate slightly about its mean value to account for particle polydispersity. The best-fit model predictions are overlaid on the measured pair potentials and capture the full spatial dependence of the pair-interactions at all temperatures. Moreover, when we compare the fitted hybridization Gibbs free energies to *a priori* predictions for ΔG_{hyb} for our sticky ends (5'-GTCTACC-3' and 5'-GGTAGAC-3') from the nearest-neighbor model (24), we find a constant deviation of only -0.03 kcal/mol at all temperatures, well within the uncertainty of the NN model predictions, estimated to have a standard deviation of ~0.5 kcal/mol (24, 28). Figure 4.3b shows the extracted pair-interaction well depths, or binding energies, for all A-B interactions measured, as well as our model predictions using the consensus hybridization Gibbs free energy. Our model quantitatively captures both the magnitude and the temperature dependence of the DNA-induced binding energy (up to 6 k_BT), without any free parameters or empirical corrections, for the first time.

An interesting exercise is to compare the number of bridges that form to the number available to react, readily estimated to be > 50 molecules on each sphere. This estimate suggests that bridge formation could be considered highly unfavorable thermodynamically, and that the $C_i(\vec{r})$ in Eq. 4.4 could be approximated by their initial values $C_i^0(\vec{r})$. Such a "differential reaction" approximation, however, systematically overpredicts the binding energy in a temperature-dependent way (Figure 4.3b). This error is the result of "lumping" the spatial variation of the degree of reaction—when $h \approx L$, the maximum degree of reaction in the center of the gap is actually 30% at 3 k_BT binding strength. Such approximations implicit in earlier models (10, 29) likely account for their failure to capture the correct temperature dependence of the DNA-induced interactions. More sophisticated models (14-16, 18, 20), with explicit molecular degrees of freedom, can capture reactant depletion using binomial statistics, but their generalization to a nonuniform spatial distribution is not obvious. Our nonuniform continuum approach provides a conceptually clearer and systematically more reliable result.

4.4 Particles with Mixed Brushes: Measurements and Models

In general, during a DNA-directed particle self-assembly experiment, an experimenter would like to specify the binding strengths between a number of different particle species, in essence a symmetric matrix of binding strengths, that will necessarily be temperature-dependent. While such a matrix can be specified using soluble linking DNA strands, such approaches may suffer from poor binding kinetics (10). An alternative approach is to attach mixtures of DNA strands having different sequences to each bead species. For example, particle A will bear DNA that is complementary to strands on particle B as well as other DNA strands that are complementary to those on particle C, etc. In this scheme, in order to induce binding between a particle and others of its own kind, the particle will necessarily have to contain DNA strands that can hybridize to other strands on its own surface. Such "self-binding" can lead to loop conformations of hybridized DNA strands that compete with bridging, potentially complicating the interaction thermodynamics.

We now consider interactions where each particle contains mutually complementary DNA sequences. A single population of particles, AB, were functionalized with a mixture of two complementary sequences of DNA (sequences "A" and "B" from before) (Figure 4.4a). Each particle is nominally labeled with ~6,000 DNA molecules and has a mixing ratio $\alpha_{A/B} = 0.4$, i.e. 40% of the surface-bound strands have sequence "A" and the remaining 60% have sequence “B.” In this case, when two AB particles approach one another, $h < 2L$, their now chemically and structurally identical DNA brushes physically overlap and can hybridize together to induce a short-range attraction between the spheres (Figure 4.4b). Figure 4.4c shows a representative set of measured pair-interaction potentials between two mixed, DNA-functionalized colloids as a function of temperature. As was observed for the A-B interactions, all AB-AB pair potentials show a temperature-dependent attraction that decreases monotonically with increasing temperature and the same temperature-independent repulsion. Again, Figure 4.4d shows the temperature dependence of the binding energy. Comparing Figure 4.4d to Figure 4.2b, we immediately see that the temperatures at which the AB-AB interactions are comparable in strength to the A-B interactions are systematically lower by ~6 °C, even though the total DNA content has increased by ~30%.

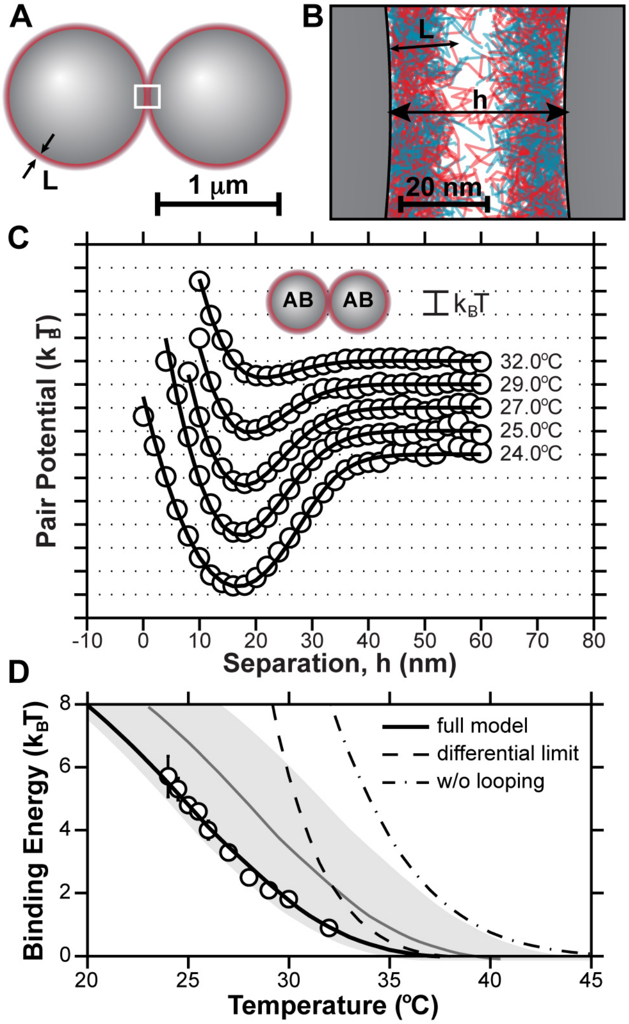

Figure 4.4 Models and experiments for mixed DNA brushes. (*A*) Each of the AB type spheres is labeled with both oligonucleotides, forming a mixed brush, rendered in (*B*). Measured pair-interaction potentials (*C*) for two AB type spheres (circles) with associated model (solid curve), both versus temperature. (*D*) Binding energy as a function of temperature. The circles are experimental measurements, each averaged over five pairs. Error bars are determined from the standard error among different pairs. The full interaction model is the solid curve, the dashed curve assumes a differential reaction approximation, and the dot-dashed curve assumes all hybridized strands are bridges. The gray band is the full interaction model solution using the nearest-neighbor prediction for ΔG_{hyb}^{NN} (gray curve) delimited by ΔG_{hyb}^{NN} ± 1 k_BT.

The explanation for the knockdown in interaction strength at a given temperature is that some of the "A" and "B" strands on a given AB particle surface have hybridized together to form DNA loops (19, 20) rather than bridges. To correct for this effect on the attractive pair-interaction, we first solve for $C_{AB}(\bar{r})$ as described above, then assume that the "A" and "B" strands react to form an unbiased distribution of loops and bridges, which is determined solely by stoichiometry. That is, we estimate the fraction of hybridized strands that are bridges via $f_{bridge}(\bar{r}) = \left[C_{A,L}^{0}(\bar{r})C_{B,R}^{0}(\bar{r}) + C_{A,R}^{0}(\bar{r})C_{B,L}^{0}(\bar{r})\right] / C_{A}^{0}(\bar{r})C_{B}^{0}(\bar{r})$, where $C_{i}^{0}(\bar{r}) = C_{i,L}^{0}(\bar{r}) + C_{i,R}^{0}(\bar{r})$ and $C_{i,L}^{0}(\bar{r})$ and $C_{i,R}^{0}(\bar{r})$ are the contributions to the initial concentration of species *i* from the left and right particle, respectively. The time-averaged number of bridges is then

$$\frac{\Delta F_{a}^{mix}(h)}{k_{B}T} = -\left\langle N_{bridge} \right\rangle = -N_{Av} \int d^{3}\bar{r} f_{bridge}(\bar{r}) C_{AB}(\bar{r}). \tag{4.7}$$

We fit our AB-AB pair-interaction potentials in Figure 4.4c as before, but replacing Eq. 4.5 with Eq. 4.7. Again, our model captures the spatial dependence of the DNA-mediated interaction for all experimental temperatures. Moreover, our model quantitatively captures the temperature dependence of the mixed-DNA binding energy (Figure 4.4d), where the differential approximation and evaluation of Eq. 4.7 that neglects looping fail. This time, when we compare the fitted hybridization Gibbs free energy to predictions for ΔG_{hyb} from the NN model, we find a constant offset of 0.50 kcal/mol at all temperatures. Although this deviation in ΔG_{hyb} is within the *a priori* uncertainty for the NN model, the value is repeatedly different from that found above with unmixed A-B interactions. Since the total density of grafted DNA is higher in this case, we hypothesize that excluded volume effects and chain-chain interactions may cause a slight perturbation to the hybridization thermodynamics.

4.5 Force Sensitivity of DNA Duplex Bridges

Nucleic acid duplexes and hairpins have been shown to be force sensitive. To assess whether or not force sensitivity should be considered when modeling DNA-induced pair-interactions, we estimate the mean entropic tension per bridge f by evaluating

$$f(h) = \frac{1}{\langle N_{bridge} \rangle} \frac{\partial}{\partial h} \Delta F_a(h), \tag{4.8}$$

remembering that $\langle N_{bridge} \rangle$ is itself h-dependent. Evaluating Eq. 4.8 for the A-B pair interactions in Fig. 1*E*, we find that each DNA bridge experiences an average tension ranging from ~0.35 pN at the potential minimum, $h = L$, to ~0.85 pN where $h = 2L$. Because hybridization is accurately modeled as a two-state reaction, the application of force linearly increases the hybridization Gibbs free energy according to $\Delta G_{hyb}(F) = \Delta G^0_{hyb} + F\Delta x$, where ΔG^0_{hyb} is the unforced hybridization Gibbs free energy and Δx is the distance between the hybridized duplex and the transition state along the forced unbinding reaction pathway (30). Force spectroscopy studies of short single DNA duplexes (31) find that Δx scales linearly with the length of the duplex n according to

$$\Delta x = (7 \pm 3)\ \text{Å} + (0.7 \pm 0.3)n\ \text{Å}. \tag{4.9}$$

For our 7-basepair duplex, Δx = 1.2 nm and the correction to the unforced hybridization Gibbs free energy $F\Delta x$ ranges from 0.10 k_BT at $h = L$ to 0.25 k_BT at $h = 2L$. Because the correction to ΔG^0_{hyb} at the potential minimum is significantly less than the uncertainty with which we can estimate ΔG^0_{hyb} (~0.8 $k_B T$) from the nearest-neighbor model, and because the spatial variation in ΔG_{hyb} of 0.15 $k_B T$ over L ~ 15 nm is undetectable given our finite spatial resolution, we omit force sensitivity from our DNA-induced pair interaction model.

4.6 Conclusion

In this chapter, we have shown that the interaction between complementary DNA-labeled particles can be modeled in a mean-field manner as chemical equilibration between two continuous concentration fields, without explicit reference to polymer chain entropy or the necessity of costly many-body dynamical simulation. This approach, founded on basic concepts in polymer physics and statistical mechanics, is able to capture both the spatial and temperature dependence of DNA-induced pair-interactions, while being readily generalizable to particles that are small compared to the DNA strands or have non-spherical shapes, as well as cases where many-body interactions are possible. While we have relied on a numerical approach, we note that our general framework is also amenable to analytic evaluation of the interaction free energy.

The success of our modeling framework relies partially upon the careful design of our experimental system. We used long, flexible ssDNA spacers intentionally, to reduce entropic tension on the bridges and maximize the brush thickness. By using a density of grafted strands that was close to the polymers' critical overlap concentration, we ensured that each strand would be able to sterically access several other polymers, despite being tethered to a solid surface, without introducing excluded volume effects. At a lower coverage of grafted DNA, we expect the actual interaction will be weaker than our continuum predictions, and will likely require an explicitly stochastic model. Beyond modeling convenience, our design choices facilitate a broad interaction well and a consistent mean field interaction without significant static disorder (e.g. due to stochasticity) that, we conjecture, directs efficient self-assembly (3).

In the future, a quantitative understanding of the physical processes that govern DNA-mediated particle binding will be essential for control and design of DNA-directed particle assemblies and materials. The material design space for this versatile technology—particles labeled with DNA—is vast: an engineered matrix of specific interactions between a library of differently sized (and shaped) particle species, whose core chemistry is effectively decoupled from the final structure and assembly processes. The material processing design space is equally vast: the ability to modulate the interactions using thermal schedules (5), added soluble strands (32), enzymes (33), photochemistry (34, 35) and DNA actuators (6, 19) promises a wide variety of schemes for controlling nucleation (29), growth (11), structural transformations (6) and replication (34) to produce useful novel particle-based metamaterials in the form of clusters, bulk crystals, thin films and heterojunctions. Navigating this complex space will rely on simulation, which is now enabled by a framework for computing interparticle interaction matrices reliably, across a range of process conditions.

4.7 References

1. Mirkin CA, Letsinger RL, Mucic RC, Storhoff JJ (1996) A DNA-based method for rationally assembling nanoparticles into macroscopic materials. *Nature* 382:607-609.
2. Alivisatos AP*, et al.* (1996) Organization of 'nanocrystal molecules' using DNA. *Nature* 382:609-611.
3. Crocker JC (2008) Nanomaterials: Golden handshake. *Nature* 451:528-529.
4. Nykypanchuk D, Maye MM, van der Lelie D, Gang O (2008) DNA-guided crystallization of colloidal nanoparticles. *Nature* 451:549-552.
5. Park SY*, et al.* (2008) DNA-programmable nanoparticle crystallization. *Nature* 451:553-556.
6. Maye MM, Kumara MT, Nykypanchuk D, Sherman WB, Gang O (2010) Switching binary states of nanoparticle superlattices and dimer clusters by DNA strands. *Nature Nanotechnology* 5:116-120.
7. Jones MR*, et al.* (2010) DNA-nanoparticle superlattices formed from anisotropic building blocks. *Nature Materials* 9:913-917.
8. Cigler P, Lytton-Jean AKR, Anderson DG, Finn MG, Park SY (2010) DNA-controlled assembly of a NaTl lattice structure from gold nanoparticles and protein nanoparticles. *Nature Materials* 9:918-922.
9. Macfarlane RJ*, et al.* (2011) Nanoparticle Superlattice Engineering with DNA. *Science* 334:204-208.
10. Biancaniello PL, Kim AJ, Crocker JC (2005) Colloidal interactions and self-assembly using DNA hybridization. *Physical Review Letters* 94:058302.
11. Kim AJ, Scarlett R, Biancaniello PL, Sinno T, Crocker JC (2009) Probing interfacial equilibration in microsphere crystals formed by DNA-directed assembly. *Nature Materials* 8:52-55.
12. Tkachenko AV (2002) Morphological diversity of DNA-colloidal self-assembly. *Physical Review Letters* 89:148303.
13. Valignat MP, Theodoly O, Crocker JC, Russel WB, Chaikin PM (2005) Reversible self-assembly and directed assembly of DNA-linked micrometer-sized colloids. *Proceedings of the National Academy of Sciences of the United States of America* 102:4225-4229.
14. Licata NA, Tkachenko AV (2006) Statistical mechanics of DNA-mediated colloidal aggregation. *Physical Review E* 74:041408.
15. Dreyfus R*, et al.* (2010) Aggregation-disaggregation transition of DNA-coated colloids: Experiments and theory. *Physical Review E* 81:041404.
16. Leunissen ME, Frenkel D (2011) Numerical study of DNA-functionalized microparticles and nanoparticles: Explicit pair potentials and their implications for phase behavior. *Journal of Chemical Physics* 134:084702.

17. Jin RC, Wu GS, Li Z, Mirkin CA, Schatz GC (2003) What controls the melting properties of DNA-linked gold nanoparticle assemblies? *Journal of the American Chemical Society* 125:1643-1654.
18. Dreyfus R*, et al.* (2009) Simple Quantitative Model for the Reversible Association of DNA Coated Colloids. *Physical Review Letters* 102:048301.
19. Leunissen ME*, et al.* (2009) Switchable self-protected attractions in DNA-functionalized colloids. *Nature Materials* 8:590-595.
20. Leunissen ME, Dreyfus R, Sha R, Seeman NC, Chaikin PM (2010) Quantitative Study of the Association Thermodynamics and Kinetics of DNA-Coated Particles for Different Functionalization Schemes. *Journal of the American Chemical Society* 132:1903-1913.
21. Park SY, Gibbs-Davis JM, Nguyen SBT, Schatz GC (2007) Sharp melting in DNA-linked nanostructure systems: Thermodynamic models of DNA-linked polymers. *Journal of Physical Chemistry B* 111:8785-8791.
22. Kim AJ, Manoharan VN, Crocker JC (2005) Swelling-based method for preparing stable, functionalized polymer colloids. *Journal of the American Chemical Society* 127:1592-1593.
23. Biancaniello PL, Crocker JC (2006) Line optical tweezers instrument for measuring nanoscale interactions and kinetics. *Review of Scientific Instruments* 77:113702.
24. SantaLucia J, Hicks D (2004) The thermodynamics of DNA structural motifs. *Annual Review of Biophysics and Biomolecular Structure* 33:415-440.
25. Biancaniello PL, Kim AJ, Crocker JC (2008) Long-time stretched exponential kinetics in single DNA duplex dissociation. *Biophysical Journal* 94:891-896.
26. Murphy MC, Rasnik I, Cheng W, Lohman TM, Ha TJ (2004) Probing single-stranded DNA conformational flexibility using fluorescence spectroscopy. *Biophysical Journal* 86:2530-2537.
27. Li DC, Lam CN, Biswal SL (2010) Measuring short-range repulsive forces by imaging directed magnetic-particle assembly title. *Soft Matter* 6:239-242.
28. SantaLucia J, Turner DH (1997) Measuring the thermodynamics of RNA secondary structure formation. *Biopolymers* 44:309-319.
29. Kim AJ, Biancaniello PL, Crocker JC (2006) Engineering DNA-mediated colloidal crystallization. *Langmuir* 22:1991-2001.
30. Evans E, Ritchie K (1997) Dynamic strength of molecular adhesion bonds. *Biophysical Journal* 72:1541-1555.
31. Strunz T, Oroszlan K, Schafer R, Guntherodt HJ (1999) Dynamic force spectroscopy of single DNA molecules. *Proceedings of the National Academy of Sciences of the United States of America* 96:11277-11282.
32. Tison CK, Milam VT (2007) Reversing DNA-Mediated adhesion at a fixed temperature. *Langmuir* 23:9728-9736.
33. Tison CK, Milam VT (2008) Manipulating DNA probe presentation via enzymatic cleavage of diluent strands. *Biomacromolecules* 9:2468-2476.
34. Leunissen ME*, et al.* (2009) Towards self-replicating materials of DNA-functionalized colloids. *Soft Matter* 5:2422-2430.

35. Richards JL, Seward GK, Wang YH, Dmochowski IJ (2010) Turning the 10-23 DNAzyme On and Off with Light. *Chembiochem* 11:320-324.

This chaper has been published as:

Rogers WB, Crocker JC (2011) Direct measurements of DNA-mediated colloidal interactions and their quantitative modeling. *Proceedings of the National Academy of Sciences of the United States of America* 108:15687-15692.

Chapter 5

Dynamics of DNA-mediated binding

5.1 Introduction

In addition to understanding the equilibrium interactions between DNA-labeled particles (1-4), it is also important to consider the dynamics with which they bind to and unbind from one another. Recently, a handful of experimental (5, 6) and theoretical (7-10) studies have demonstrated the importance of these binding dynamics and collective growth kinetics within the context of directed self-assembly. Specifically, the ability of individual, interacting particles to readily equilibrate with the surface of a growing crystal, is critically important in determining both the quality and structure of the final ordered assembly. Unfortunately, much of the experimental work to date regarding DNA-mediated interactions between polymer microspheres raises concerns that DNA-induced binding may be inherently slow (1, 11) or have 'strange' binding kinetics, e.g. power law (1, 12) or stretched exponential (13), which could ultimately frustrate efficient assembly. These concerns are highlighted by the fact that the nucleation and growth of DNA-directed colloidal crystals takes several days, roughly one hundred times slower than for depletion crystallization (11), and that the kinetics are dependent on the grafted DNA density, suggesting that particle-particle binding is reaction-, rather than diffusion-limited. These findings are made all the more surprising, given the fact that single-molecule measurements find that DNA hybridization is rapid compared to microsphere diffusion.

In this chapter, we demonstrate that under the right conditions, carefully designed systems of DNA-functionalized particles exhibit effectively diffusion-limited binding, suggesting that these interactions should be suitable to direct self-assembly, while also validating our mean-field approach from Chapter 4. We explore the transition from diffusion-limited to reaction-limited binding by 'titrating' down the DNA labeling density, and develop a simple dynamic model that is able to reproduce some of the 'strange' kinetics observed in multivalent binding. Specifically, we find that, when compounded, static disorder at the single-molecule level can give rise to highly non-exponential lifetime distributions in processes governed by multivalent interactions. In the future, the ability to modulate and reliably model the DNA-induced binding dynamics will be key to the rational self-assembly of complex nanomaterials. Moreover, our experimental approach can be easily generalized to other relevant systems whose binding is mediated by dynamic ligand-receptor pairs (e.g. cell adhesion and rolling), and can also be extended to access the kinetics of secondary-structure formation at the single-molecule level (e.g. DNA hairpin folding).

5.2 Measurement and Dissection of Binding Trajectories

We use a scanning-line optical tweezers instrument (see Chapter 2) to measure the binding dynamics of DNA-labeled colloids as a function of temperature, interaction strength and DNA strand density. We synthesize DNA-labeled colloids using a physical grafting technique (see Chapter 3), preparing two different populations of particles, A and B, which are functionalized with complementary sequences of DNA. To investigate the effect of DNA labeling density, we prepared four different pairs of populations with decreasing labeling densities by diluting the DNA-labeled pluronic with unlabeled F108 prior to adsorption and swelling with toluene (see Chapter 3). The dilution ratios were 1/1, 1/2, 1/7 and 1/10, yielding nominal labeling densities of 5000, 2500, 700 and 500 DNA/particle, as confirmed by flow cytometery. To maintain reversible binding within our experimentally accessible temperature window (~25-40°C), an additional guanine nucleotide was added to the 'sticky end' sequence used for the 1/7 and 1/10 dilution samples. The two sticky end sequences used were 5'-GTCTACC-3' and 5'-GTCTACCG-3' and all binding experiments were performed in aqueous buffer containing 125 mM NaCl/ 10 mM tris-HCl/ 1mM EDTA/ pH = 8.0.

To extract the kinetics of DNA-mediated binding, we confine two DNA-functionalized particles in an extended harmonic potential and track their relative separation as they undergo Brownian motion (14, 15). When the particles are labeled with complementary sequences of DNA, they transiently bind to and unbind from one another as bridging DNA duplexes form and rupture between the particles. This dynamic binding and unbinding, which is mediated by reversible DNA 'handshaking' is evident in the trajectories of the relative separation h between the microspheres as a function of time (Figure 5.1). Qualitatively, it is clear from these trajectories that the system explores two states (bound b and unbound u) that are characterized by different distributions of h; in the unbound state, $P_u(h)$ is broad and extends over the full trap length, while in the bound state, $P_b(h)$ is constrained to small h.

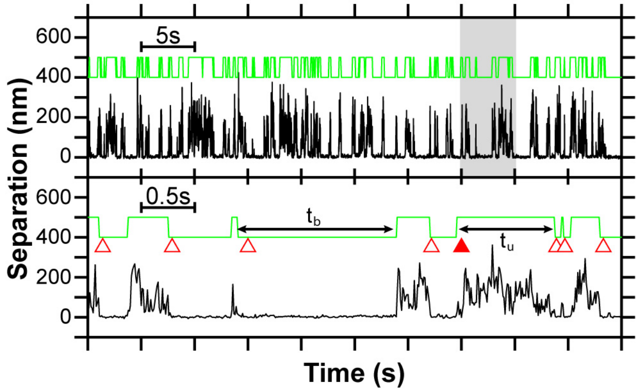

Figure 5.1. An example trajectory of particles binding and unbinding as DNA bridges hybridize and melt dynamically. Experimental separation trajectories (black) that show intermittent binding and unbinding can be dissected to extract the state of the particles (green), which is either bound (low) or unbound (high). We use these trajectories to obtain bound and unbound lifetimes, t_b and t_u, respectively, as a function of the interaction strength, and parameterize our experimental systems according to a measured Damköhler number *Da*. The Damköhler number is determined from the frequency with which the particles stick together (△) or bounce apart (▲) upon collision.

To quantitatively dissect the time-dependent relative separation and determine the state of the system (*b* or *u*) in each frame, we use a three-step approach. First, we threshold the trajectory at h^* and define the logical variable S as $S = h > h^*$, where $S = 1$ if the particles are unbound and $S = 0$ if they are bound. The threshold separation is defined as $h^* = \mu + 2\sigma$, where μ and σ are the mean and standard deviation, respectively, of the best-fit Gaussian distribution of $P(h)$ - 1. Next, we erode any states that have a lifetime of only a single frame (i.e. the particles must unbind for longer than a single frame to be considered unbound). Finally, we use our approximate state trajectory (a time-dependent series of 1s and 0s) to estimate the emission and transition probabilities needed to determine the most likely sequences of states, or Viterbi path, that the particles (a hidden Markov model) traversed (16-18).

5.2.1 Hidden Markov Model

A hidden Markov model is a statistical model in which the system is assumed to be a Markov process with hidden states that are related to an observable token. Each state has a probability distribution (emission probability) of the possible output tokens and probabilities of switching to the other states (transition probability). In our system, there are only two hidden states (either bound b or unbound u) and the observable token is the relative separation h between the microspheres. As mentioned above, we can approximate the two emission probability distributions $P_u(h)$ and $P_b(h)$ from our thresholded trajectory, where $P_i(h)$ is the probability of observing some h when in state i. We can also estimate the transition probabilities $P_t^{i \to j} = \Delta t / \langle t_i \rangle$, where $\langle t_i \rangle$ is the average lifetime of state i and Δt is the time increment between successive frames. Finally, we use the Viterbi algorithm to determine the most likely sequence of hidden states that would result in the sequence of observed h (Figure 5.1). We then iterate the process one more time to refine our Viterbi path. Figure 5.2 shows the final two emission distributions. The shape of the unbound state's emission distribution $P_u(h)$ essentially results from the harmonic potential of the optical trap. The shape of the bound state's emission distribution $P_b(h)$ is controlled by the equilibrium configurations of the DNA bridges tethered between the two microspheres (blurred by our spatial resolution).

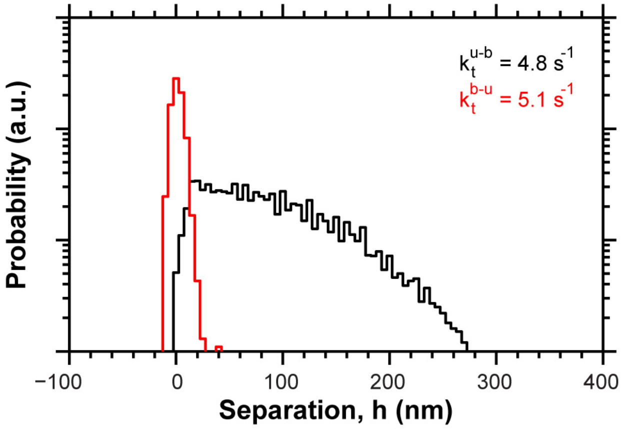

Figure 5.2. Two emission distributions and two transition rates fully specify our Hidden Markov Model (HMM). The unbound state's emission distribution (black) is dictatated by the shape of our optical trapping potential. The bound state's emission distribution (red) is specified by the equilibrium configurations of the tethered DNA bridges.

To validate our approach, we use the same analysis routine to extract imposed bound and unbound lifetime distributions of a simulated trajectory (Figure 5.3a). To construct the mock trajectory, we use Monte Carlo to generate the time-evolution of the state of a system with lifetime distributions $P(t_b) \propto t_b^{-1} \exp(-t_b / \tau_b)$ and $P(t_u) \propto \exp(-t_u / \tau_u)$ for the bound and unbound state, respectively. Next, we discretize the state trajectory into individual frames, and sample a token separation h from the relevant emission distribution $P_i(h)$ for each frame (Figure 5.3b). Finally, we run the simulated token trajectory through our analysis routine to extract the bound and unbound lifetime distributions (Figure 5.3c). Remarkably, even though the bound lifetime distribution is significantly non-exponential, we find that this approach is able to accurately extract the bound lifetime distribution without significantly distorting the unbound lifetime distribution. While the emission distributions, normal and uniform for the bound and unbound states, respectively, are somewhat idealized in this example, they do in fact closely resemble the experimental distributions and this validation works equally well for even more realistic distributions.

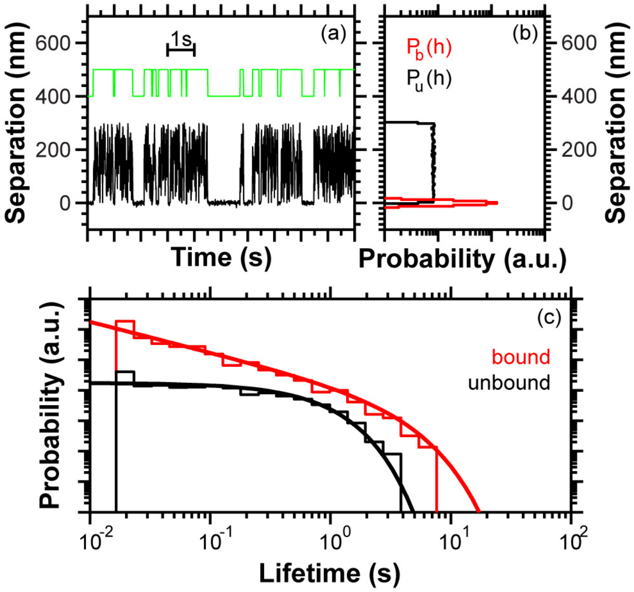

Figure 5.3. A mock experiment. We generate a simulated trajectory of the relative separation *h* as a function of time (a) from simple emission distributions: uniform and normal for the unbound and bound states, respectively (b). Our analysis routine is able to recover the imposed lifetime distributions for the unbound (black) and bound (red) states, without significant distortion, even though they are not necessarily exponential.

5.2.2 Damköhler Analysis

To parameterize our different experimental conditions, we define a Damköhler number *Da* as a ratio of the forward rate of bridge formation to the rate of relative diffusion between the microspheres

$$Da\big|_{h=h_{\min}} = \frac{k_f N_{eff}^2}{D / L_w^2}, \tag{5.1}$$

where k_f is a microscopic forward rate of hybridization, N_{eff} is the number of interacting DNA molecules in the gap between the particles, L_w is the width of the DNA-induced pair potential well, and D is the relative diffusivity. In reality, this Damköhler number is necessarily separation-dependent (the forward rate of bridge formation is zero when h is very large and grows monotonically as the particles approach one another), so we define our Da at a particular separation $h = h_{min}$, or the separation at the pair potential minimum. When the Damköhler number is large, the rate of bridge formation overwhelms the rate at which the particles can diffuse relative to one another, and bridging duplexes can form and break multiple times before the particles eventually move apart. On the other hand, when the Damköhler number is small, relative diffusion is much faster than bridge formation and the particles can collide multiple times without ever forming a single bridge. Within this context, we develop a method of extracting the Damköhler number Da from our dynamic trajectories by closely examining how likely the spheres are to bind together, as opposed to bouncing off of one another, when they 'collide'.

If, when two particles collide, we assume that they can take only one of two paths (either bind together or bounce apart), and those two processes are governed by the rates shown in Eq. 5.1, then we can define the probability that they will bounce off of one another as

$$P_{bounce} = \frac{D / L_w^2}{D / L_w^2 + k_f N_{eff}^2}. \tag{5.2}$$

In practice, to calculate P_{bounce} from our annotated trajectories, we determine all collision events (Figure 5.1), where the particles approach one another and cross a collision threshold $h_c = h_{min}$. For each collision event, we query our state trajectory to determine whether the particles bounced off of one another or stuck together before moving back across $h_c + 5$ nm (some hysteresis is built in to remove correlations). The ratio of the number of 'bounce events' to the number of collisions is then P_{bounce}, which can be related to the Damköhler by

$$Da = \frac{1}{P_{bounce}} - 1. \tag{5.3}$$

By construction, when the particles are equally likely to either stick or bounce ($P_{bounce}=P_{stick}=0.5$), the Damköhler number is one.

5.3 DNA-Induced Binding Dynamics

Using the concepts developed above, we parameterize our four sets of experiments by determining their experimental Da (Figure 5.4). Because the forward rate of bridge formation goes as the DNA labeling density squared, we find that we can vary the experimentally determined Da over nearly two orders of magnitude by diluting the DNA surface coverage by roughly an order of magnitude (Figure 5.4). Our inability to vary Da over two full orders of magnitude is likely due to the weak temperature dependence of the microscopic forward rate k_f and the relative diffusivity D. Regardless, we are able to explore the full transition from diffusion-limited binding ($Da > 1$) to reaction-limited binding ($Da < 1$).

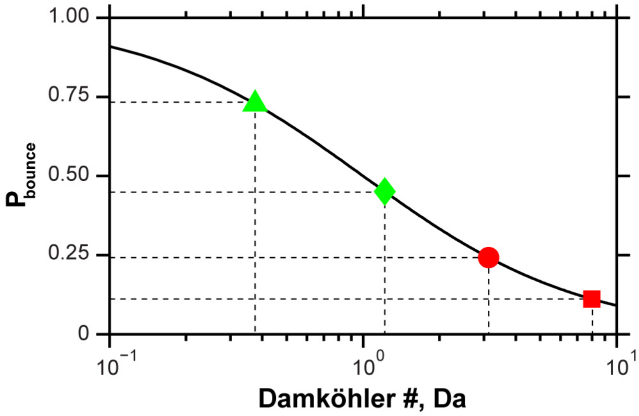

Figure 5.4. Experimentally determined Damköhler number *Da* extracted from the bouncing probability. The Damköhler number is varied by nearly two orders of magnitude by changing the DNA labeling density: 500 (▲), 700 (◆), 2500 (●) and 5000 (■) DNA/particle. To keep the interaction strength between 0-6 k_BT at temperatures within our experimentally accessible window, we used two different 'sticky end' sequences: 5'-GTCTACC-3' (red) and 5'-GTCTACCG-3' (green).

5.3.1 Diffusion-Limited Binding (*Da* > 1)

When the DNA labeling density is high (*Da* > 1), the forward rate of bridge formation is also high and we expect to see diffusion-limited binding between the particles. Figure 5.5 shows bound and unbound lifetime distributions for the highest *Da* system (*Da* ≈ 10). We find that both the bound and unbound lifetime distributions are accurately described by single exponentials. As expected, the mean lifetime of the unbound state is invariant with temperature and well depth, as it is determined entirely by the particles' relative diffusivity and the trapping potential (neither of which are strongly temperature sensitive). The mean bound lifetime, on the other hand, is an exponential function of the well depth and obeys an Arrhenius-type expression of the form

$$\langle t_b \rangle = \frac{1}{\omega} e^{-\frac{EB}{k_B T}}, \tag{5.4}$$

where EB is the binding energy and ω is the escape attempt frequency. Fitting equation 5.4 to our data yields an ω of ~100 s^{-1}, consistent with the reciprocal of the time required for the particles to diffuse the half-width of the potential well ($L_w \approx 15$ nm) (15).

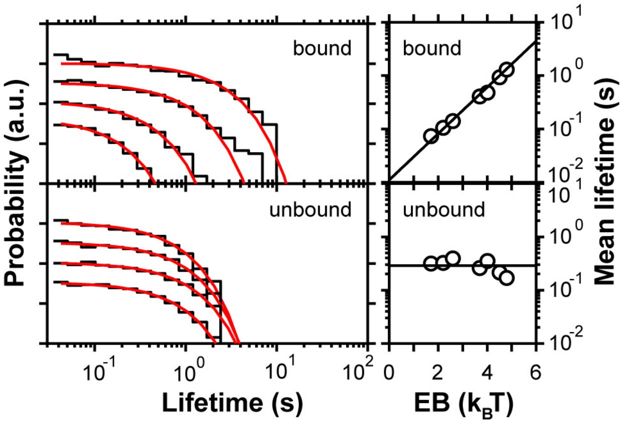

Figure 5.5. Densely-labeled DNA-functionalized colloids exhibit diffusion-limited binding. The bound and unbound lifetime distributions (black) are well fit by single exponentials (red) for all temperatures and well depths studied. The mean bound lifetime scales exponentially with the binding energy (EB) according to an Arrhenius-type expression. The mean unbound lifetime is invariant with the binding energy, and is determined solely by the trap shape and the particles' relative diffusivity. The escape attempt frequency is ~100 s^{-1} and is consistent with the inverse of the time to diffuse the half-width of the potential well ($L_w \approx 15$ nm).

That the bound lifetimes are exponentially distributed and their means obey an Arrhenius relationship to the well depths with an escape attempt frequency consistent with measurements of the relative particle diffusivity suggests that the binding is indeed diffusion-limited. To our knowledge, this is the first time that diffusion-limited binding has been observed in DNA-induced colloidal interactions, and dispels the notion that there is something intrinsically ‘strange’ or ‘slow’ about hybridization-mediated binding. Instead, it supports the claim that Watson-Crick base-pairing is suitable to direct the assembly of particles, and suggests that these interactions are amenable to conventional simulation of structure nucleation and growth (9, 10).

5.3.2 Reaction-Limited Binding ($Da < 1$)

In the other limit, when the rate of bridge formation is much slower than particle diffusion, we find highly non-exponential lifetime distributions (Figure 5.6), with functional forms that are consistent with previous studies of linker-mediated bridging (1). Again, a single exponential accurately fits the unbound lifetime distributions and their mean lifetime is invariant with the binding energy, as before. Unlike the high *Da* experimental system, the mean unbound time is now nearly four fold larger (~1s instead of ~0.25s), consistent with the claim that, when reaction-limited, the particles must collide several times before finally forming a DNA bridge. In fact, we can use this observation as a numerical check of our *Da* approximation, as the mean unbound lifetime should scale as $\sim 1/P_{stick}$, where P_{stick} is $1 - P_{bounce}$, i.e. $(1 - 0.1)/(1 - 0.75) \approx 4$.

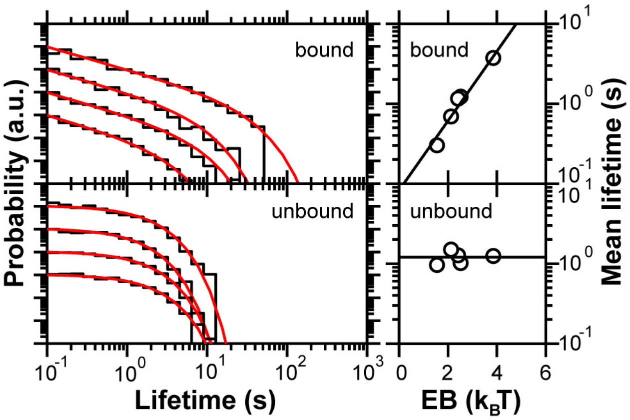

Figure 5.6. Sparsely-labeled DNA-functionalized colloids exhibit reaction-limited binding. The bound lifetime distributions (black) are fitted-well by truncated power laws (red) with a power law exponent of -1 for all temperatures and well depths. The mean bound lifetime scales exponentially with the binding energy (EB), but the escape attempt frequency (~10 s^{-1}) is much smaller than one over the diffusive rattle time (~100 s^{-1}). The unbound lifetime distributions (black) are fitted-well by single exponentials (red) and the mean lifetime is invariant with the binding energy.

The bound lifetime distributions are fitted-well by truncated power laws of the form

$$P(t_b) \propto t^{-\alpha} e^{-t_b/\tau_b}, \tag{5.5}$$

where α is the power law exponent and τ_b is a characteristic time. All bound lifetime distributions in Figure 5.6 can be fitted with a single power law exponent α=1, which is in the same range of exponents reported in other experimental (1) and theoretical (19) studies of DNA-mediated binding. Interestingly, if we fit the bound lifetime distributions from all four of our different *Da* systems, we find that the power law exponent α monotonically decreases with increasing *Da*, and approaches zero as *Da* becomes much greater than one (when α=0, the bound lifetime distribution is purely exponential). To investigate the origin of these non-exponential kinetics, we develop a simple dynamic model of multivalent binding.

5.4 Multivalent Binding Dynamics Model

Conceptually, one can imagine a number of mechanisms that could potentially give rise to the observed non-exponential binding kinetics. In this section, we investigate the relative contributions of four candidates: (i) it is generally accepted that even simple multivalent systems tend to display non-exponential lifetime distributions, a result of 'precursor' events where one or two bonds form and then rapidly dissociate; (ii) as recently demonstrated (12), local DNA density fluctuations (and resulting dispersion in the forward rate of bond formation) can also cause non-exponential binding and subdiffusive behavior; (iii) in addition to contributions from density fluctuations, there is necessarily a local distribution of forward rates due to the geometry of the two-particle interaction (i.e. DNA strands near the line of centers see a higher local concentration of their complement); and (iv) it has also been demonstrated experimentally that even single DNA molecules exhibit non-exponentially distributed bound lifetimes as a result of static disorder in their dehybridization/melting rate k_r (20, 21). To simulate the dynamics of multivalent binding in these different scenarios, we built a toy model consisting of N_{eff} discrete ligand-receptor pairs, i.e. N_{eff} reversible bonds in parallel.

In the simplest case (i), all ligand-receptor pairs are identical and the system is fully characterized by N_{eff} and a single binding Gibbs free energy $\Delta G_{bind} = -k_B T \ln(k_f / k_r)$, where k_f and k_r are the microscopic rates of bond formation and rupture, respectively. In the next simplest case (ii), the number of discrete bond pairs can fluctuate, but their molecular rates k_f and k_r remain unchanged. To include forward rate fluctuations that result from the system geometry (iii), we generate a realistic forward rate distribution $P(k_f)$ from our molar reactant fields $C_A^0(\vec{r}), C_B^0(\vec{r})$. Specifically, we construct $P(k_f)$ by sampling one of the reactant concentration fields with the equilibrium configurations of the strands on the opposing sphere, where k_f is proportional to $C_i^0(\vec{r})$. Finally, we include static disorder in the individual bond pairs (iv) by assigning each one a different k_r from the distribution

$$P(k_r) = \int_0^\infty dx \frac{1}{\pi} \exp\left[-k_r x - \left(\frac{x}{\tau_i}\right)^\beta \cos(\beta\pi)\right] \sin\left[\left(\frac{x}{\tau_i}\right)^\beta \sin(\beta\pi)\right], \qquad (5.6)$$

where β is the stretching exponent and τ_i is the characteristic time of an individual bond pair (20). The lifetime distributions associated with Eq. 5.6 are stretched exponential $P(t_b^i) \propto \exp[-(t_b^i / \tau_i)^\beta]$ and are often seen in single molecule experiments of DNA hairpin melting.

In the full model containing (i-iv), we launch the system with $\langle N_{eff} \rangle$ unbound, parallel ligand-receptor pairs, each with a forward rate k_f sampled from $P(k_f)$. We evolve the system with a fixed time step $\Delta t << 1/\max(k)$ that is much shorter than one over the largest rate in the system. Until the first bond is formed, we continually sample N_{eff} and k_f to approximate the tumbling of the two particles in the optical trap. Once a bond is formed, it is assigned a reverse rate k_r from $P(k_r)$ and maintains that specific k_r until it eventually dissociates. When the system has formed two or more bonds, we fix N_{eff} and

k_f to approximate the limited range of motion of the two tethered surfaces. Finally, we evolve the system until we have generated ~2000 binding/unbinding events. Figure 5.7 shows the simulated bound lifetime distributions from four different runs with $\langle N_{eff} \rangle = 15$ and $\Delta F_a = \ln P_0 = -2\ k_BT$.

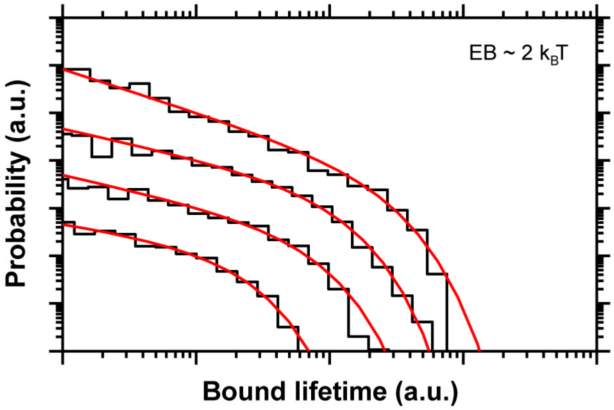

Figure 5.7. Simulated bound lifetime distributions. Simple dynamic models of varying complexity give rise to truncated power law bound lifetime distributions with power law exponents: (i) $\alpha = 0.4$ (bottom), (i-ii) $\alpha = 0.6$ (second from bottom), (i-iii) $\alpha = 0.6$ (second from top), and (i-iv) $\alpha = 0.95$ (top). Including static disorder in the microscopic reverse rate k_r with $\beta = 0.5$, a value consistent with literature reports (20-22), leads to highly non-exponential lifetime distributions comparable with our measurements. In each evaluation, ΔF_a was forced to -2 k_BT by adjusting the mean rates. As a result, the magnitude of the mean bound lifetime is unconstrained. This demonstration could be made more compelling by constraining the microscopic rates through experimental measurement.

All simulated bound lifetime distributions in Figure 5.7 are fitted-well by truncated power laws. We find that the bound lifetime distribution of the base case (i) is described by a truncated power law with an exponent α of only ~0.4. Including dispersion in the forward rate of bridge formation due to density fluctuations (i-ii) or density fluctuations and non-uniform microscopic rates k_f (i-iii) drives the power law exponent up to ~0.6, but never to the experimentally observed $\alpha \approx 1$. Not until we include dispersion in the rate of bond rupture k_r (i-iv) do we generate distributions with power law exponents approaching one. Remarkably, by including a rupture rate distribution with $\beta = 0.5$, a value consistent with experimental observation, we are able to generate simulated bound lifetime distributions with $\alpha = 0.95$. While these results and simulations are only preliminary, it is certainly suggestive that non-exponential kinetics at the single-molecule level may lead to even more non-exponential lifetime distributions in the multivalent limit.

5.5 Thermodynamics of Binding in the Low Density Limit

In addition to looking at the dynamics of binding, this large data set provides an excellent opportunity to thoroughly test our thermodynamic model (4) described in detail in Chapter 4. As before, we extract pair-interaction potentials for each pair of particle populations as a function of temperature. We find that the shape and spatial dependence of the pair potential is more or less unchanged (although the pair potentials seem to become increasingly blurred as *Da* decreases) when going to lower density, so they are omitted for clarity. Instead, we focus only on at the temperature dependence of the pair-interaction well depth or binding energy (Figure 5.8). The qualitative trends are consistent with our expectations; namely, the binding energy curves shift to lower temperatures as the DNA labeling density is decreased (for a given sticky end sequence). We also find that lengthening the sticky end sequence, and thereby increasing the hybridization Gibbs free energy, shifts the binding energy curves to higher temperatures, as expected.

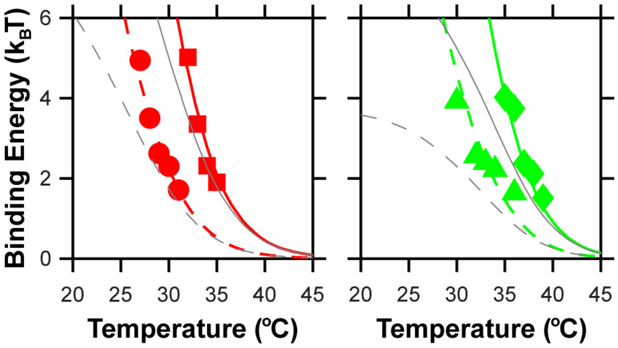

Figure 5.8. Temperature-dependent, DNA-induced interaction strength or binding energy. The points are experimental measurements, each averaged over five pairs, of the binding energy between DNA-functionalized colloids with varying labeling density: 500 (▲), 700 (◆), 2500 (●) and 5000 (■) DNA/particle. To keep the binding energies between 0-6 k_BT at temperature within our experimentally accessible window, we use two different 'sticky end' sequences: 5'-GTCTACC-3' (red) and 5'-GTCTACCG-3' (green). The interaction strength is computed assuming that the number of DNA bridges obeys binomial (colored) or Poisson (grey) statistics. We find that the Poisson approximation is invalid when the binding energy is greater than ~1 k_BT.

The continuum thermodynamic model presented in Chapter 4, which assumes that the bridge formation is accurately described as a Poisson process, captures the temperature dependence of the pair-interaction strength for the most densely labeled particles. Unfortunately, it fails to predict the temperature-dependent binding energy of the three lower density samples for attractive wells deeper than ~1 k_BT. In hindsight this is not particularly surprising, as we are necessarily driving bridge formation away from the conditions were the Poisson approximation is valid (N_{eff} is large and the probability p that a given molecule is bridged is small). In fact, in the lowest DNA density system, there are only ~15 DNA molecules per particle that are sterically available for bridge formation. In the limit where there is no longer a large reservoir of unreacted DNA molecules, bridge formation is no longer a simple Poisson process (effectively an 'open' system) and it appears that we must use binomial statistics to capture the depletion of available strands. The Poisson distribution approximates the binomial distribution only when N_{eff} is large and p is small.

As was the case in Chapter 4, evaluating the attractive contribution to the DNA-mediated pair-interaction essentially requires computing the probability that the particles are untethered P_0, and then evaluating

$$\frac{\Delta F_a}{k_B T} = \ln P_0 , \tag{5.6}$$

where P_0 is a function of temperature T and the relative separation h. To compute P_0 in the non-Poisson limit, we follow nearly the same approach presented in Chapter 4. Again, we model the DNA brushes as continuous fields of molar concentrations $C_A^0(\vec{r}), C_B^0(\vec{r})$ that are generated by oversampling static, equilibrium configurations of tethered freely-jointed chains. We compute the three-dimensional product field $C_{AB}(\vec{r})$ by solving the coupled equations

$$\begin{cases} C_{AB}(\vec{r}) = \dfrac{C_A(\vec{r})C_B(\vec{r})}{C_0} \exp\left[-\dfrac{\Delta G_{hyb}}{k_B T}\right] \\ C_A^0(\vec{r}) = C_A(\vec{r}) + C_{AB}(\vec{r}) \\ C_B^0(\vec{r}) = C_B(\vec{r}) + C_{AB}(\vec{r}) \end{cases} \tag{5.7}$$

as a function relative separation h and temperature T, and then evaluate ΔF_a according to

$$\frac{\Delta F_a}{k_B T} = \ln P_0 = N_{Av} \int C^0(\vec{r}) \ln\left[1 - \frac{C_{AB}(\vec{r})}{C^0(\vec{r})}\right] d^3\vec{r}\,, \tag{5.8}$$

where C^0 is the local minimum concentration of reactant 'A' or 'B'. In other words, we calculate the probability that the particles are unbound P_0, by evaluating the joint probability that there are no bridges at any point $\vec{r}$.

Solving Eqs. 4.6 and 5.8, blurred by our instrumental spatial resolution, we compute and fit the experimentally measured pair-interaction potentials, taking ΔG_{hyb} as a fitting parameter while allowing particle diameter to fluctuate slightly about its mean value to account for particle polydispersity. The best-fit model predictions are shown in Figure 5.8 and capture the full temperature dependence of the experimentally measured binding energies. Moreover, when we compare the fitted hybridization Gibbs free energies to *a priori* predictions of ΔG_{hyb} for our sticky ends (5'-GTCTACC-3' or 5'-GTCTACCG-3') from the nearest-neighbor model (23), we find average deviations of only 0.17 kcal/mol and -0.45 kcal/mol, respectively, both within the uncertainty of the NN model predictions, estimated to have a standard deviation of ~0.5 kcal/mol (23, 24). For the same fitted hybridization Gibbs free energies, evaluation of the model using the Poisson approximation (Figure 5.8) is unable to capture either the magnitude or the temperature dependence of the binding energy for any of the three lowest DNA density samples for binding energies greater than ~1 $k_B T$. While it seems unlikely that the addition of a single guanine nucleotide would lead to an absolute deviation of ~0.6 kcal/mol between our best-fit ΔG_{hyb} and the NN prediction, this subtle change could conceivably alter the π-stacking interactions or 'dangling end' stabilization. In practice, direct experimental determination of the hybridization free energies by UV-VIS spectrophotometry is probably required for a more definitive assessment.

5.6 Conclusion

In this chapter, we have shown that carefully designed systems of DNA-functionalized colloids exhibit diffusion-limited binding, suggesting that DNA-mediated interactions are suitable for the directed-assembly of particle-based systems. As the DNA labeling density is ‘titrated’ down, the hybridization-mediated binding becomes reaction-limited and the bound state lifetime distributions are highly non-exponential. We develop a simple dynamic model that is able to reproduce some of the anomalous kinetics observed in multivalent binding, provided the individual molecular degrees of freedom are themselves non-exponential. In addition to providing some insight into the dynamics of multivalent processes, these results also suggest helpful design criteria for experiments that look at binding between colloidal probes to access single-molecule lifetimes (13). Specifically, we find that the rate of bond formation must be significantly less than the particles’ diffusive rate (see Chapter 7 for details), so that individual binding events are not obscured by slow microsphere diffusion.

We also use this extensive data set to develop an extension to our mean-field thermodynamic model presented in Chapter 4. We find that the bridge formation can no longer be approximated as a Poisson process when evaluating the DNA-induced interactions between sparsely labeled particles. Instead, we use binomial statistics, generalized for the case of non-uniformly distributed reactants, to calculate the joint probability that the particles are untethered. This approach, which does not require any additional computation, is able to capture both the spatial and temperature dependence of DNA-induced pair-interactions between micron-scale particles with only a few hundred tethered strands. In the future, this should allow us to accurately predict DNA-induced interactions between nanometer-scale colloids, where the number of interacting DNA strands is necessarily small. While we have relied on a numerical approach, we note that our general framework is also amenable to analytic evaluation of the interaction free energy.

5.7 References

1. Biancaniello PL, Kim AJ, Crocker JC (2005) Colloidal interactions and self-assembly using DNA hybridization. *Physical Review Letters* 94:058302.
2. Dreyfus R*, et al.* (2009) Simple Quantitative Model for the Reversible Association of DNA Coated Colloids. *Physical Review Letters* 102:048301.
3. Leunissen ME, Frenkel D (2011) Numerical study of DNA-functionalized microparticles and nanoparticles: Explicit pair potentials and their implications for phase behavior. *Journal of Chemical Physics* 134:084702.
4. Rogers WB, Crocker JC (2011) Direct measurements of DNA-mediated colloidal interactions and their quantitative modeling. *Proceedings of the National Academy of Sciences of the United States of America* 108:15687-15692.
5. Kim AJ, Scarlett R, Biancaniello PL, Sinno T, Crocker JC (2009) Probing interfacial equilibration in microsphere crystals formed by DNA-directed assembly. *Nature Materials* 8:52-55.
6. Nykypanchuk D, Maye MM, van der Lelie D, Gang O (2007) DNA-based approach for interparticle interaction control. *Langmuir* 23:6305-6314.
7. Licata NA, Tkachenko AV (2006) Errorproof programmable self-assembly of DNA-nanoparticle clusters. *Physical Review E* 74:041406.
8. Lukatsky DB, Mulder BM, Frenkel D (2006) Designing ordered DNA-linked nanoparticle assemblies. *Journal of Physics-Condensed Matter* 18:S567-S580.
9. Scarlett RT, Crocker JC, Sinno T (2010) Computational analysis of binary segregation during colloidal crystallization with DNA-mediated interactions. *Journal of Chemical Physics* 132.
10. Scarlett RT, Ung MT, Crocker JC, Sinno T (2011) A mechanistic view of binary colloidal superlattice formation using DNA-directed interactions. *Soft Matter* 7:1912-1925.
11. Kim AJ, Biancaniello PL, Crocker JC (2006) Engineering DNA-mediated colloidal crystallization. *Langmuir* 22:1991-2001.
12. Xu Q, Feng L, Sha R, Seeman NC, Chaikin PM (2011) Subdiffusion of a Sticky Particle on a Surface. *Physical Review Letters* 106.
13. Biancaniello PL, Kim AJ, Crocker JC (2008) Long-time stretched exponential kinetics in single DNA duplex dissociation. *Biophysical Journal* 94:891-896.
14. Crocker JC, Grier DG (1996) Methods of digital video microscopy for colloidal studies. *Journal of Colloid and Interface Science* 179:298-310.
15. Biancaniello PL, Crocker JC (2006) Line optical tweezers instrument for measuring nanoscale interactions and kinetics. *Review of Scientific Instruments* 77:113702.
16. Bronson JE, Fei JY, Hofman JM, Gonzalez RL, Wiggins CH (2009) Learning Rates and States from Biophysical Time Series: A Bayesian Approach to Model Selection and Single-Molecule FRET Data. *Biophysical Journal* 97:3196-3205.

17. Sorgenfrei S, *et al.* (2011) Label-free single-molecule detection of DNA-hybridization kinetics with a carbon nanotube field-effect transistor. *Nature Nanotechnology* 6:125-131.
18. Fei JY, *et al.* (2009) Allosteric collaboration between elongation factor G and the ribosomal L1 stalk directs tRNA movements during translation. *Proceedings of the National Academy of Sciences of the United States of America* 106:15702-15707.
19. Licata NA, Tkachenko AV (2007) Colloids with key-lock interactions: Nonexponential relaxation, aging, and anomalous diffusion. *Physical Review E* 76.
20. Ying LM, Wallace MI, Klenerman D (2001) Two-state model of conformational fluctuation in a DNA hairpin-loop. *Chemical Physics Letters* 334:145-150.
21. Ansari A, Kuznetsov SV, Shen YQ (2001) Configurational diffusion down a folding funnel describes the dynamics of DNA hairpins. *Proceedings of the National Academy of Sciences of the United States of America* 98:7771-7776.
22. Kim J, Doose S, Neuweiler H, Sauer M (2006) The initial step of DNA hairpin folding: a kinetic analysis using fluorescence correlation spectroscopy. *Nucleic Acids Research* 34:2516-2527.
23. SantaLucia J, Hicks D (2004) The thermodynamics of DNA structural motifs. *Annual Review of Biophysics and Biomolecular Structure* 33:415-440.
24. SantaLucia J, Turner DH (1997) Measuring the thermodynamics of RNA secondary structure formation. *Biopolymers* 44:309-319.

Chapter 6

Linker-Mediated Interactions and Binding Dynamics

6.1 Introduction

In general, during a DNA-directed particle self-assembly experiment, an experimenter would like to specify the binding strengths between a number of different particle species, in essence a symmetric matrix of binding strengths, that will necessarily be temperature-dependent. As demonstrated in Chapter 4, we can program these interactions by functionalizing particles with mixtures of directly complementary DNA strands and quantitatively model them in a mean-field way (1). Another promising approach to specifying the mutual interactions between particles that is, in principle, significantly more flexible, uses soluble 'linker' strands (2, 3) to facilitate inter-particle bridging (Figure 6.1). While this is a very common approach for addressing DNA-induced interactions between nanoparticles (4, 5), groups investigating DNA-mediated binding between micron-scale colloids (6-9) tend to shy away from linker-based systems, as there are concerns that linker-mediated binding is inherently slow (2, 3). Remarkably, unlike another well known, short-range colloidal interaction, the depletion attraction (10), which drives the crystallization of micron-sized polystyrene microspheres in minutes (3, 11), the only DNA linker-mediated colloidal crystals took days to nucleate and grow, despite the fact that their interactions were completely reversible (2, 3).

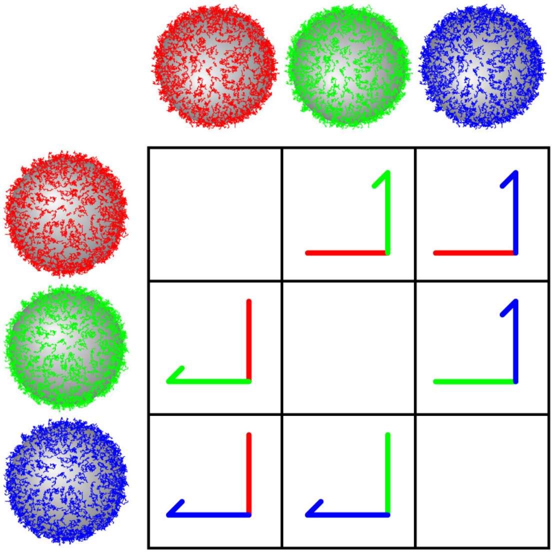

Figure 6.1. Schematic of a symmetric DNA-mediated pair-interaction matrix. A convenient way of specifying multiple orthogonal interactions between DNA-labeled particles is through carefully designed soluble linker strands. In this example, three particle types interact with one another through three linker strands. By design, any given particle can bind to a particle of another type, but cannot bind to another particle of its own type.

In this chapter, we measure linker-mediated binding between one-micrometer diameter polystyrene colloids and extend our linker-free, mean-field interaction model from Chapters 4 and 5. We also extract the DNA-induced binding dynamics and compare them with the linker-free measurements from Chapter 5, previously demonstrated to be nearly diffusion-limited. We suggest that the kinetics of linker-mediated binding in earlier reports were impaired by unstable intermediate species that are required for rapid bridging, thus relying on rare three-body (i.e. particle-linker-particle) interactions. To stabilize the intermediate species and speed up the dynamics, we suggest that linkers should be ‘thermodynamically’ asymmetric, i.e. the linker should bind more firmly to one particle species than the other. Finally, we show that the near-diffusion-limited binding observed in linker-free systems can be fully recovered through the use asymmetric linker strands, while still preserving the added design flexibility associated with linker-based architectures.

6.2 Linker-Induced Pair-Interactions

To explore linker-mediated binding between particles, we synthesize three different populations of DNA-functionalized colloids, A, B, and C, each with a single sequence labeled to its surface (Figure 6.2). As in Chapters 4 and 5, sequences ‘A’ and ‘B’ are complementary and can hybridize together to induced attractive interactions between A and B particles (Figure 6.2b). Sequence ‘C’ is neither complementary to sequence ‘A’ nor sequence ‘B,’ so binding must be mediated by soluble linker strands. A linker, ‘L1,’ which is partially complementary to ‘A’ and partially complementary to ‘C’ is used to mediate binding between two different particle species, A and C (Figure 6.2c). Another linker, ‘L2,’ is symmetric and can bridge between two C particles of the same type (Figure 6.2d). Each particle is nominally labeled with 3,000 DNA strands and stabilized against nonspecific binding by a dense PEO brush. The three particle-labeled sequences are: 5’-$(T)_{50}$-TAATGCCTGCTACC-3’, 5’-$(T)_{50}$-TGAGTTGCGGTAGAC-3’, and 5’-$(T)_{50}$-TGAGTTGGATAAGCG-3’ for sequences ‘A,’ ‘B,’ and ‘C,’ respectively. The two linker sequences are: 5’-CGCTTATCACGGTAGACAGG-3’ and 5’-CGCTTATCCTCGCTTATCC-3’ for ‘L1’ and ‘L2,’ respectively. The two linker-based studies were performed in aqueous buffer containing 250 nM linker/ 0.01% (v/v) colloids/ 10 mM tris-HCl/ 1 mM EDTA/ 100 mM NaCl/ pH=8.0.

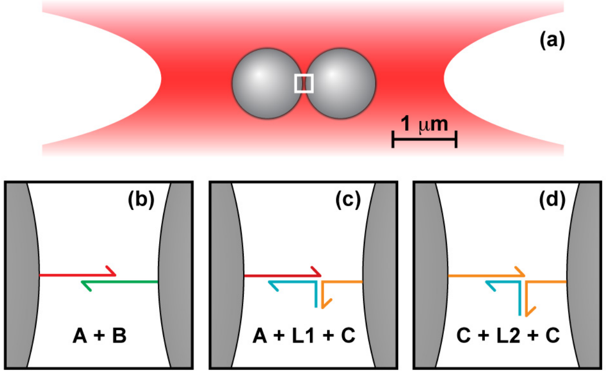

Figure 6.2. Different DNA-induced interaction schemes. Two one-micrometer diameter, DNA-functionalized particles confined to an extended optical potential, or line trap, (a) can be bridged together by DNA duplexes in a number of different ways. When the two particles display different but complementary sequences of DNA, they can bind together in a linker-free way (b). If the surface-tethered DNA sequences are not directly complementary, a soluble linker strand must mediate binding. That linker strand can either bridge between particles of different types (c), or it can be symmetric and induce binding between two particles of the same species (d).

As before, to extract DNA-induced, pair-interaction potentials, we confine two DNA-functionalized particles in an extended optical potential or line trap and passively track and histogram their relative separation h as they undergo Brownian motion (see Chapter 2). The equilibrium pair free energy $F(h)$, then, can be computed from the measured $P(h)$, up to an additive constant, by inverting the Boltzmann relation, $P(h) \propto \exp[-F(h)/k_B T]$, where $k_B T$ is the thermal energy (12). Using this approach, we measure DNA-induced pair-interaction potentials for our three different DNA architectures as a function of temperature T and relative separation h. A detailed discussion of the measurement and modeling of linker-free experiments is discussed in Chapters 4 and 5 and is omitted here. Figure 6.4a shows the experimentally measured temperature-dependent binding energy for our linker-free A-B interactions and corresponding model agreement.

6.2.1 Two-Component, Asymmetric Linker: A-L1-C

Figure 6.3 shows five representative pair potentials for the A-L1-C interaction as a function of temperature. As expected, all pair potentials show a temperature-dependent attraction whose strength increases monotonically with decreasing temperature as DNA bridges become more thermodynamically stable. Again, the attractive interaction disappears completely at higher temperatures, but under those conditions, it is impossible to discriminate between A-L1-A, C-L1-C and A-L1-C interactions. No binding was observed between pairs of A or C particles, or in the absence of linkers, demonstrating that binding is indeed the result of linker-mediated bridging.

To model the spatial and temperature dependence of the A-L1-C interaction, we follow a very similar approach to that described in Chapters 4 and 5, where the bridge formation reaction is now $A + L_1 + C \rightleftharpoons AL_1C$. Again, we treat the bridge formation process as chemical equilibration between spatially varying, static fields of molar concentrations. Specifically, two of the reactant fields $C_A^0(\vec{r}), C_C^0(\vec{r})$ are constructed, as before, by oversampling equilibrium configurations of freely-jointed chains uniformly tethered to spherical caps. The linker field $C_{L_1}^0(\vec{r})$ is spatially uniform and is 250 nM everywhere. Finally, we compute the 'product' field $C_{AL_1C}(\vec{r})$ by solving the system of equations

$$\begin{cases} C_{AL_1C}(\vec{r}) = \dfrac{C_A(\vec{r})C_{L_1}(\vec{r})C_C(\vec{r})}{C_0^2}\exp\left[\dfrac{-\Delta G_{hyb}^{AL_1} - \Delta G_{hyb}^{L_1C}}{k_B T}\right] \\ C_{AL_1}(\vec{r}) = \dfrac{C_A(\vec{r})C_{L_1}(\vec{r})}{C_0}\exp\left[\dfrac{-\Delta G_{hyb}^{AL_1}}{k_B T}\right] \\ C_{L_1C}(\vec{r}) = \dfrac{C_{L_1}(\vec{r})C_C(\vec{r})}{C_0}\exp\left[\dfrac{-\Delta G_{hyb}^{L_1C}}{k_B T}\right] \\ C_A^0(\vec{r}) = C_A(\vec{r}) + C_{AL_1}(\vec{r}) + C_{AL_1C}(\vec{r}) \\ C_C^0(\vec{r}) = C_C(\vec{r}) + C_{L_1C}(\vec{r}) + C_{AL_1C}(\vec{r}) \\ C_{L_1}^0(\vec{r}) \approx C_{L_1}(\vec{r}) \end{cases} , \qquad (6.1)$$

where $C_0 = 1M$ is a reference concentration, $C_i(\vec{r})$ is the equilibrium concentration of species i, and ΔG_{hyb}^i is the hybridization Gibbs free energy for the formation of the intermediate species i. The last three formulae describe mole balances with initial concentrations $C_A^0(\vec{r})$, $C_C^0(\vec{r})$, and $C_{L_1}^0(\vec{r})$, which are taken as static, i.e. they do not vary with the extent of reaction. Because the colloid volume fraction in our experiment is only 0.01% (v/v), the linker strands are in significant excess of the tethered DNA strands and are treated as an infinite reservoir, with $C_{L_1}^0(\vec{r}) \approx C_{L_1}(\vec{r})$. Finally, we calculate the attractive free energy ΔF_a by evaluating

$$\frac{\Delta F_a}{k_B T} = \ln P_0 = N_{Av}\int C^0(\vec{r})\ln\left[1 - \frac{C_{AL_1C}(\vec{r})}{C^0(\vec{r})}\right]d\vec{r}^{\,3}, \qquad (6.2)$$

where N_{Av} is Avogadro's number, P_0 is the probability that the particles are unbound, and $C^0(\vec{r})$ is the minimum local brush concentration $C^0(\vec{r}) = \min[C_A^0(\vec{r}), C_C^0(\vec{r})]$.

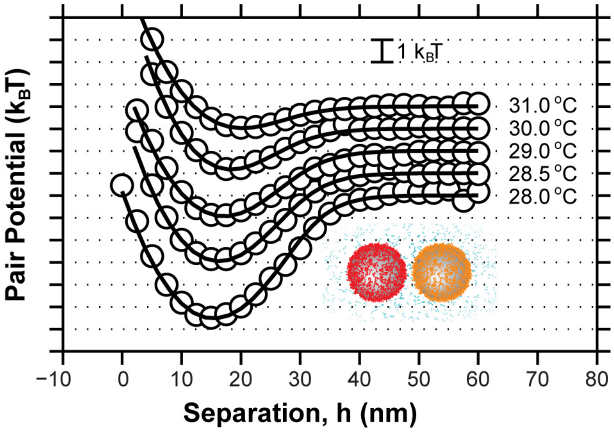

Figure 6.3. Representative pair potentials that result from linker-mediated binding. An asymmetric soluble linker strand induces binding between two different particle species (A-L1-C) in a temperature-dependent way. The DNA-mediated interaction can be tuned from very weak to effectively irreversible over only ~3 °C. The circles are experimental data and the solid curves are model-fits. The pair-interaction potentials show a temperature-dependent attraction that results from dynamically forming and breaking DNA bridges, and a temperature-independent, short-range repulsion that arises from the compression of unbridged strands. The data and model-fits are shifted vertically for clarity.

Solving Eqs. 4.6, 6.1, and 6.2, blurred by our instrumental spatial resolution of ~3.5 nm (see Chapter 2), we compute and fit the experimentally measured pair-interaction potentials in Figure 6.3, taking $\Delta G_{hyb}^{L_1C}$ as a fitting parameter, while allowing the particle diameter to fluctuate slightly about its mean value to account for particle polydispersity. The best-fit model predictions are overlaid on the measured pair potentials and capture the full spatial dependence of the linker-mediated pair-interactions at all temperatures. Moreover, we find that the model is able to accurately capture the steep temperature dependence of the binding energy up to interaction strengths of 6 k$_B$T (Figure 6.4b). Interestingly, when we compare the fitted hybridization Gibbs free energies to a priori predictions for $\Delta G_{hyb}^{L_1C}$ from the NN model (13, 14), we find a constant deviation of ~1.3 kcal/mol at all temperatures, outside the a priori uncertainty of the nearest-neighbor model, estimated to be about ±0.6 kcal/mol.

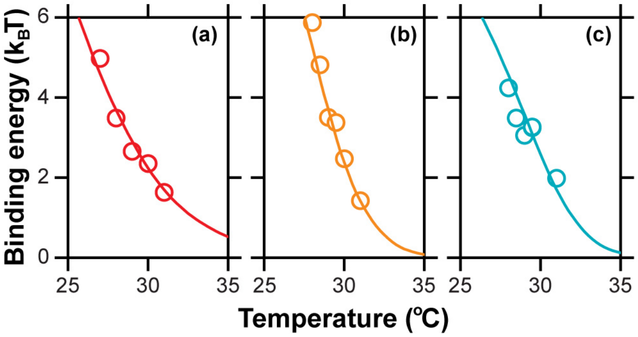

Figure 6.4. The temperature-dependent binding energy of three different DNA architectures. The binding energy between two particles functionalized with complementary sequences of DNA can be modeled quantitatively in a mean-field manner (a). Soluble linker strands can also be used to induce binding between DNA functionalized colloids in a temperature-dependent way. If the *a priori* hybridization Gibbs free energies are adjusted slightly, our mean-field model from Chapters 4 and 5 also captures the temperature dependence of binding mediated by an asymmetric (b) or symmetric (c) linker. The circles are experimental data averaged over five pairs. The solid curves are model-fits.

Unlike the linker-free interactions described in Chapters 4 and 5, which were fully specified by a single Gibbs free energy, there are now two hybridization free energies, one for each half reaction: $A + L_1 \rightleftharpoons AL_1$ and $L_1 + C \rightleftharpoons L_1C$. Rather than fitting for both ΔG_{hyb}^{i}, we take advantage of the dynamic content of our data to constrain the problem. Specifically, we find that the experimentally determined *Da* is > 1, indicating a rapid rate of bridge formation likely due to the thermodynamic stabilization of one of the intermediate species: AL_1 or L_1C. Because the ratio of the two equilibrium constants

$\exp(-\Delta G_{hyb}^{AL_1} + \Delta G_{hyb}^{L_1C}) \approx 100$ suggests that the $A + L_1 \rightleftharpoons AL_1$ half-reaction is strongly favored, we assume that the NN prediction of the hybridization Gibbs free energy $\Delta G_{hyb}^{AL_1}$ is accurate, as it predicts that the half-reaction $A + L_1 \rightleftharpoons AL_1$ is near completion. Moreover, because $A + L_1 \rightleftharpoons AL_1$ results in the formation of a conventional, in-line duplex (Figure 6.2c), the double-stranded motif most common in development of the NN model, it seems logical that those predictions would be most accurate. As a result, we 'lump' all of the deviations from the *a priori* prediction into $\Delta G_{hyb}^{L_1C}$, and propose two potential explanations for the destabilization of that second bridge-half.

We hypothesize that the thermodynamic stability of the linker-mediated bridges is compromised by two factors related to the 'geometry' of the final bridge; specifically, the (i) increased force-sensitivity and (ii) additional entropic or enthalpic penalties associated with bending the duplex into an 'L-like' shape (Figure 6.2c). As detailed in Chapter 4, we estimate that each bridge experiences an average tension of ~0.4 pN. Because the reactive compliance of the perpendicular duplex is larger than the in-line duplex (i.e. it is more easily unzipped as a result of force), we find that this force results in a free energy change of ~0.4 kcal/mol (15), leaving ~0.9 kcal/mol accounted for. We suggest that the remaining 0.9 kcal/mol may come from penalties associated with bending the duplex. Unfortunately, while we designed the linker to have an unpaired 'hinging' base to minimize this effect, it may be that a single nucleotide is insufficient. In hindsight, this is not particularly surprising as the persistence length of ssDNA is roughly four nucleotides long. In the future, it would be interesting to repeat these experiments with linkers that have different 'hinge' lengths to see if we could improve the model agreement. Another approach may be to design linker architectures that result in all in-line duplexes (Figure 6.5), i.e. pairs of linkers instead of a single linker strand (5).

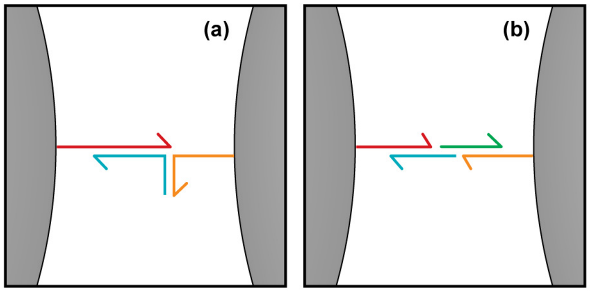

Figure 6.5. Two different linker-mediated binding schemes. The use of only a single linker strand (a) results in the formation of highly bent ‘L-like’ duplexes whose thermodynamics do not obey a simple nearest-neighbor model. Complementary linker pairs (b) lead to the formation of linear bridges that may be less force-sensitive and easier to model.

6.2.2 One-Component, Symmetric Linker: C-L2-C

To compare our asymmetric linker design with the earlier experimental system that demonstrated slow, reaction-limited binding (2, 3), we measure the pair-interaction potentials between two particles of the same type mediated by a symmetric linker (Figure 6.2c). As with the mixed interactions discussed in Chapter 4, the symmetry of the system requires that we consider self-interactions and loop states, but for the bridge formation reaction $C + L_2 + C \rightleftharpoons CL_2C$. Again, we calculate the ‘product’ concentration field by solving the coupled equations

$$
\begin{aligned}
&C_{CL_2C}(\bar{r}) = \frac{C_C(\bar{r})^2 C_{L_2}(\bar{r})}{C_0^2}\exp\left[\frac{-\Delta G_{hyb}^{CL_2} - \Delta G_{hyb}^{L_2C}}{k_B T}\right] \\
&C_{CL_2}(\bar{r}) = \frac{C_C(\bar{r}) C_{L_2}(\bar{r})}{C_0}\exp\left[\frac{-\Delta G_{hyb}^{CL_2}}{k_B T}\right] \qquad , \\
&C_C^0(\bar{r}) = C_C(\bar{r}) + C_{CL_2}(\bar{r}) + 2C_{CL_2C}(\bar{r}) \\
&C_{L_2}^0(\bar{r}) \approx C_{L_2}(\bar{r})
\end{aligned}
\tag{6.3}
$$

where $C_0 = 1M$ is the reference concentration, $C_i(\bar{r})$ is the equilibrium concentration of species *i*, and ΔG_{hyb}^i is the hybridization Gibbs free energy for the formation of the intermediate species *i*. As before, we assume that hybridization results in an unbiased distribution of loops and bridges that is governed only by the local stoichiometry, and calculate the fraction of equilibrium duplexes that are bridges according to $f_{bridge}(\bar{r}) = 2C_C^{0,L}(\bar{r})C_C^{0,R}(\bar{r}) / (C_C^{0,L}(\bar{r}) + C_C^{0,R}(\bar{r}))^2$, where $C_C^{0,L}(\bar{r})$ and $C_C^{0,R}(\bar{r})$ are the contributions to the reactant field $C_C^0(\bar{r})$ from the left and right particle, respectively. Finally, the linker-induced attractive free energy is found by evaluating

$$
\frac{\Delta F_a}{k_B T} = \ln P_0 = N_{Av}\int C^0(\bar{r})\ln\left[1 - \frac{f_{bridge}(r)C_{CL_2C}(\bar{r})}{C^0(\bar{r})}\right]d\bar{r}^3 , \tag{6.4}
$$

where $C^0(\bar{r}) = \min[C_C^{0,L}(\bar{r})(1 - f_{loop}^L(\bar{r})), C_C^{0,R}(\bar{r})(1 - f_{loop}^R(\bar{r}))]$ and $f_{loop}^i(\bar{r})$ is the fraction of duplexes on particle *i* that are loops. We fit our experimentally measured pair potentials to numerically blurred solutions of Eqs. 4.6, 6.3, and 6.4, taking $\Delta G_{hyb}^{L_2C}$ as a free parameter. To be consistent with our approach detailed above, we only allow the hybridization Gibbs free energy of one half-reaction to vary, and fix the hybridization free energy of the other.

Unfortunately, we find that the temperature-dependent interaction strength of the symmetric linker system (Figure 6.4c) is not accurately described by our extended model, as the fitted hybridization Gibbs free energy differs from the NN prediction by about -2.2 kcal/mol, well outside the a priori uncertainty of ±0.7 kcal/mol. Because this is probably our most complex DNA architecture studied, perhaps it is not all that surprising that our model predictions are a few degrees off from the measured binding energies. Either way, we suggest a few explanations for this disagreement and highlight another potential issue associated with our thermodynamic modeling framework. First, there are likely to be complications that result from the high degree of symmetry in the system. Specifically, if the first reaction in the bridge formation process $C + L_2 \rightleftharpoons CL_2$, i.e. free linkers hybridizing to tethered strands, is significantly favored over the second $CL_2 + C \rightleftharpoons CL_2C$ (for the reasons described above), the particles could become 'passivated' against binding. On the other hand, if the first half-reaction is thermodynamically unstable and there are few hybridized linkers, our assumption that the two-particle system is in chemical equilibrium may not be satisfied. In this limit, we would need to consider the finite dynamics of linker and particle diffusion to accurately estimate the binding energy in this system. Finally, because we conduct the pair-interaction measurements at particle volume fractions of only ~0.01% (v/v) and the linker strands are in ~100-1000 fold excess compared to the tethered sequences, we are potentially sensitive to the presence of impurity strands at the 0.1-1% level that interfere with bridging. In the future, repeating these pair-interaction experiments as a function of linker concentration should help shed light on the possible mechanism. In addition, these linker-based systems lend themselves to complementary measurement by aggregation-disaggregation type experiments that are conducted at more relevant volume fractions, e.g. 1-10% (v/v) colloids.

6.3 Linker-Induced Binding Dynamics

In addition to looking at the equilibrium pair-interactions and extending our continuum thermodynamics model, we also look at the linker-mediated binding dynamics and compare them to a linker-free system with nearly the same DNA density. Rather the considering the full lifetime distributions and Damköhler analysis presented in Chapter 5, we only look at the well depth-dependent mean bound lifetime. Figure 6.6a shows the mean bound lifetimes as a function of the interaction strength for all three DNA architectures. We find that all mean bound lifetimes scale exponentially with the binding energy and can be fitted by an Arrhenius-type equation to extract an escape attempt frequency ω, as described in Chapter 5 (Figure 6.6b). As hypothesized, we see that switching from a symmetric to an asymmetric linker increases the unbinding attempt frequency by roughly five fold. Moreover, we find that the asymmetric linker system is able to fully recover the diffusion-limited binding exhibited by linker-free architectures. Although this work is only preliminary, it suggests we should be able to design DNA-induced interaction matrices that have the rapid binding of linker-free systems, while maintaining the design flexibility afforded by linker-mediated bridging. These studies would again be nicely complemented by dynamic aggregation-disaggregation type experiments at more assembly-relevant volume fractions, i.e. 10% (v/v) particles.

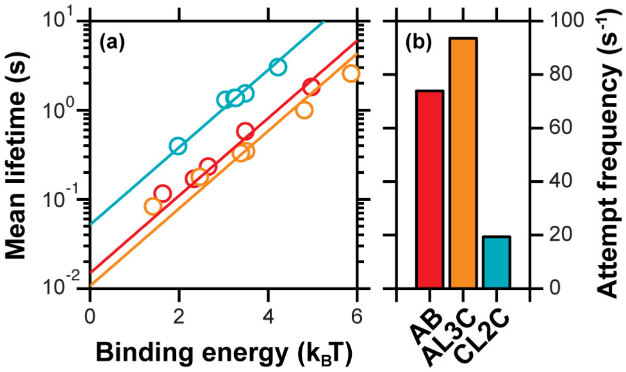

Figure 6.6. The dynamics of linker-mediated binding. The DNA-induced binding between three different DNA architectures scales exponentially with the interaction strength of binding energy (a): linker-free binding between two different particle types (red), asymmetric linker-mediated binding between two different particles types (orange), and symmetric linker-induced binding between two particles of the same species (blue). The escape attempt frequency can be determined for each architecture (b) and demonstrates that the unbinding rate can be increased nearly five fold by introducing a slight asymmetry in the thermodynamic stability of the linker's two half reactions.

6.4 Conclusion

In this chapter, we have investigated the DNA-induced interactions and dynamics of three different DNA architectures: (i) linker-free and (ii) asymmetric linker-mediated binding between different particle species, and (iii) symmetric linker-induced binding between two particles of the same type. We find that we can extend our continuum model from Chapters 4 and 5 to describe linker-induced binding between DNA-functionalized colloids, but suggest that refinement of the linker sequence will be necessary for more quantitative agreement (e.g. longer 'hinge' sequences or the use of linker pairs instead of single linker strands). We also demonstrate that, by making the linker slightly asymmetric, we are able to recover the binding dynamics of our linker-free system, while maintaining the design flexibility afforded by linker-based systems. In the future, we imagine that DNA-directed particles assemblies will by guided by both linker-free and linker-mediated interactions between a number of interacting particles, and quantitative models will be required to specify their mutual interactions.

6.5 References

1. Rogers WB, Crocker JC (2011) Direct measurements of DNA-mediated colloidal interactions and their quantitative modeling. *Proceedings of the National Academy of Sciences of the United States of America* 108:15687-15692.
2. Biancaniello PL, Kim AJ, Crocker JC (2005) Colloidal interactions and self-assembly using DNA hybridization. *Physical Review Letters* 94:058302.
3. Kim AJ, Biancaniello PL, Crocker JC (2006) Engineering DNA-mediated colloidal crystallization. *Langmuir* 22:1991-2001.
4. Park SY*, et al.* (2008) DNA-programmable nanoparticle crystallization. *Nature* 451:553-556.
5. Macfarlane RJ*, et al.* (2011) Nanoparticle Superlattice Engineering with DNA. *Science* 334:204-208.
6. Dreyfus R*, et al.* (2009) Simple Quantitative Model for the Reversible Association of DNA Coated Colloids. *Physical Review Letters* 102:048301.
7. Leunissen ME*, et al.* (2009) Switchable self-protected attractions in DNA-functionalized colloids. *Nature Materials* 8:590-595.
8. Leunissen ME*, et al.* (2009) Towards self-replicating materials of DNA-functionalized colloids. *Soft Matter* 5:2422-2430.
9. Ung MT, Scarlett R, Rogers WB, Sinno T, Crocker JC (2011) Diffusionless transformations and real-space crystallography of DNA-directed colloidal crystals. *Submitted*.
10. Asakura S, Oosawa F (1954) On Interaction between 2 Bodies Immersed in a Solution of Macromolecules. *Journal of Chemical Physics* 22:1255-1256.
11. Dinsmore AD, Yodh AG, Pine DJ (1995) Phase-Diagrams of Nearly Hard-Sphere Binary Colloids. *Physical Review E* 52:4045-4057.
12. Biancaniello PL, Crocker JC (2006) Line optical tweezers instrument for measuring nanoscale interactions and kinetics. *Review of Scientific Instruments* 77:113702.
13. SantaLucia J, Turner DH (1997) Measuring the thermodynamics of RNA secondary structure formation. *Biopolymers* 44:309-319.
14. SantaLucia J, Hicks D (2004) The thermodynamics of DNA structural motifs. *Annual Review of Biophysics and Biomolecular Structure* 33:415-440.
15. Woodside MT*, et al.* (2006) Nanomechanical measurements of the sequence-dependent folding landscapes of single nucleic acid hairpins. *Proceedings of the National Academy of Sciences of the United States of America* 103:6190-6195.

Chapter 7

Single Molecule Studies of DNA and Protein Unfolding

7.1 Introduction

Over the past decade, single molecule experiments have probed the unfolding and unbinding kinetics of DNA, RNA and proteins (1-6). While some experiments find exponential lifetime distributions, as expected for a single reaction pathway or rate-limiting step, other experiments find highly non-exponential lifetime distributions—with both findings sometimes reported for the same molecule (7-11). While non-exponential kinetics have often been attributed to multiple reaction pathways over a rough energy landscape, it is unclear how this mechanism would specifically yield the stretched exponential and log-normal distributions typically observed. Here we develop a simple model consisting of a single rate-limiting pathway having a free energy barrier modulated by a time varying force, possibly due in turn to thermal fluctuations in other portions of the same molecule or its measurement instrument. Remarkably, this model generates stretched exponential and log-normal lifetime distributions over a broad range of experimental and molecular parameters when the fluctuating force varies over timescales longer than the mean lifetime. While this model may shed some light on the current disagreement between different measurements of DNA duplex and hairpin opening kinetics, and non-exponential kinetics of ubiquitin unfolding under force, it appears that the experimental time scales on which these forces fluctuate is much too fast. For this mechanism to apply, then, we hypothesize that the bond may have some 'memory' of the force it experiences upon formation. For the specific case of DNA duplex melting, we offer an additional explanation relating to patchiness in the DNA labeling density.

7.2 Dynamical Heterogeneity in Single Molecule Experiments

The unfolding and unbinding of biomolecules have frequently been shown to be force sensitive. In the first and simplest model, due to Bell (12), the relevant activation barrier decreases by an amount which is proportional to the applied molecular tension F resulting in an exponential dependence in the transition rate constant k,

$$k(F) = \tau_{attempt}^{-1} e^{-\frac{E_a - F\Delta x}{k_B T}} = k_0 e^{\frac{F}{F_0}}, \tag{7.1}$$

where $\tau_{attempt}$ is the attempt time for barrier crossing, E_a is the activation free energy, Δx is the distance from the folded state to the transition state, k_BT is the thermal energy, k_0 is the unfolding rate coefficient at zero force and $F_0 = k_BT/\Delta x$. For a constant force, Eq. 7.1 predicts a single rate constant and an exponential distribution for the waiting times (lifetimes) of the corresponding Poisson process. Obviously, a distribution of forces, would lead to a distribution of rate constants and a non-exponential lifetime distribution. We hypothesize that force fluctuations due to ubiquitous thermal (Brownian) excitation could account for the non-exponential kinetics seen in many systems. Indeed, unlike many other purported mechanisms for explaining non-exponential behavior, force fluctuations must be present, and have a readily computable amplitude. We determine first the magnitude and form of the force distribution required, and second how slow the force fluctuations must be for Eq. 7.1 to apply, i.e. to be quasi-static.

To answer the first question, we computed the expected lifetime distribution of a Bell bond subjected to a Gaussian distribution of static forces (13) with mean force $\bar{F}$ and standard deviation σ_F, parameterizing the results as a function of $\sigma = \sigma_F / F_0$ and $\mu = \bar{F} / F_0$. As analytic results are not available, lifetime distributions $P(\tau)$ were computed directly by Monte Carlo; typical results for a few values of σ are shown in Figure 7.1a-c. To cover the experimentally relevant parameters, we computed lifetime distributions across a two-dimensional space delimited by $0.1 \leq \sigma \leq 10$ and $0.1 \leq \mu \leq 100$. The activation barrier was assumed to be positive at all forces, $E_a > F\Delta x$; any negative forces/tensions were assumed to yield the unforced rate (14). The resulting lifetime distributions were fit by χ^2 minimization to each of three forms: exponential $P(\tau) \propto \exp\{-\tau / \tau_0\}$, stretched exponential $P(\tau) \propto \exp\{-(\tau / \tau_0)^\beta\}$, and log-normal $P(\tau) \propto \exp\{-[\ln(\tau / \tau_0) - m]^2 / 2s^2\} / \tau$, where τ_0 is a characteristic time, m is the log-mean and the degree of non-exponential behavior is controlled by either the dimensionless stretching exponent β or log-standard deviation s. While none of these forms provides an exact fit, a given form was deemed an acceptable description if it could not be statistically excluded ($p > 0.05$) using a simulated ensemble of 2000 lifetimes, a sample size chosen to match current state of the art single-molecule experiments. The domains in the $\{\sigma,\mu\}$ plane described by the three different forms are shown in Figure 7.1d. Remarkably, we found that a stretched exponential could fit nearly the entire domain (except for a small region where $\sigma > 2$ and $\sigma > \mu$). For $\sigma > 1$, the distribution can also be fitted-well by a log-normal form. In the small σ limit, $\sigma < 0.4$, the distribution is statistically indistinguishable from a single exponential. Overall, we find that the non-exponential behavior is controlled by the ratio of the force fluctuations' magnitude relative to a molecular parameter $\sigma = \sigma_F / F_0$ rather than their magnitude relative to the mean applied force, as might have been supposed.

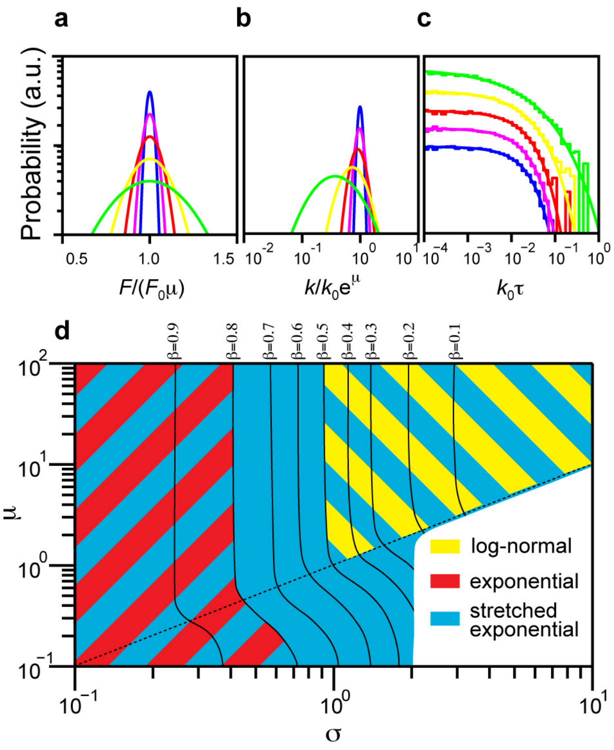

Figure 7.1. Gaussian force fluctuations give rise to non-exponential lifetime distributions. (a) Logarithmic-linear probability distributions of dimensionless force with constant mean, $\mu = 5$, and increasing standard deviation, $\sigma = 0.10$ (blue), 0.18 (purple), 0.32 (red), 0.56 (yellow) and 1.00 (green). (b) Double logarithmic plot of resulting log-normal $P(k) \propto (1/k)\exp\{-[\ln(k/k_0)-\mu]^2/2\sigma^2\}$ rate distributions with log-mean μ and log-standard deviation σ. (c) Double logarithmic dimensionless lifetime distributions and their best-fit stretched exponentials: $\beta = 0.97$ (blue), 0.94 (purple), 0.88 (red), 0.68 (yellow) and 0.42 (green), curves shifted vertically for clarity. (d) A phase portrait illustrating the regions of the $\{\sigma, \mu\}$ parameter space where the lifetime distributions are well described by a stretched exponential (blue), log-normal (yellow) or exponential (red) form (hatching indicates more than one model provides a good description). The solid curves are contour lines of constant β. The dashed line indicates $\sigma = \mu$. The lifetime distributions in the white region were not well described by any of the forms.

The second question we turn to is how slow the force fluctuations must be to be treated as quasi-static. In general, the survival probability is given by

$$S(t) = \exp\left\{ -\int_0^t k\left[F(t')\right]dt' \right\}. \tag{7.2}$$

If the force fluctuates rapidly in time, and the rate also changes rapidly, as it is exponentially dependent on the force, then the integral in the exponent becomes

$$\int_0^t k\left[F(t')\right]dt' \approx \langle k(F) \rangle t\,, \tag{7.3}$$

where $\langle k(F) \rangle$ is the time-averaged rate. The probability of surviving a time *t*, then, is described by a single exponential with a characteristic rate $\langle k(F) \rangle$ (15). As a result, even though the amount of time spent in the transition state is very short (16), it is the mean time for a tensed bond to overcome the activation barrier $\tau_{escape} = 1/\langle k(F) \rangle$ that is the relevant time scale.

7.3 Estimating the Forces in Single DNA Melting Experiments

The first test of this approach is to understand the lifetime distribution for DNA duplex dissociation, which has been reported as stretched exponential (7, 10, 11, 17, 18) and as exponential (1-3). The first report that we analyze is one published by our laboratory on the thermal dissociation of DNA duplexes (7). As illustrated in Figure 7.2a-b, the experiment consists of two micron-sized polymer spheres confined by a line optical trap and linked by a single DNA molecule. With zero optical force applied to the spheres, the duplex lifetimes obey a stretched exponential distribution with β= 0.45 ± 0.07 and $\tau_0 \approx$ 0.5 s. Although the optical forces were zero, the duplex was still subjected to a time varying entropic tension as the two tethered microspheres rattle in the optical trap.

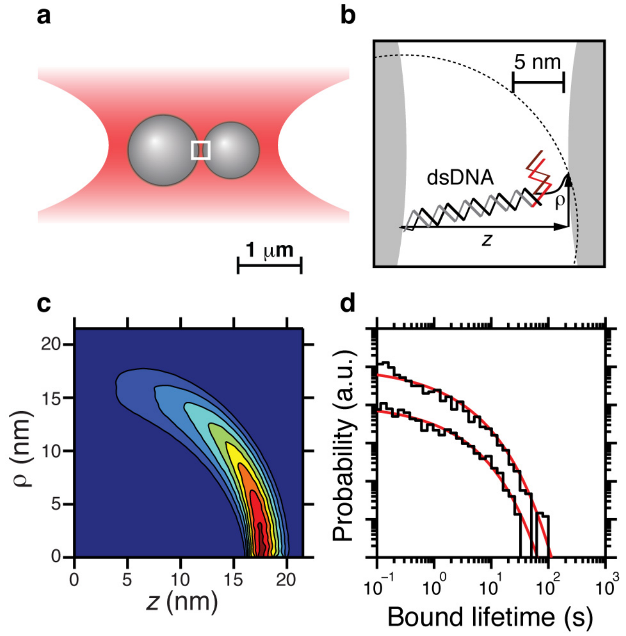

Figure 7.2. A single DNA duplex bridging between two microspheres has a stretched exponential lifetime distribution. (**a**) Geometry of the experimental system consisting of two polymer microspheres (**b**) linked together by a single DNA complex. The red section shows the 16 base pair DNA duplex whose dissociation lifetime is monitored. (**c**) The relative positions of the DNA anchor points on the two spheres occupy a hemispherical shell, whose simulated probability density $P(z,\rho)$ is shown. Red denotes the highest probability. (**d**) Double logarithmic distribution of simulated (bottom) and experimental (top) lifetime distributions, overlaid with best fit stretched exponentials having $\beta = 0.45$ and $\tau_0 = 0.5$ s. The distributions and fits are shifted vertically by a factor of 10 for clarity.

To compute the force distribution in the experiment, we use Monte Carlo sampling to compute the probability distribution of the relative positions of the DNA anchor points on the two spheres $P(z,\rho)$ shown in Figure 7.2c, and compute the potential of mean force (19) $W(z,\rho) = -k_B T \ln\left[P(z,\rho)\right]$. The corresponding force field was computed via the gradient of $W(z,\rho)$ and forces were sampled according to the Boltzmann distribution. This force distribution was then converted to a corresponding lifetime distribution taking the unforced rate k_0 and reactive compliance Δx as free parameters. Figure 7.2d shows the excellent agreement between the simulated and experimentally determined lifetime distributions for the reactive compliance Δx = 8.5 nm, consistent with well-known literature values (2). Unfortunately, the diffusion of the microspheres causes the force fluctuation correlation time (~10 ms) (7) to be much faster than the mean bound lifetime (~500 ms) (2). That our best-fit reactive compliance agrees quantitatively with experimentally determined values, though, suggests that force fluctuations on timescales apparently shorter than the mean lifetime may contribute to the observed non-exponential kinetics.

Stretched exponential lifetime distributions for DNA hairpin opening have also been observed by fluorescence correlation spectroscopy (FCS). Interestingly, Kim *et al.* measured stretched exponential lifetime distributions for short DNA hairpins with only a single GC base pair in the stem (18), which seems to rule out the hypothesis that such kinetics were due to misfolded intermediates. To test our hypothesis that force fluctuations may lead to non-exponential kinetics in hairpin dissociation, our collaborators Neeraj Agrawal and Ravi Radhakrishnan computed the force distribution produced by thermal fluctuations within a single-stranded DNA loop of various lengths. The ssDNA loop was modeled as an elastic, inextensible, homogeneous, object with bending stiffness K_b, where K_b is be determined from the persistence length ξ_p through the relationship $\xi_p = K_b/k_BT$. An ensemble of equilibrium conformations of the loop, as shown in Figure 7.3, was generated using the Monte Carlo technique (20) with umbrella sampling of the loop end-to-end distance a. As before, the potential of mean force as a function of a was computed from the distribution of *a* values, and fit to a quadratic function whose derivatives yielded the mean and standard deviation of the force distribution (Figure 7.3). The experimental FCS study (18) found a range of stretching exponents for both single and double GC base pair stems and loops consisting of three to nine dTs. After simulating each loop length, we find that we can fit all the stretching exponents using reactive compliance values in the range Δx = 3-8 Å, with the largest values corresponding to the longest loops. To our knowledge, there are no independent measurements of the reactive compliance for a single GC nucleotide pair, but our values seem comparable to the overall length change expected during in-plane straightening of a GC pair's bent equilibrium conformation ($\Delta x \approx 3$ Å), as might occur during serial rupture of their three hydrogen bonds. Again, simple estimates suggest the typical timescale for the force fluctuations would be of order nanoseconds, much slower that the picosecond attempt time for single base pair rupture, but comparable to the mean folded lifetime (21).

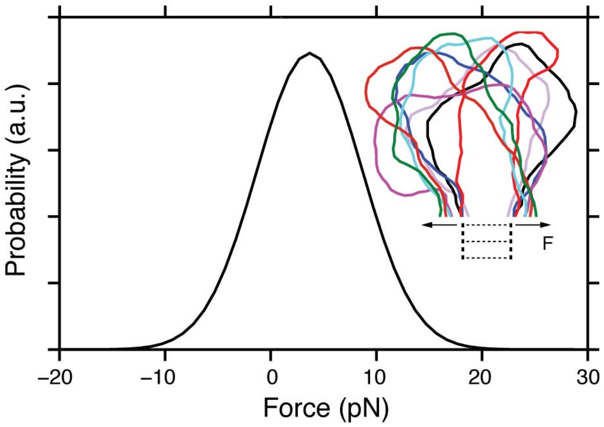

Figure 7.3. A semi-flexible polymer loop gives rise to Gaussian fluctuating forces. The force distribution at the loop-end for a 6 nm contour length ssDNA loop is shown, as obtained by Monte-Carlo technique. The force acting along the loop-ends is taken to be positive if it increases the loop-ends separation. The inset shows snapshots of the loop's thermal fluctuations. Simulations performed by Neeraj Agrawal and Ravi Radhakrishnan.

Of course, some measurements of DNA hairpin opening show purely exponential behavior, notably that of Woodside *et al.*(2), based upon measurements in an optical tweezer based force clamp. Simple estimates suggest that the fluctuating forces in that experiment are in excess of that required to give non-exponential kinetics in our model (22). Significantly, however, the large applied tension in that experiment directly couples the molecular reaction coordinate to a pair of microspheres, constraining the force fluctuations and the molecular attempt frequency to be of the same order, and voiding the quasi-static assumption required by our model. In this case, the degree of freedom presumably explores the time-averaged potential, resulting in an exponential lifetime distribution.

7.4 Forced Unfolding of Ubiquitin

Last, we turn to forced protein unfolding experiments, usually performed by using an atomic force microscope (AFM) to probe the force vs. extension, $F_m(x)$, behavior of a single protein as its domains unfold. This system can be treated as a fluctuating spring network (23), one of which is the AFM cantilever and the other of which is the (partially unfolded) protein. For our purposes, the fluctuating force can be computed from $\sigma_F = \sqrt{(k_{AFM} + k_m)k_B T}$, where k_{AFM} is the spring constant of the cantilever and the effective spring constant of the molecule is $k_m = \partial F_m / \partial x\big|_{x_{rest}}$, evaluated at its mean extension x_{rest} (23). We fit our model to published AFM pulling data for ubiquitin (8, 9, 24) that has been rigorously corrected for known sources of non-exponential behavior. We find that our model does fit the data using the computed force fluctuations if the reactive compliance of ubiquitin has a value $\Delta x \approx 0.20$ nm. The literature values (9) for the reactive compliance are in the range 0.19-0.25 nm, again in agreement with our prediction. Thus, we find that the kinetics of ubiquitin unfolding appear to be just that of a two-state system subject to the fluctuating forces expected in the experiment. Of course, given the complexity of data analysis in AFM pulling experiments, verification would require new data, preferably confirming the expected relationship between the non-exponential behavior and the force fluctuation amplitude, e.g. by changing the cantilever spring constant.

7.5 Anomalous DNA Kinetics Due to Finite Microsphere Diffusion

Another potential explanation for the stretched exponential kinetics observed in the thermal dissociation of a DNA duplex (7) arises naturally from our analysis presented in Chapter 5. Specifically, from the DNA labeling densities provided (~10 and >10^5 DNA/particle for the large and small sphere, respectively), we can estimate a Damköhler number > 10, similar to our linker-free systems that exhibited diffusion-limited binding. As a result, despite the fact that the expected number of bridges is < 1 and each physical binding event contains only a single duplex, the bound times that are observed in experiment likely contain a large number of reconnection events. In other words, because the forward rate of bridge formation is much higher than the particles' relative diffusivity, the particles are unable to diffuse apart before another bridge forms. In this limit, we would expect that the bound time distribution to be exponential, with an escape attempt frequency related only to the relative diffusivity of the particles. The fact that a stretched exponential distribution is observed instead, is likely a result of local density fluctuations or 'patchiness' on the densely labeled sphere.

It has been recently demonstrated that DNA-coated particles exhibit non-exponential binding as a result of density fluctuations (25). Specifically, if the binding in diffusion-limited, the characteristic time for the particles to stick together is given by

$$\tau\left(N_{eff}\right)=\frac{1}{\omega}\exp\left[-\frac{\Delta F\left(N_{eff}\right)}{k_B T}\right], \tag{7.4}$$

where ω is the escape attempt frequency and N_{eff} is the effective number of interacting DNA strands. If the number of interacting strands fluctuates between successive binding events according to some normalized statistical distribution $\rho(N_{eff})$ (most likely Gaussian), then the bound lifetime distribution becomes

$$P(t_b) = \sum_{N_{eff} \neq 0} \rho(N_{eff}) e^{-t_b/\tau(N_{eff})} . \tag{7.5}$$

Even though the number density fluctuations $\sqrt{N}/N$ in the interaction region are < 1%, there could be local patchiness in the strand distribution that would lead to a larger-than-expected dispersion in the forward rate. In the future, we should be able to use this analysis to determine exactly how large the local density fluctuations must be to yield a stretched exponential distribution with $\beta = 0.45$. Even in the absence of quantitative analysis, we are confident that the reported lifetimes are confounded by slow microsphere diffusion and do not represent actual single-molecule melting events.

7.6 Designing Single-Molecule Experiments with Colloidal Probes

Originally, we had designed a single-molecule experiment to measure the kinetics of DNA hairpin folding and unfolding (Figure 7.4). Unfortunately, while we were able to implement the design and collect dynamic data demonstrating molecular binding, it is unlikely that the bound events that we observed by particle tracking actually represent single bound states. Measurements of the forward rate of hairpin closure (10^4-10^5 s^{-1}) show that it is orders of magnitude faster than microsphere diffusion (~10^2 s^{-1}), suggesting that the hairpin likely opens and closes a number of times before the particles move apart. Again, even though this experiment is unambiguously in the single-molecule limit, our ability to really see what is happening is masked by the slow microsphere diffusion.

Unfortunately, only DNA hairpins with loops longer than ~100 nucleotides fold at rates comparable to 10^2 s^{-1} (10), and experiments with loops of that length are completely unfeasible. In the future, single-molecule experiments of this kind should be designed such that the forward rate of folding or binding be much slower than the microsphere diffusion.

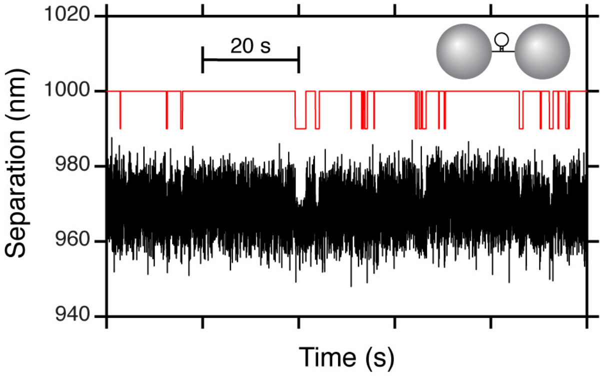

Figure 7.4. Single-molecule study of DNA hairpin folding and melting. A single DNA hairpin tethered between two polymer microspheres can undergo reversible binding and unbinding. When the forward rate of hairpin formation is faster than the microsphere diffusion, the separation between the particle centroids (black) is an inaccurate reporter of the molecular confirmation, as the hairpin can bind and unbind multiple times before the particles respond. As a result, the state of the molecule (red) that is inferred from the time-dependent separation is obscured by the slow microsphere diffusion.

7.7 Conclusion

Our findings suggest new methods for probing biomolecular kinetics and force sensitivity; beyond varying cantilever stiffness, one could use engineered peptide or nucleotide spacers to provide force fluctuations with known magnitudes and correlation times. At the least, this should enable the determination of reactive compliances and contributions to force fluctuations due to other parts of the molecule. Moreover, future experiments should pursue the idea that biomolecular bonds may ‘remember’ the force that they experience upon formation.

The model for non-exponential kinetics we have presented is strikingly generic; we suppose that it may be relevant for many other systems as well. Stretched exponential kinetics have been observed during the folding of some proteins (26), which could be accounted for within our model by a rate limiting, misfolded intermediate having a structure analogous to our DNA hairpins—fluctuating forces from a unfolded peptide loop acting on a force sensitive contact in the misfolded structure. Moreover, both the cytoskeleton and its *in vitro* polymer models display power-law rheology (22), associated with an unusually broad distribution of stress relaxation rates; the protein cross-links in those systems are typically force sensitive and the network structure should give rise to the fluctuating forces required. Last, stretched exponential kinetics have been observed in many glassy systems (27), corresponding perhaps to cage-breaking events being force sensitive, and responding to slowly fluctuating stresses from dynamical heterogeneity domains. Future work will probe the kinetics of small ensembles of stretched exponential modes coupled together, which we conjecture will lead to even more dramatically non-exponential behavior.

Finally, we develop simple design criteria that are required for experiments that use colloidal particles as reporters of single molecule conformations. Unlike previous ‘single molecule’ experiments that only considered the bond rupture rate, we suggest that the magnitude of the forward rate is equally important. Specifically, to accurately measure single molecular unfolding or unbinding events, the forward rate of folding or binding must be much slower than the microsphere diffusion. If this criterion is unsatisfied, the observed bound states are actually composed of a number of ‘hidden’ bound states that are obscured by the slow microsphere diffusion.

7.8 References

1. Woodside MT*, et al.* (2006) Direct measurement of the full, sequence-dependent folding landscape of a nucleic acid. *Science* 314:1001-1004.
2. Woodside MT*, et al.* (2006) Nanomechanical measurements of the sequence-dependent folding landscapes of single nucleic acid hairpins. *Proceedings of the National Academy of Sciences of the United States of America* 103:6190-6195.
3. Liphardt J, Onoa B, Smith SB, Tinoco I, Bustamante C (2001) Reversible unfolding of single RNA molecules by mechanical force. *Science* 292:733-737.
4. Ritort F (2006) Single-molecule experiments in biological physics: methods and applications. *Journal of Physics-Condensed Matter* 18:R531-R583.
5. Fernandez JM, Li HB (2004) Force-clamp spectroscopy monitors the folding trajectory of a single protein. *Science* 303:1674-1678.
6. Van Orden A, Jung J (2008) Fluorescence correlation spectroscopy for probing the kinetics and mechanisms of DNA hairpin formation. *Biopolymers* 89:1-16.
7. Biancaniello PL, Kim AJ, Crocker JC (2008) Long-time stretched exponential kinetics in single DNA duplex dissociation. *Biophysical Journal* 94:891-896.
8. Brujic J, Hermans RI, Walther KA, Fernandez JM (2006) Single-molecule force spectroscopy reveals signatures of glassy dynamics in the energy landscape of ubiquitin. *Nature Physics* 2:282-286.
9. Garcia-Manyes S, Brujic J, Badilla CL, Fernandez JM (2007) Force-clamp spectroscopy of single-protein monomers reveals the individual unfolding and folding pathways of I27 and ubiquitin. *Biophysical Journal* 93:2436-2446.
10. Bonnet G, Krichevsky O, Libchaber A (1998) Kinetics of conformational fluctuations in DNA hairpin-loops. *Proceedings of the National Academy of Sciences of the United States of America* 95:8602-8606.
11. Wallace MI, Ying LM, Balasubramanian S, Klenerman D (2001) Non-Arrhenius kinetics for the loop closure of a DNA hairpin. *Proceedings of the National Academy of Sciences of the United States of America* 98:5584-5589.
12. Bell GI (1978) Models for Specific Adhesion of Cells to Cells. *Science* 200:618-627.
13. Richert R (1985) Analysis of Non-Exponential 1st-Order Reactions. *Chemical Physics Letters* 118:534-538.
14. Tees DFJ, Woodward JT, Hammer DA (2001) Reliability theory for receptor-ligand bond dissociation. *Journal of Chemical Physics* 114:7483-7496.
15. Zwanzig R (1990) Rate-Processes with Dynamic Disorder. *Accounts of Chemical Research* 23:148-152.
16. Dellago C, Bolhuis PG, Csajka FS, Chandler D (1998) Transition path sampling and the calculation of rate constants. *J. Chem. Phys.* 108:1964-1977.
17. Jung JM, Van Orden A (2005) Folding and unfolding kinetics of DNA hairpins in flowing solution by multiparameter fluorescence correlation spectroscopy. *Journal of Physical Chemistry B* 109:3648-3657.

18. Kim J, Doose S, Neuweiler H, Sauer M (2006) The initial step of DNA hairpin folding: a kinetic analysis using fluorescence correlation spectroscopy. *Nucleic Acids Research* 34:2516-2527.
19. Biancaniello PL, Kim AJ, Crocker JC (2005) Colloidal interactions and self-assembly using DNA hybridization. *Physical Review Letters* 94:058302.
20. Agrawal NJ, Radhakrishnan R, Purohit PK (2008) Geometry of mediating protein affects the probability of loop formation in DNA. *Biophysical Journal* 94:3150-3158.
21. Cocco S, Monasson R, Marko JF (2001) Force and kinetic barriers to unzipping of the DNA double helix. *Proc. Natl Acad. Sci. USA* 98:8608-8613.
22. Gardel ML*, et al.* (2006) Stress-dependent elasticity of composite actin networks as a model for cell behavior. *Physical Review Letters* 96:-.
23. Marshall BT*, et al.* (2006) Measuring molecular elasticity by atomic force microscope cantilever fluctuations. *Biophysical Journal* 90:681-692.
24. Brujic J, Hermans RIZ, Garcia-Manyes S, Walther KA, Fernandez JM (2007) Dwell-time distribution analysis of polyprotein unfolding using force-clamp spectroscopy. *Biophysical Journal* 92:2896-2903.
25. Xu Q, Feng L, Sha R, Seeman NC, Chaikin PM (2011) Subdiffusion of a Sticky Particle on a Surface. *Physical Review Letters* 106.
26. Sabelko J, Ervin J, Gruebele M (1999) Observation of strange kinetics in protein folding. *Proceedings of the National Academy of Sciences of the United States of America* 96:6031-6036.
27. Phillips JC (1996) Stretched exponential relaxation in molecular and electronic glasses. *Reports on Progress in Physics* 59:1133-1207.

Chapter 8

Conclusions and Future Directions

DNA hybridization can be used to induce specific attractions between small particles, providing a highly versatile approach to creating novel particle-based materials having a variety of periodic structures. In this thesis, we designed, measured, and modeled these weak, reversible DNA-induced colloidal interactions for a number of relevant DNA architectures. We develop a clear modeling framework to accurately predict the equilibrium binding between DNA-labeled colloids as a function of experimentally relevant parameters (e.g. DNA sequence, strand density, particle size, temperature, ionic strength, etc.). Unlike other measurements that infer the interaction strength by mapping the temperature-dependent aggregation-disaggregation transition, we designed and constructed a line optical tweezers instrument that enabled us to directly measure the pair-interactions with high spatial and temporal resolution. Our instrument is ultimately able to measure the separation between two micron-scale colloidal particles to roughly 1 nm in excess of 10 kHz, and can be used to measure other short-range, thermally accessible colloidal and surface forces.

Our measured DNA-induced pair-interaction potentials can be modeled quantitatively using the principles of chemical equilibrium and binomial statistics, generalized for spatially nonuniform reactants (1). The generality of our modeling framework allows for its seamless extension to various DNA sequences and architectures (e.g. linker-free binding, linker-mediated binding, self-binding with competitive interactions, etc.). Moreover, our model is able to accurately describe interactions between nanoparticles that are necessarily small relative to the DNA contour length (2, 3) or have nonspherical shapes (4). In the future, the ability to reliably model the interactions between particles with multiple, potentially interacting DNA strands will be key to the development of more complex nanomaterials using DNA-directed assembly (5).

Further refinements of our equilibrium binding model will likely require direct measurement of the nucleic acid thermodynamics. While the unified nearest-neighbor model is an indispensable tool in designing and modeling DNA-induced interactions, it is often difficult to differentiate its *a priori* uncertainty from other systematic deviations. Because the optical tweezers studies of linker-mediated binding are somewhat pathological, i.e. the pair of particles is immersed in a semi-infinite reservoir of linker strands, complementary aggregation-disaggregation-type experiments could help bridge the gap to assembly-relevant colloidal volume fractions. Moreover, future linker-based architectures should be designed to minimize any potential entropic or enthalpic penalties associated with bending the duplex bridge (e.g. linkers with long unpaired hinge sequences or pairs of complementary linkers).

Additional pair-interaction experiments should be designed to isolate and study the effects of force-sensitivity in DNA duplex-bridges (e.g. by systematically varying their reactive compliance). The incorporation of force-sensitivity into our equilibrium binding model will likely be required for the design of more complex DNA architectures. In addition, force-sensitivity remains a relatively unexplored control-knob in DNA-directed assembly. For example, the entropic tension experienced by DNA bridges could be modulated through incorporation of hairpins in the spacer sequences and provide an additional means to finely tune the interaction strength, where the bridges experience a higher tension when their hairpins are folded. Intentionally designed secondary structure in the DNA strands could also be used to design switchable interactions. As demonstrated, interactions between particles that are labeled with sequences whose 'sticky ends' are palindromic and form hairpins, can be turned 'on' and 'off' in a temperature-dependent way (6). Future theoretical work should be able to use our measured potentials to explore interesting assembly strategies and novel equilibrium structures in simulation. Moreover, because our model is constructed from experimentally relevant variables, there is a direct mapping from simulation to the lab. For example, if it were beneficial to adjust the range or shape of the pair-interaction, we could accomplish that by changing the length or flexibility of the spacer sequences, and then directly validate our construct experimentally.

Unlike earlier studies that raised concerns that DNA-mediated binding may be inherently slow, we find that the dynamics can be modulated from effectively diffusion-limited to reaction-limited by reducing the number of DNA strands grafted to the particles' surfaces. When the microspheres are labeled with at least ~5,000 molecules each, the distribution of their bound lifetimes is exponential for interaction strengths up to ~6 k_BT. Moreover, their mean bound lifetime scales exponentially in the binding energy with an escape attempt frequency that is limited by the microspheres' relative diffusivity. When the particles are labeled with fewer than ~5,000 DNA strands, they exhibit reaction-limited binding that scales quadratically with the strand density. In this limit, the bound lifetimes are significantly non-exponential and can potentially slow annealing times during crystallization. A simple dynamic model is able to reproduce the non-exponentiallity of the measured bound time distributions by including static disorder in the melting rate at the single molecule-level. We also study the dynamics of linker-mediated binding and demonstrate that it can be made diffusion-limited by stabilizing one of the linker-bound intermediate species. This is most easily accomplished by designing linker strands that have asymmetric or unbalanced hybridization Gibbs free energies for their two reactive ends.

Our experimental method and theoretical framework are also amenable for extension to the study of reversible ligand-receptor pairs in the single-molecule limit. We suggest that, in addition to tuning the unbinding or unfolding rate, care must be taken in designing the systems forward rate to eliminate artifactual binding/unbinding events. Specifically, when using particle tracking of colloidal spheres to infer the conformation of a tethered molecule (e.g. a DNA duplex or hairpin), the system must be designed so that the forward rate of folding/hybridization is less than the particles' relative diffusivity. We suggest that previous studies of DNA duplex (7) and hairpin melting were not strictly in this limit, and that each observed bound state was actually an ensemble of a number of rapid reconnection events.

In conclusion, we described the design and implementation of an optical tweezers instrument capable of measuring short-range, thermally accessible colloidal interactions with nanometer precision. We demonstrated the functionality and usefulness of this instrument by measuring the entropic attraction that micron-scale colloidal particles experience in the presence of concentrated, non-adsorbing micelles. We used the same instrument to measure the equilibrium binding interactions between a variety of different DNA-functionalized colloidal systems, and developed a mean-field pair-interaction model that is able to quantitatively capture the spatial and temperature dependence of the DNA-induced colloidal interactions up to binding energies relevant for self-assembly. The associated dynamics can be tuned from diffusion-limited to reaction-limited by decreasing the DNA strand density. When reaction-limited, the bound times follow a surprising power law scaling that may be caused by static disorder at the single molecule level, and could significantly slow annealing during crystallization. Lastly, we suggest that our experimental and theoretical approach is well-suited for studying other dynamic systems that are governed by weak ligand-receptor pairs (e.g. Dscam protein-mediated interactions (8)).

8.1 References

1. Rogers WB, Crocker JC (2011) Direct measurements of DNA-mediated colloidal interactions and their quantitative modeling. *Proceedings of the National Academy of Sciences of the United States of America* 108:15687-15692.
2. Macfarlane RJ*, et al.* (2009) Assembly and organization processes in DNA-directed colloidal crystallization. *Proceedings of the National Academy of Sciences of the United States of America* 106:10493-10498.
3. Macfarlane RJ*, et al.* (2010) Establishing the Design Rules for DNA-Mediated Colloidal Crystallization. *Angewandte Chemie-International Edition* 49:4589-4592.
4. Jones MR*, et al.* (2010) DNA-nanoparticle superlattices formed from anisotropic building blocks. *Nature Materials* 9:913-917.
5. Hormoz S, Brenner MP (2011) Design principles for self-assembly with short-range interactions. *Proceedings of the National Academy of Sciences of the United States of America* 108:5193-5198.
6. Leunissen ME*, et al.* (2009) Switchable self-protected attractions in DNA-functionalized colloids. *Nature Materials* 8:590-595.
7. Biancaniello PL, Kim AJ, Crocker JC (2008) Long-time stretched exponential kinetics in single DNA duplex dissociation. *Biophysical Journal* 94:891-896.
8. Hattori D*, et al.* (2007) Dscam diversity is essential for neuonal wiring and self-recognition. *Nature* 449:223-227.